IN SEARCH OF THE AXION PARTICLE WITH RF CAVITIES IN CAST EXPERIMENT AT CERN

by
Kaan Özbozduman
B.S., Physics, Boğaziçi University, 2017

Submitted to the Institute for Graduate Studies in
Science and Engineering in partial fulfillment of
the requirements for the degree of
Master of Science

Graduate Program in Physics
Boğaziçi University
2021

ACKNOWLEDGEMENTS

I would like to express my gratitude to the thesis committee for allocating time to examine this work.

I count myself very lucky to have three supervisors in my thesis studies.

I am grateful to Prof. V. Erkcan Özcan. I was fascinated by his genius in teaching modern physics laboratory course in the Spring of 2016. This experience also motivated me to carry on my research in particle physics. Two years later, he welcomed me to his research group and supported me to work at CERN for CAST. He was so generous to provide me with this great opportunity in dawn of my academic carrier.

I would not be working at CAST without the support of Prof. Serkant A. Çetin. When Prof. Özcan told me that we would meet the Dean of Bilgi University, I was a bit stressed out and worried for not having worn appropriately. Soon after our conversation started, I was relieved by his sincere, encouraging attitude. I am thankful to Prof. Çetin for his continuing support throughout my studies in CAST. His valuable advices and appreciation of the work I have been doing has always motivated me.

Most students I met at CERN would complain about not having enough time to spend with their supervisors. I was fortunate to have the chance to reach my supervisor whenever I needed almost every day. Prof. Konstantin Zioutas is one of the most passionate persons about research. He spreads this spirit and positivity to everyone working with him. He always helped me, initially for my integration to CERN and then for my studies in CAST. I learned a lot from his studiousness and punctuality. Conversations we had on both research and non-research subjects were priceless.

Many thanks to Arif Bayırlı and Cenk Yıldız, former students of CAST. Arif introduced CAST to me in a chat when I had no idea about it. Encouraged by him, I went to the office of Prof. Özcan and asked if I can work in CAST as well. Cenk also would help me whenever I am in need at CERN. I was like their substitute at CAST and benefited a lot from the good impression they had left there.

Marios Maroudas and I were partners in the CAST-CAPP detector research. I always felt lucky to work with this intelligent and hardworking gentleman. He is never afraid to get his hands dirty for the sake of science. He has been the dynamo of CAST-CAPP and did a great job to make CAST-CAPP, once considered hopeless, the most prominent project of CAST. He would lend me a helping hand whenever I needed and introduced me the local environment and the city. I am grateful to him and his girlfriend Foteini for kindly inviting me to day trips, and afternoon runs which I enjoyed a lot.

Support of my family has been the driving force that helped me succeed in education and research. Every move they made as I grew up, buying my first science book, an illustrated animal atlas, when I was 6, backing me when I decided to major in physics at the age of 18, helping me prepare my luggage the day before my first travel to CERN, helped and motivated me to carry on. They were always caring and trying to create the happy, supportive environment for me to study, work and rest. Many thanks and love to Kaya, Hasniye and Nihal, my parents and sister.

I have benefited and enjoyed a lot by the wisdom, support and company of Fritz Caspers, Prof. Horst Fischer, Wolfgang Funk, Prof. Giovanni Cantatore in CAST group; Prof. Yannis Semertzidis, Çağlar Kutlu in IBS/CAPP group and Semra Türkçapar, Michael Betz, Sinem Şimşek, Mehtap Tinaz. I want to say thanks to all.

ABSTRACT

IN SEARCH OF THE AXION PARTICLE WITH RF CAVITIES IN CAST EXPERIMENT AT CERN

Axion is a pseudo scalar boson that is predicted to solve the strong CP problem and therefore cast light upon curious CP invariance of the strong nuclear interactions. It is also a promising candidate to be the building block of the dark matter. CAST was invented more than 20 years ago as an axion helioscope, searching for high energy solar axions and it has exceeded the expectations throughout its operation. In a published article in 2017, CAST has declared a new research program to explore galactic halo (dark matter) axions.

CAST-CAPP detector searches for dark matter axions using four microwave cavities that operate in 4.7-5.4 GHz band corresponding to $\sim$19-22 μeV axion mass. It has started operation in 2019, after several years of design, installations and tests. CAST-CAPP is unique in a sense that it utilizes multiple portable rectangular cavities that can be phase-matched in order to amplify the axion signal. In 2 data taking runs, preliminary results indicate that CAST-CAPP has pushed the limits of axion search by exploring new regions in the parameter space.

ÖZET

CERN'DEKİ CAST DENEYİNDE RF KAVİTELER İLE AXİON PARÇACIĞI ARAŞTIRMALARI

Axion, güçlü yük-parite sorununu çözerek güçlü çekirdek kuvvetinin neden yük-parite simetrisine aykırı davranmadığı sorusuna ışık tutmak için ortaya atılan bir psödoskalar bozondur. Axion ayrıca karanlık maddenin yapıtaşı olabilecek bir parçacık adayıdır. CERN axion güneş teleskopu (CAST), 20 yıldan uzun bir süre önce güneşten gelebilecek yüksek enerjili axionları algılamak için kuruldu ve işleyişi boyunca beklentilerin üzerinde bir başarı gösterdi. 2017 yılında yayınlanan bir makalesinde CAST gelecek yıllar için belirlediği araştırma programının odağında karanlık maddeyi oluşturduğu düşünülen gökada halesi axionlarını aramak olacağını bildirdi.

CAST-CAPP, dört mikrodalga kovuk ile ∼19-22 μeV axion kütlesine denk gelen 4.7-5.4 GHz bandında karanlık madde olmaya aday axion parçacıklarını araştıran bir algıçtır. Birkaç yıl süren tasarım, kurulum ve deneme sonucu 2019 yılında çalışmaya başlayan CAST-CAPP, birden çok dikdörtgen prizma şekilli, taşınabilir mikrodalga kovuğu faz eşleme yöntemiyle işleterek axion sinyalini yükseltme potansiyeli ile özgün bir deneydir. İki veri alım dönemi sonucunda elde edilen öncül sonuçlar, CAST-CAPP'ın mevcut axion araştırması sınırlarını genişleterek, axion parametre uzayında yeni alanları keşfettiğini göstermektedir.

TABLE OF CONTENTS

ACKNOWLEDGEMENTS . . . iii
ABSTRACT . . . v
ÖZET . . . vi
LIST OF FIGURES . . . ix
LIST OF TABLES . . . xv
LIST OF SYMBOLS . . . xvi
LIST OF ACRONYMS/ABBREVIATIONS . . . xviii
1. INTRODUCTION . . . 1
1.1. CERN Axion Solar Telescope (CAST) . . . 3
1.2. CAST-CAPP . . . 6
2. AXION THEORY . . . 8
2.1. Strong CP Problem . . . 8
2.2. Peccei-Quinn Theory and Axion . . . 9
2.3. Axion-photon Conversion . . . 10
2.4. Axion Signal Shape . . . 12
2.5. Axion Dark Matter Streams . . . 15
3. MICROWAVE CAVITIES . . . 16
3.1. Microwave Cavities in Analogy with RLC Circuits . . . 18
3.2. Geometry Factor . . . 20
3.3. Signal Power . . . 20
4. CAST-CAPP EXPERIMENT . . . 22
4.1. Hardware . . . 22
4.1.1. Cavities . . . 25
4.1.2. Vector Network Analyzer . . . 27
4.1.3. Spectrum Analyzer . . . 28
4.1.4. Installation in Summer 2019 . . . 30
4.1.5. Amplifiers . . . 33
4.2. Coherence of Axion signal . . . 35

4.3. Combining Multiple Cavities with Phase-matching 35
4.4. Data Acquisition 38
4.4.1. Data-taking Run of 2018 41
4.4.2. Data-taking Run of 2019 41
4.4.3. Data-taking Run of 2020 42
4.5. Data Acquisition Statistics 42
4.6. Data Acquisition Strategies 44
4.6.1. Fast Tuning Method 44
4.6.2. Wide Band Scanning 45
4.7. Sensitivity Prospects 47
4.8. Future of CAST-CAPP 49
5. DATA PROCESSING AND ANALYSIS 52
5.1. From Time Domain to Frequency Domain: Fourier Transform 52
5.2. Sampling Theorem 53
5.3. Zeroth Frequency and Data Detrending 55
5.4. Data Processing and Noise Characteristics 55
5.5. Analysis Overview 62
5.6. Data Qualification 63
5.7. IF Interference Detection 66
5.8. Flattening Processed Spectra 67
5.9. Combining Multiple Spectra 70
5.10. Grand Spectrum 75
5.11. A Simulation to Account for Grand Spectrum Correlations 78
5.12. Threshold for Candidate Selection 82
5.13. Exclusion 84
5.14. Axion Candidates 86
6. CONCLUSION 88
REFERENCES 89
APPENDIX A: AXION LINE SHAPE 95
APPENDIX B: FAST FOURIER TRANSFORM 98
APPENDIX C: COPYRIGHT PERMISSIONS 100

LIST OF FIGURES

Figure 1.1. Axion-photon coupling exclusion limit. [1] 3

Figure 1.2. CERN Axion Solar Telescope (CAST). 4

Figure 1.3. CAST layout. [2] 5

Figure 1.4. Schematic of CAST as an axion helioscope. [1] 6

Figure 2.1. Feynman diagrams of Primakoff effect. Axion is coupling to (a) two photons in vacuum, (b) a photon in the presence of a static magnetic field (virtual photon) [3] 11

Figure 2.2. Galactic halo axion signal shape in lab vs galactic frame. Horizontal axis gives, $\nu - \nu_a$, the frequency distance from $\nu_a = 5.0$ GHz. . . . 14

Figure 2.3. Variation of the galactic halo axion signal shape in lab frame across CAST-CAPP frequency range. Horizontal axis gives, $\nu - \nu_a$, the frequency distance from $\nu_a = 5.0$ GHz. 14

Figure 3.1. Sketch of a CAST-CAPP cavity. 17

Figure 3.2. Lorentzian shaped profile of the cavity resonance mode. 18

Figure 3.3. Unloaded RLC circuit as a model of a resonant cavity. 18

Figure 4.1. CAST-CAPP experiment setup devices and connections. Names of the instruments are given in text. 23

Figure 4.2. CAST-CAPP system diagram. Dashed lines indicate cavity input connections. Solid lines show receiver i.e., cavity output connections. CAST cryostat layers are indicated by colors. The drawing shows the cavities on top of each other in order to fit the diagram in the page. In reality, 4 cavities in the magnet bore are aligned on the axis of their length. 24

Figure 4.3. CAST-CAPP cavity. 25

Figure 4.4. CAST-CAPP cavity inside view and tuner bars (a). Potential tuning range of the cavities (b). Resonance frequency as a function of the insulating bar positions (blue) and that of the empty cavity (red), all for TE_{101} mode. [4] 26

Figure 4.5. CAST-CAPP tuning mechanism. Locomotive wheel and the coupling rod are indicated by red circle on both the photograph and the technical drawing. 26

Figure 4.6. VNA monitor showing the CAST-CAPP cavity resonance modes in 100 MHZ range about ∼5.3 GHz. 27

Figure 4.7. Noise bump of the cavity displayed by the spectrum analyzer indicates good quality of the receiver chain. 28

Figure 4.8. Visualization of the cavity output during a test signal injection to the cavity input. Sine shape of the test signal is visible time trace (lower part of the screen) where the complex IQ measurements are depicted as different (blue and yellow) sine waves of shifted phase. The upper box on the spectrum analyzer screen shows the frequency domain plot of the measurement where the sine wave appears as a narrow line (blue) in the middle of the screen. 29

Figure 4.9. Photographs of CAST magnet closed (left) and opened (right). Several important parts are indicated with color: 300 K (warm) flange (yellow), 70 K clamp on copper vessel (red), magnet bore after 2 K flange removed (green). CAST-CAPP uses the the one on the right (green) of the two identical magnet bores. 31

Figure 4.10. Images of piezoelectric tuner motor and its locomotive wheel (a), double springs on the rear side of the motor (b) and aluminum lock strips between 2 cavities (c). 32

Figure 4.11. Photograph (left) and technical drawing (b) of the broken shaft of the tuner plates in cavity 4 indicated by red circles. 33

Figure 4.12. Low noise amplifier gain and noise measurement as a function of frequency at temperature $\approx$ 5K. 34

Figure 4.13. VNA screen showing that 4 cavity modes are aligned with respect to frequency and amplitude. 37

Figure 4.14. Screen of the local CAST-CAPP PC during simultaneous data-taking and analysis. 39

Figure 4.15. Histogram of cavity data-taking times over the frequency range. Colors denote cavities 1 (blue), 2 (orange), 3 (green), 4 (red). . . . 44

Figure 4.16. WBS test measurements with an injected (fake) signal of power varied powers. Output powers are plotted as a function of the frequency distance from TE_{101} resonance mode center. 46

Figure 4.17. Axion-photon coupling exclusion prospects as a function of time, given the frequency tuning range (data acquisition range) with colors: Red (5 MHz), blue (50 MHz), black (500 MHz). Solid lines denote the case for 4 phase-matched cavities whereas dashed lines mark the single cavity case. 48

Figure 4.18. Time to reach KSVZ (solid, red) and DFSZ (solid, black) axion coupling sensitivity as a function of tuning range. Dashed lines indicate KSVZ & DFSZ axion coupling x10 with colors red & black, respectively. 49

Figure 4.19. CAST-CAPP axion parameter space scanning prospects in short-term. The region bounded by red line is to be scanned by a single cavity and the one with blue line boundary is to be scanned by 3 phase-matched cavities. 50

Figure 5.1. A diagram of DFT output frequencies. 54

Figure 5.2. Normalized distribution of FFT voltage and power outputs. FFT power spectrum displays χ^2 distribution of 2 degrees of freedom. Because it is given by (Equation 5.10) the sum of squares of 2 normally distributed parameters. FFT voltage spectrum has χ distribution as it is proportional to the square root of the power spectrum as indicated by Equation 5.9. Baselines of both FFT power and voltage spectra were removed before histogramming and distribution functions were scaled. 57

Figure 5.3. CAST-CAPP FFT spectrum of a single chunk (grey) of 0.02s data and 3000 packs averaged (black) of 1-minute data. Yellow band is the IF filter roll-off. 58

Figure 5.4. FFT spectrum of 1-minute data as an average of FFT power spectra of 3000 chunks. Baseline of the spectrum was removed before histogramming. 59

Figure 5.5. Standard deviation of flattened noise spectrum versus data taking time. 61

Figure 5.6. Processed spectrum 1-minute data as an average of FFT power spectra of 3000 chunks and the SG filter applied to it (upper). Processed spectrum noise baseline is removed to obtain the flattened spectrum (lower). 68

Figure 5.7. Transfer function of Savitzky-Golay filter with parameters: Window length = 1001, polynomial order = 4. 69

Figure 5.8. Scaled spectrum. 71

Figure 5.9. Vertical averaging of scaled spectra demonstrated on 9 sample scaled spectra. Scaled spectra are aligned according to RF index (top). Weighted averaging of the scaled spectra with maximum likelihood method (middle) where data in black and red represent p_k^C and σ_k^C. Lower plot shows the normalized combined spectrum where data in black and blue represent $x_k^C = p_k^C/\sigma_k^C$ and $(\sigma_k^C)^{-1}$. 73

Figure 5.10. Combined spectrum (top black) and its SNR for a prospective axion signal (bottom blue). 74

Figure 5.11. Combined spectrum histogram. 75

Figure 5.12. Grand spectrum (top, black) and its SNR for a prospective axion signal (bottom, blue). 78

Figure 5.13. Grand spectrum histogram. 79

Figure 5.14. Covariance distribution among SCS bins with bin spacing < 28. . 81

Figure 5.15. Covariance distributions among SRS separately for bin spacing = 1, 2, 3, 4 denoted by colors. Color code: Green for $\Delta j = 1$, blue for $\Delta j = 2$, yellow for $\Delta j = 3$, Magenta for $\Delta j = 4$. 81

Figure 5.16. Hypothesis testing in search of the axion signal in grand spectrum. 83

Figure 5.17. Axion-photon coupling exclusion plot for CAST-CAPP data. . . . 85

LIST OF TABLES

Table 3.1. Parameters that contribute to axion power in an RF cavity. 21

Table 4.1. CAST-CAPP cavity tuning optimal and maximal ranges for each cavity. 33

Table 4.2. Scaling of SNR with the combination of N correlated/uncorrelated signals versus noise (uncorrelated by default) for the distinct definitions of SNR. 38

Table 4.3. CAST-CAPP data acquisition statistics classified according to cavity identities for axion sensitive measurements taken with magnetic field on. PM denotes phase-matched cavities. 43

Table 4.4. CAST-CAPP data acquisition statistics classified according to cavity identities for axion insensitive measurements with magnetic field off. PM denotes phase-matched cavities. 43

Table 5.1. An account of the spectra we generate in the analysis procedure. . 63

Table 5.2. Statistics of datafiles discarded from the analysis of CAST-CAPP data due to not fulfilling the standards set for qualification. "Initial" and "Final" labels indicate the measurements before and after a measurement, respectively. 65

LIST OF SYMBOLS

a	Axion field
B	Magnetic field
c	Speed of light
C_{lmn}	Geometry factor of a cavity
E	Electric field
h	Planck's constant
$\hbar$	Reduced Planck's constant
$g_{a\gamma\gamma}$	Axion-photon coupling
g_γ	Unitless coupling constant
k	Number of FFT chunks
k_B	Boltzmann's constant
m_a	Axion mass
n	Number of spectra
N	Number of bins (samples) in a spectrum
N_0	Noise power density
p	Momentum
P	Polynomial order of the Savitzky-Golay filter
Q	Quality factor
Q_a	Quality factor of axion signal
Q_L	Loaded Quality factor
t	Data taking time
T	Acquisition time of a spectrum
T_s	Noise temperature of the system
U	Stored energy in the cavity
W	Window length of the Savitzky-Golay filter
x	Height of a normalized bin of a spectrum
Z	Partition function

α	Fine-structure constant
β	Coupling factor
$\delta\nu$	Resolution bandwidth
$\delta\nu_a$	Axion bandwidth
$\Delta\nu$	Bandwidth
Δt	Sampling interval in time (Reciprocal of sampling rate)
ϵ_0	Vacuum permittivity
λ	Wavelength
μ	Mean value
μ_0	Vacuum permeability
ν	frequency (used interchangeably with f)
ν_0	center frequency of a cavity resonance mode
ν_a	Axion frequency
ν_c	Nyquist critical frequency
ρ_a	Axion energy density
σ	Standard deviation
τ	Time length of data series
ω	Angular frequency

LIST OF ACRONYMS/ABBREVIATIONS

ADMX	Axion Dark Matter eXperiment
AU	Arbitrary Units
CAPP	Center for Axion and Precision Physics
CAST	CERN Axion Solar Telescope
CASTOR	CERN Advanced STORage manager
CERN	Conseil Européen pour la Recherche Nucléaire
COV	COVariance
CP	Charge-Parity
dB	DeciBell
dBm	DeciBell-Milliwatts
DAQ	Data AcQuisition
DFSZ	Dine, Fischler, Srednicki and Zhitnitski
DFT	Discrete Fourier Transform
DM	Dark Matter
EMI	ElectroMagnetic Interference
FFT	Fast Fourier Transform
FSM	Fast Scanning Method
FWHM	Full Width at Half Maximum
IF	Intermediate Frequency
KSVZ	Kim, Shiftman, Vainshtein and Zakharov
LHC	Large Hadron Collider
ML	Maximum likelihood
QCD	Quantum ChromoDynamics
RAID	Redundant Array of Independent Disks
RBW	Resolution Bandwidth
RF	Radio Frequency
RMS	Root Mean Square
SA	Spectrum Analyzer

SCS	Simulated Combined Spectra
SFS	Simulated Flattened Spectra
SG	Savitzky-Golay
SNR	Signal-to-Noise Ratio
SPS	Simulated Processed Spectra
SRS	Simulated Rebinned Spectra
TE	Transverse Electric field
VNA	Vector Network Analyzer
WBS	Wide Band Scanning

1. INTRODUCTION

Standard model of particle physics is made possible by the understanding of the building blocks of our universe lead by many discoveries in the last ∼150 years. Each new discovery, the latest one was that of Higgs particle at CERN, has filled a gap in this puzzle, strengthening our picture of nature. Still, there are more gaps to fill to improve our depiction of reality. Strong charge-parity (CP) problem stands out to be one of the most prominent issues in particle physics that arose in the last century. The problem is, strong force has proven to conserve CP symmetry in all experiments while theoretical models (QCD) allow for CP violation in strong interactions. Peccei-Quinn mechanism, a widely acknowledged explanation to the problem, requires the existence of pseudoscalar boson. Named after a detergent brand, axion is expected to clean a big mess in particle physics.

Even more profound than the strong CP problem, a big issue of the science is explaining why there seems to be much more matter in galaxies than observed. Observations indicate a discrepancy between the orbital motion of the stars around the galaxy center and Newtonian mechanics (or equivalently the general theory of relativity) which they should obey. [5] Rotation speeds of the stars away from the galaxy center are observed to be more or less constant, independent of the distance from the galaxy center while Kepler's laws require a significant decline. The most straight forward solution is the presence of matter in galaxies in an invisible form. Because of its obscurity, this extra matter is called dark matter. While the dark matter theory is also supported by the observations of gravitational lensing [6], galactic rotation curve data [7] indicates the dark matter that should be present in order to account for the observations constitutes $\sim 27\%$ of the universe, outweighing the normal, luminous matter ($\sim 5\%$ of the universe) by a factor of 5, roughly.

Dark matter is also searched at microscopic level. Various theoretical models suggest that dark matter might be made up of weakly interacting massive particles (WIMPs). Promising experiments such as XENON1T study nuclear recoils of liquid xenon to detect an interaction involving WIMPs [8] Experiments in the Large Hadron Collider (LHC) at CERN also look out for missing energy and momentum after collisions that might escape the detectors in the form of dark matter particles.

Axion is also a dark matter candidate due to its weakly interacting nature and the possibility of mass production during the big bang. Therefore, it may be possible to hit two birds with one stone, if axion is discovered. Axion haloscopes, the most promising axion dark matter experiments such as ADMX [9], IBS/CAPP [10], utilize microwave cavities to search for axion of mass in μeV scale. These experiments operate at ultra-high magnetic fields in order to convert axions to photons through the inverse Primakoff effect [11]. Then, axion converted photons are expected to resonate in cavities creating an electrical signal.

Light shining through a wall (LSW) experiments also use Primakoff effect for axion detection. Moreover, LSW experiments also aim to create axion in laboratory using a powerful laser beam in magnetic field where laser photons are expected to convert to axions. Then, the laser beam hits a wall where photons are blocked but axions can easily pass through it and be detected on the other side by a microwave cavity. LSW techniques is also used for the detection of a wider family of particles called weakly interacting slim particles (WISPs) including axion, hidden sector photons etc. [12]

CERN Axion Solar Telescope (CAST) is built as an axion helioscope that searching for high energy solar axions with actively tracking the sun during dawn and sunset, when the sun is close to horizon. As of 2018, CAST has become also an axion haloscope, searching for dark mater halo axions with 2 independent cavity experiments: RADES [13] and CAST-CAPP. CAST-CAPP uses 4 cavities designed, constructed, and installed on CAST in cooperation with IBS/CAPP at South Korea. Figure 1.1

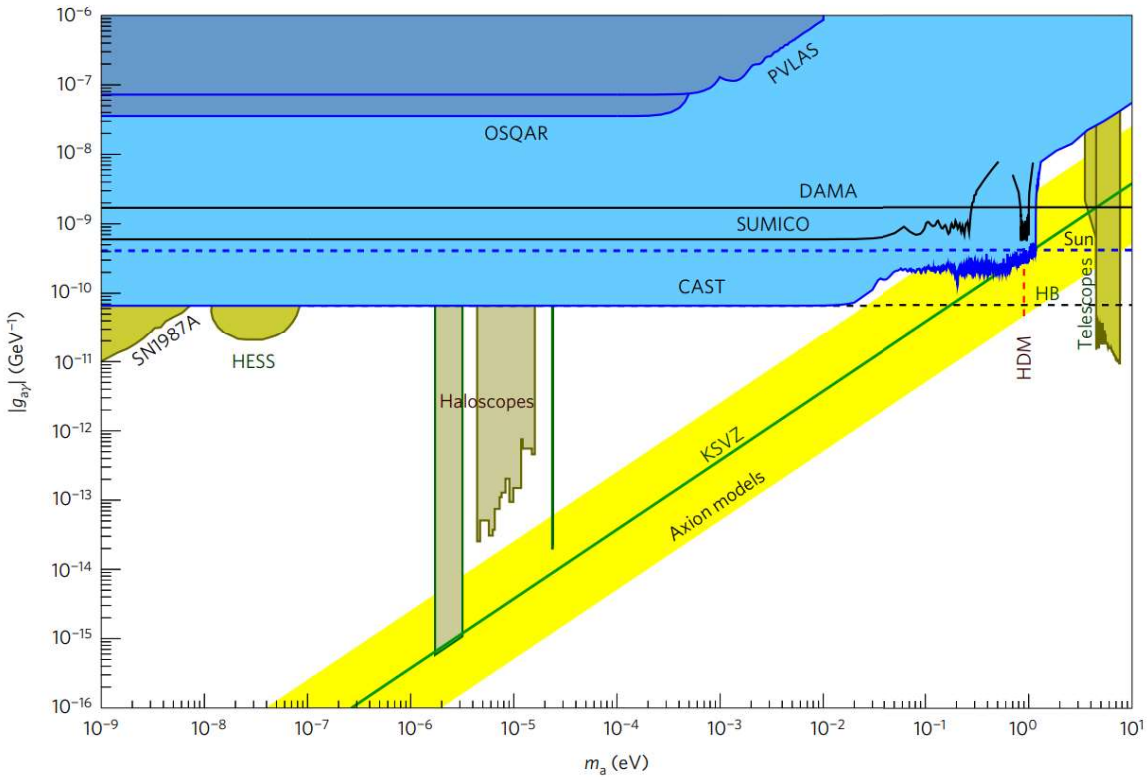

Figure 1.1. Axion-photon coupling exclusion limit. [1]

shows he exclusion plot of axion-photon coupling as of 2017. [1] Apparently, CAST has spanned the broadest range in axion photon coupling vs mass parameter space as an axion helioscope. Still, axion haloscopes are evidently the strongest tools to scan low mass (dark matter candidate) axion with KSVZ sensitivity.

1.1. CERN Axion Solar Telescope (CAST)

CAST consists of 10 meters long, decommissioned LHC dipole magnet with 43 mm diameter twin magnet bores which can apply 9 T transverse magnetic field (see Figure 1.3). Object of CAST is to detect axions and weakly interacting particles that can contribute to the understanding of quantum chromodynamics (QCD) and provide an explanation to the dark matter and dark energy phenomena. The CAST magnet is utilized as axion-to-photon converter through (inverse) Primakoff effect, the phenomenon that is also responsible for axion production in the sun. [14] To align the beam pipe with the sun, CAST magnet is installed on a tracking table that can

rotate ±8° vertically and ±40° horizontally. Thus, CAST can track the sun for 1.5 hour for each sunrise and sunset (3 hours a day). These limitations are required by the cryogenic system supporting superconductivity of the magnet at 1.8 K. Non-tracking time is mainly devoted to background measurements. [15]

Axion experiments explore $m_a - g_{a\gamma\gamma}$ parameter space which is partially explored by scanning over a wide range of axion mass. Still, none of these experiments have the facilities to scan the whole range with high sensitivity. CAST stands out among its counterparts with its LHC dipole magnet and the various detectors mounted on it which allow scanning of a wider axion mass range with high sensitivity.

An X-ray telescope (XRT) employs a focusing mirror system to focus photons, converted via Primakoff effect, on a detector. (See Figure 1.4) Detectors are conventionally installed on one of the two ends of the dipole magnet (Figure 1.3). CAST uses several detectors to search for photons resulting from axion-to-photon conversion such as the micro-mesh gaseous structure (Micromegas) detector [16], integrated grid (InGRID) detector [17], silicon drift detector (SDD). [18] Using these techniques, researchers at CAST have been determining the precise bounds for the axion-to-photon coupling constant $g_{a\gamma\gamma}$ for a given axion mass m_a. CAST reported the most advanced exclusion limit on the axion-photon coupling to be $0.66 \times 10^{-10} GeV^{-1}$. [1]

Figure 1.2. CERN Axion Solar Telescope (CAST).

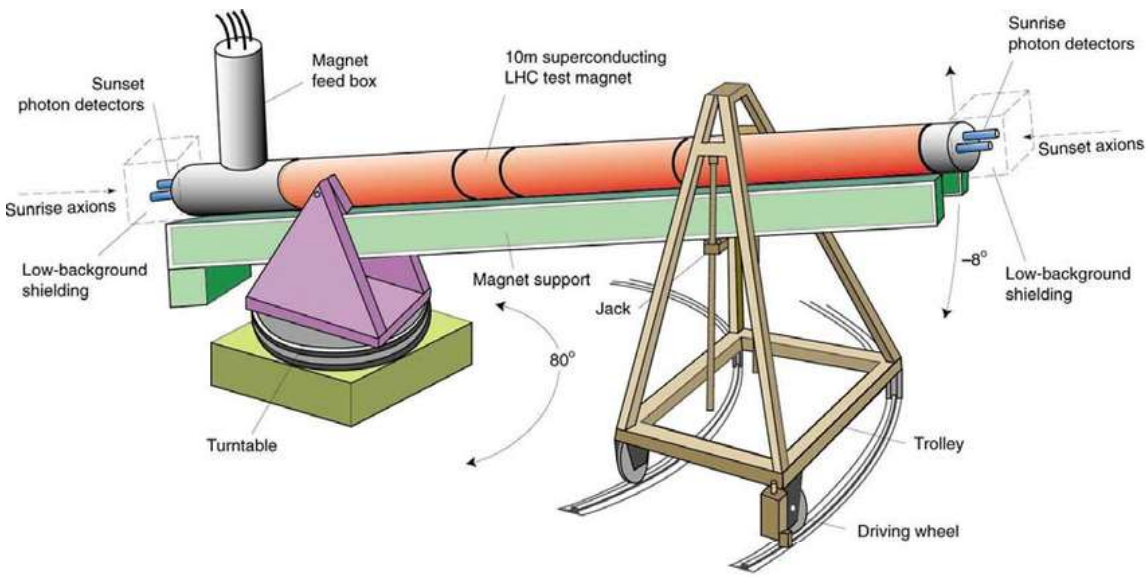

Figure 1.3. CAST layout. [2]

Coherence is an important factor that affects the sensitivity of the experiment. To avoid destructive axion-photon interference, length L of the magnet should obey the inequality in Equation 1.1. [14]

$$L < \frac{2\pi\omega\hbar^2}{m_a^2 c^3} \tag{1.1}$$

where, ω is the angular frequency of the photon. For $L = 10$ m, the coherence condition turns out to be $m_a \leq 0.02$ eV. Studying higher mass ranges requires filling the beam pipe with gas. This gives photons an effective mass and coherence is restored once the axion and photon masses match. Gas pressure can be adjusted to detect axions with higher masses. [15]

To scan a wide spectrum of axion masses, CAST has been operated with cold bores at vacuum ($m_a \leq 0.02$ eV) or filled with ^{4}He ($m_a \leq 0.39$ eV) and ^{3}He ($m_a \leq 1.18$ eV). CAST has become the first axion helioscope experiment that reached the KSVZ axion line where KSVZ is an axion model that predicts the presence axion particles as a result of spontaneously broken Peccei-Quinn symmetry. [19] [20]

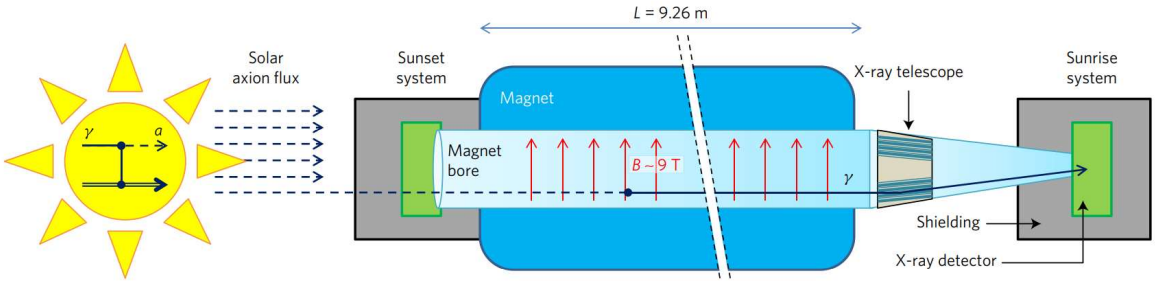

Figure 1.4. Schematic of CAST as an axion helioscope. [1]

In addition to axions, CAST also searches for other exotic particles of cosmological interest such as chameleons which may account for the dark energy problem (accelerating expansion of the universe). Their detection at CAST is supported by two channels. First, chameleons can be converted to photons through Primakoff process. Second, chameleons can directly interact with matter and their radiation pressure can be measured opto-mechanically. A kinetic weakly interacting sub-eV particle (KWISP) detector utilizes the latter channel in which XRT focuses chameleon beams on thin (50 nm) Si3N4 membrane which in positioned at the node of the standing wave inside Fabry-Perot cavity. A laser beam is frequency locked to the cavity. Any displacement of the membrane causes cavity mode frequencies to shift making the instrument capable of sensing tiny forces (on the order of 10^{-14} N) on the membrane. [21]

1.2. CAST-CAPP

Potential capabilities of CAST have been improved year by year as different detection mechanisms were employed. Apex of all these developments is the installation of resonant cavities into the cold magnet bores of CAST through a transfer of equipment and know-how from the Center for Axion and Precision Physics Research (CAPP) of Institute for Basic Science (IBS) of the Korea Advanced Institute of Science and Technology (KAIST). This axion dark matter detector project is called CAST-CAPP.

Resonant cavities are operated to detect the electromagnetic signal in resonance with the axion field in the presence of a high magnetic field. This development is a milestone for CAST as it becomes the first axion experiment to search for both

solar (helioscope) and galactic halo (haloscope) axions. Haloscope technique is used by several experiments such as the Axion Dark Matter eXperiment (ADMX) and CAPP for axion search where photons converted from axions through Primakoff effect resonate in these cavities and generate power as given in Equation 1.2. [9] [10]

$$P \approx g_{a\gamma\gamma}^2 B^2 V \rho_a C Q m_a^{-1} \tag{1.2}$$

where B is the magnetic field, V is the cavity volume, ρ_a is the local axion density, C is the geometry factor of cavity mode, Q is the quality factor of the cavity resonance mode (the ratio of the cavity stored energy to its losses of power) and m_a is axion mass. Given the common average experimental parameters P is expected to be of order 10^{-22}W requiring a very sensitive instruments for detection. These cavities can be tuned to different resonance frequencies by electronically moving a rod inside the cavity. The resonance frequency that the cavity is tuned to determine the axion mass range to which the cavity is sensitive. That is, resonant frequency of a cavity $f \sim m_a c^2/h$ boosts the generated power for corresponding axion mass, m_a. In 2015, CAST started a collaboration with CAPP to implement microwave cavities in the CAST magnet in search of axions around $m_a \sim 20$ μeV. [4]

Rectangular cavities, a novel geometry in axion physics, will enable CAST-CAPP to examine unexplored fields on the $m_a - g_{a\gamma\gamma}$ parameter space. Owing to its ∼9 T, ∼9 m magnet bores (although we have not yet filled the whole space in the CAST magnet with CAST-CAPP cavities), CAST-CAPP can exploit high B^2V leading to a relatively better power output (Equation 1.2). Currently, CAST-CAPP is able to scan for axion signals in $\sim 20 - 30$ μeV mass range. In Section 4.8, we discuss how we can expand this region as well as how to enhance our sensitivity in the whole axion mass range of interest to CAST-CAPP.

2. AXION THEORY

2.1. Strong CP Problem

CP is the combination of two symmetries of the nature: Charge conjugation symmetry (C) and Parity (P). C transforms all the particles in a system to their antiparticles. That is, C inverts the sign of electric charge and other internal quantum numbers (lepton and baryon numbers, strangeness etc.) of a particle while leaving spin, mass, momentum and energy untouched. P transformation flips the signs of all three spatial coordinates.

Gravity, electromagnetism, and the strong nuclear force are symmetric under both C and P transformations. That is, physics laws are invariant when a particle is exchanged with its antiparticle or the coordinates are transformed from a right-hand to left-hand system, or vice versa. In contrast, both C and P symmetries are broken by the weak force. In 1957, the studies of β decay of Cobalt-60 and meson decays to electron and muon revealed that neutrinos produced by weak interaction are left-handed, that is, the spin of neutrino is in the opposite direction of its velocity, whereas an antineutrino is right-handed. [22] This indicates the P symmetry is broken for the weak force. Moreover, since the chirality is inverted in particle-antiparticle interchange, C symmetry is also broken. Still, it seemed then CP is conserved for the weak force because when a neutrino (left-handed) is transformed by both C and P, it becomes a right-handed antineutrino as expected. However, in 1964, the studies of the Kaon decay showed that CP symmetry is also broken by the weak force. [23]

Mathematical formulation of the quantum chromodynamics (QCD) allows for CP violation. Equation 2.1 shows QCD Lagrangian of

$$\mathcal{L}_{\mathrm{QCD}} = \sum_i \bar{\psi}_i \left(i(\gamma^\mu D_\mu)_{ij} - m_i \, \delta_{ij} \right) \psi_j - \frac{1}{4} G^a_{\mu\nu} G^{\mu\nu}_a - \frac{g^2 \bar{\theta}}{32\pi^2} G_{\mu\nu} \tilde{G}^{\mu\nu} \tag{2.1}$$

where i is an index over quark flavors, ψ_i is the quark field, γ^μ is the Dirac matrices, m_i is the quark mass and $G_a^{\mu\nu}$ is the gluon field tensor, similar to the electromagnetic field strength tensor, $F^{\mu\nu}$ and g is the strong coupling constant. For a non-zero $\bar{\theta}$ angle the last term of the Lagrangian is expected to violate CP symmetry. Yet not a single case of CP violation is observed for the strong force. Measurements of the electric dipole moment of the neutron are used to get an insight into the value of $\bar{\theta}$. Experimental limit on the electric dipole moment of the neutron ($d_n \lesssim 10^{-28} e \cdot m$) is roughly a billionth of the value that would be generated given a CP violating strong force. [24] This brings about a fine tuning problem with $\bar{\theta} \leq 10^{-9}$ that results in CP invariance of the strong force when there is no know reason concerning QCD. [25]

2.2. Peccei-Quinn Theory and Axion

The most credible resolution to the strong CP problem was formulated in 1977 by Roberto Peccei and Helen Quinn. [26] [27] Their solution accepted θ angle a dynamical variable, as opposed to a constant, which is a byproduct of a new field, namely, axion. As a result of the axion field a new term can be added to the Lagrangian (Equation 2.1) to account for the effective potential of the axion field (Equation 2.2).

$$V_{eff} = \frac{a\xi}{f} \frac{g^2}{32\pi^2} G^a_{\mu\nu} \tilde{G}^{\mu\nu}_a \tag{2.2}$$

Peccei-Quinn theory states the last, CP violating, term of the QCD Lagrangian in Equation 2.1 cancel out with this addition as shown in Equation 2.3 ensuring that there is no net term that can possibly cause CP violation.

$$-\frac{\langle a \rangle \, \xi}{f} = \bar{\theta} \tag{2.3}$$

As a result of the proposed field, Peccei-Quinn mechanism predicts the presence of a neutral, light, pseudoscalar particle, axion. Experiments that aim to verify Peccei-Quinn Theory develop ways to detect axion through its coupling to other particles, mostly photons.

2.3. Axion-photon Conversion

Axion may couple to photons through Primakoff effect [11] via two channels: An axion my decay to two photons in vacuum (Figure 2.1(a)) or in the reference frame of a static electromagnetic field an axion may decay to a photon (Figure 2.1(b)). Coupling of axion and electromagnetic field is expressed with the Lagrangian in Equation 2.4. [1]

$$\mathcal{L} = -\frac{1}{4} g_{a\gamma\gamma} F_{\mu\nu} \tilde{F}^{\mu\nu} a = g_{a\gamma\gamma} \vec{E} \cdot \vec{B} a \tag{2.4}$$

where $g_{a\gamma\gamma}$ is the coupling constant, $F_{\mu\nu}$ is the electromagnetic field tensor, a is the axion field. $\vec{E}$ and $\vec{B}$ are electric field (associated with photons) and magnetic field (of the magnet), respectively. Coupling constant $g_{a\gamma\gamma}$ is inversely proportional to the axion decay constant, f_a.

$$g_{a\gamma\gamma} = \frac{\alpha g_\gamma}{2\pi f_a} \tag{2.5}$$

where α is the fine structure constant and g_γ is a model dependent constant of O(1). KSVZ (Kim-Shifman-Vainshtein-Zakharov) axion model accepts $g_\gamma = -0.97$, whereas DFSZ (Dine-Fischler-Srednicki-Zhitnitsky) model coupling is $g_\gamma = 0.36$.

Lagrangian of the coupled electromagnetic and axion scalar fields (Equation 2.6) yield the modified Maxwell equations (Equations 2.7 - 2.10) [28]

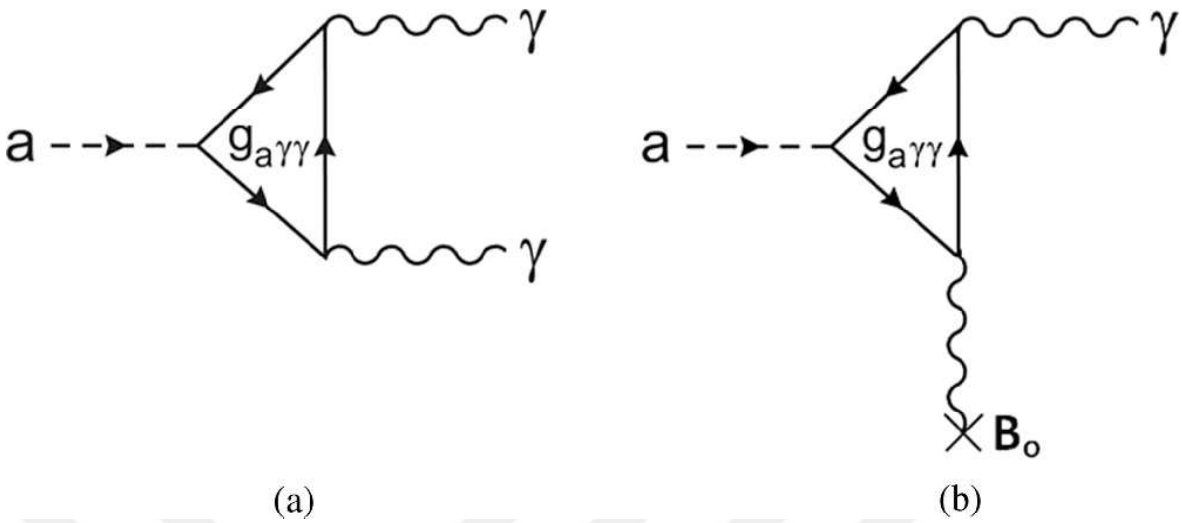

Figure 2.1. Feynman diagrams of Primakoff effect. Axion is coupling to (a) two photons in vacuum, (b) a photon in the presence of a static magnetic field (virtual photon) [3]

$$\mathcal{L} = \frac{1}{2}\left(\partial_\mu a\right)^2 - \frac{1}{2}m_a^2 a^2 - \frac{1}{4}F_{\mu\nu}F^{\mu\nu} + \frac{1}{4}g_{a\gamma\gamma}F_{\mu\nu}\tilde{F}^{\mu\nu}a \tag{2.6}$$

$$\nabla \cdot \mathbf{E} = g_{a\gamma\gamma}\mathbf{B} \cdot \nabla a \tag{2.7}$$

$$\nabla \times \mathbf{B} - \dot{\mathbf{E}} = g_{a\gamma\gamma}\left(\mathbf{E} \times \nabla a - \mathbf{B}\dot{a}\right) \tag{2.8}$$

$$\nabla \times \mathbf{E} + \dot{\mathbf{B}} = 0 \tag{2.9}$$

$$\nabla \cdot \mathbf{B} = 0 \tag{2.10}$$

where ∇ is the Laplacian operator and a single dot over a parameter indicates first order time derivative.

Nearest possible axion source to planet earth is the sun where axions are created via Primakoff process. Solar axions have energies in keV scale which can be converted back into X-ray photons by inverse Primakoff effect in high magnetic fields of the specially designed magnets of axion experiments.

Axions may also be found virialized in the halo of galaxies. Due to its relatively low velocity in non-relativistic domain, kinetic energy of halo axion is negligible compared to its mass. Therefore, the conversion photon frequency is related directly to the constant axion mass. Equation 2.12 shows this relation.

$$m_a c^2 \approx h\nu \tag{2.11}$$

$$m_a(\mu eV/c^2) \approx 4.14 \cdot \nu(\text{GHz}) \tag{2.12}$$

Microwave cavities are sensitive to dark matter axions with velocities on the order $v \sim 10^{-3}c$ with energy in μeV scale. Energy of the photon created through Primakoff process is equal to that of the converted axion. Because of a weakly interacting nature and its abundance in early universe axions have attracted the attention of scientist as a promising candidate for dark matter. Decay constant f_a for cold dark matter (CDM) axion is constrained by the astronomical observations to be 10^9 GeV $\lesssim f_a \lesssim 10^{12}$ GeV. Axion mass is inversely proportional to the decay constant.

$$m_a \sim \frac{10^{12}\ \text{GeV}}{f_a} \mu eV \tag{2.13}$$

Equation 2.13, together with the constraints on the decay constant require a dark matter candidate axion to have a mass in μeV-meV range.

2.4. Axion Signal Shape

Galactic halo axion signal shape depends on its energy distribution over frequency space. Assuming that particle energies for virialized halo axions is dominated by their mass, classical ideal gas formalism gives us the frequency distribution of virialized halo axion. Equation 2.14 shows the frequency distribution function for the axion signal.

$$f(\nu)d\nu = \frac{2}{\sqrt{\pi}}\left(\frac{3}{\nu_a\langle\beta^2\rangle}\right)^{3/2}\sqrt{\nu-\nu_a}\;\; exp\left(-\frac{3(\nu-\nu_a)}{\nu_a\langle\beta^2\rangle}\right)d\nu \tag{2.14}$$

where $\langle\beta^2\rangle = \langle v^2\rangle/c^2$. Root mean square (RMS) velocity of the galactic halo in the rest frame of Milky Way is $v_{RMS} = \sqrt{\langle v^2\rangle} \approx 270$ km/s. [29]

Calculations above are valid for an inertial observer (or a detector) in galactic frame. In the lab frame, the distribution function for energy is given Equation 2.15.

$$f_{Lab}(\nu)d\nu = \sqrt{\frac{6}{\pi}}\frac{1}{r\nu_a\langle\beta^2\rangle}\, exp\left(-\frac{3r^2}{2}-\frac{3(\nu-\nu_a)}{\nu_a\langle\beta^2\rangle}\right) sinh\left(3r\sqrt{\frac{2(\nu-\nu_a)}{\nu_a\langle\beta^2\rangle}}\right)d\nu \tag{2.15}$$

where, $r = v_{Lab}/v_{RMS} \approx 0.85$ is the ratio of the velocity of lab (earth) with respect to the galactic rest frame to RMS velocity of galactic halo. Distribution function for frequency is given by Equation 2.15. [30] RMS velocity of DM axion halo in lab frame becomes $v_{a,RMS} = \sqrt{\langle v_a^2\rangle} \approx 350km/s$. In Appendix A, we derive the axion signal.

Figure 2.2 shows the comparison of axion signal shape at $\nu_a = 5.0$ GHz. Signal widths that cover 90% of the signal power are 4.3 kHz and 7 kHz for galactic and lab frames, respectively. Figure 2.3 displays the lab frame axion signal shapes for various frequencies that CAST-CAPP is able to cover. In 800 MHz range around 5.1 GHz, signal amplitude and width both vary by $\sim 8\%$.

Quality factor Q_a of DM axion is the ratio of axion rest mass energy to kinetic energy dispersion as shown in Equation 2.16. [29]

$$Q_a \approx \frac{m_a c^2}{\sigma_E} = \frac{m_a c^2}{\frac{1}{2}m_a\sigma_{v^2}} \sim 10^6 \tag{2.16}$$

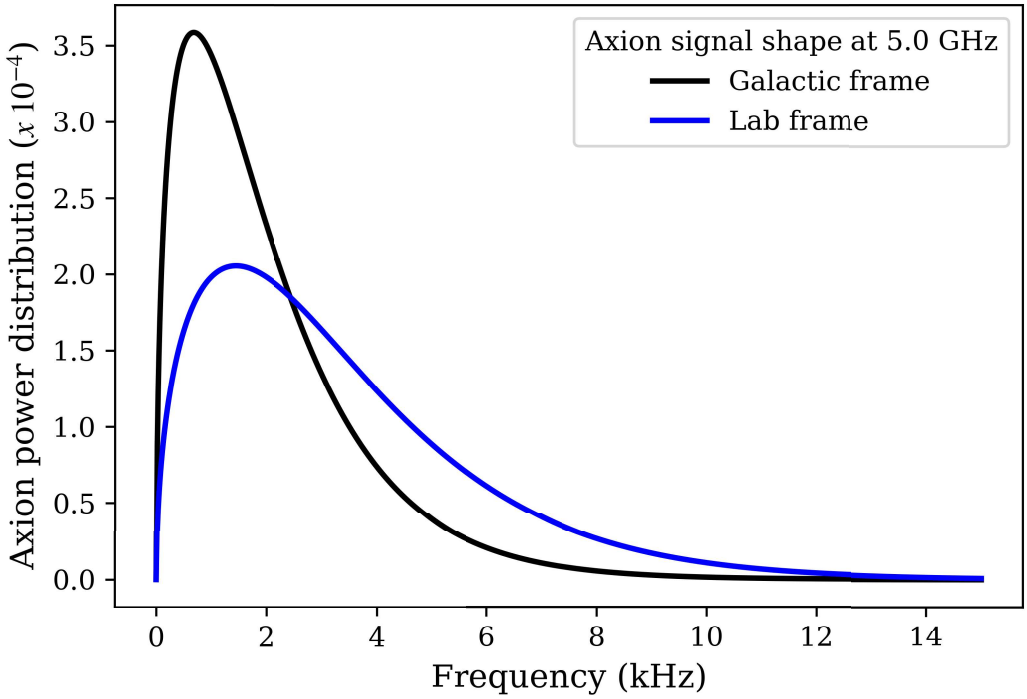

Figure 2.2. Galactic halo axion signal shape in lab vs galactic frame. Horizontal axis gives, $\nu - \nu_a$, the frequency distance from $\nu_a = 5.0$ GHz.

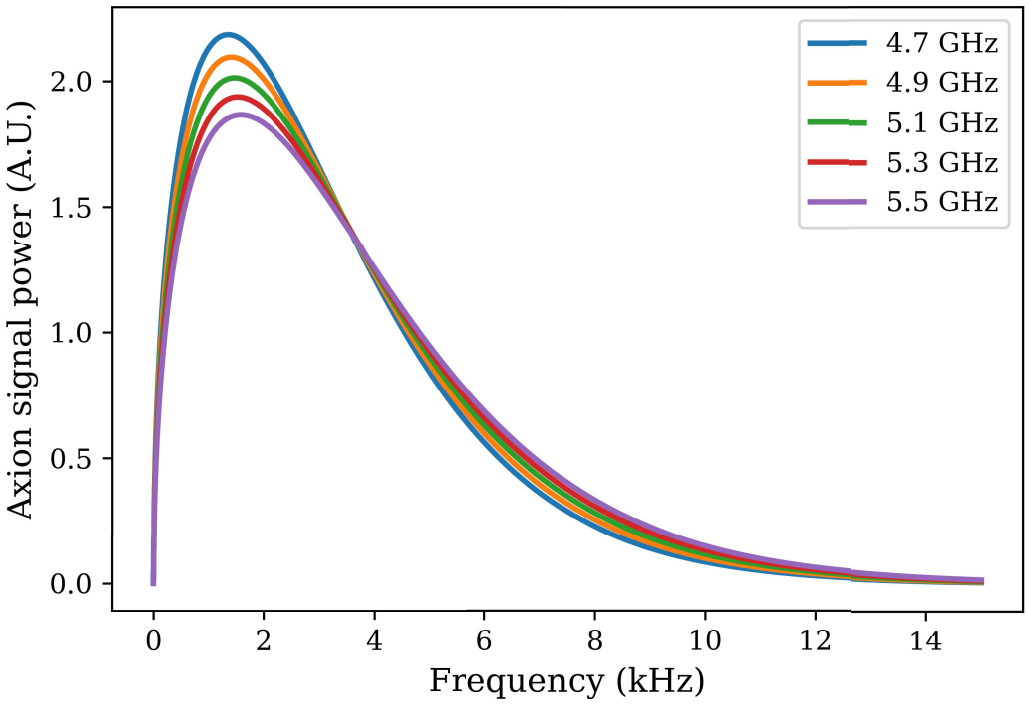

Figure 2.3. Variation of the galactic halo axion signal shape in lab frame across CAST-CAPP frequency range. Horizontal axis gives, $\nu - \nu_a$, the frequency distance from $\nu_a = 5.0$ GHz.

2.5. Axion Dark Matter Streams

Conventional theoretical models for axion dark matter assume energy densities ranging from 0.2 to 0.6 GeV cm^{-3} [31] and most axion haloscope experiments stick to the axion dark matter energy density $\rho_a = 0.45$ GeV cm^{-3}. [32] However, latest simulations suggest that even in small scales (e.g., solar system) interactions of dark matter halo with celestial bodies might result in local inhomogeneity of dark matter distribution through various mechanisms. [33] First, matter streams in a galaxy such as Sagittarius Stream in milky way can induce accompanying dark matter streams. Second, axion dark matter halo can accommodate local structures of increased axion density as a result of gravitational interaction. So called axion mini-clusters can have masses up to 10^{-12} M_{Sun}. [34] Axion dark matter mini-clusters that occur around a star, being trapped by its gravitational field, are expected to have enhanced local energy densities up to factor 10^5. Yet another mechanism is the gravitational focusing of dark matter halo by astronomical objects. Focal length of these objects depends on their mass and the axion dark matter velocity. Simulations show that at the focal point of such objects local axion density is enhanced up to factor 10^8. Even planets such as the Earth has a significant gravitational lensing capability for low-speed dark matter. [35] In the axion haloscope point of view, whatever the underlying mechanisms are, an axion dark matter stream can promote signal detection. Yet, the main drawback is that the local axion enhancement by streams is time dependent and likely to have burst like effects that may last only days or even hours. The key to detect these hypothetical short living stream effects is to scan a wide band with a fast manner. In Section 4.6.1, we explain how we try to adapt CAST-CAPP operation to increase sensitivity to transient axion streams.

3. MICROWAVE CAVITIES

CAST-CAPP uses 4 rectangular prism shaped cavities. The cavity response to a signal is determined by its geometry and material. Metal cavities ensure that the electromagnetic fields are zero on cavity walls. This boundary condition results in a quantization of field frequencies that can store resonate inside the cavity. Solution of the Laplace equation inside the cavity result in the resonance mode frequencies (Equation 3.1) as a function of the cavity geometry, L_X, L_y, L_z with mode indexes l, m, n.

$$f_{lmn} = \frac{c}{2}\sqrt{\left(\frac{l}{L_x}\right)^2 + \left(\frac{m}{L_y}\right)^2 + \left(\frac{n}{L_z}\right)^2} \tag{3.1}$$

Equation 2.4 indicates that axion-to-photon conversion probability is enhanced if the electric field of the converted photon is in the direction of the static magnetic field. Therefore, we can work with transverse electric (TE_{lmn}) resonance modes with $E_z = 0$, $n \neq 0$ and either l or m equal to zero but not both. Assuming the magnetic field in y direction, we require $E_y \neq 0$. The most fundamental mode satisfying these conditions is TE_{101} which we aim to use in our studies. Equation 3.2 yields the transverse electric field for TE_{101} mode.

$$E_y(x, y, z) = -i\frac{\pi^2 c^2}{2 f_{101} L_x} B_0 \; sin\left(\frac{\pi}{L_x}x\right) sin\left(\frac{\pi}{L_z}z\right) \tag{3.2}$$

where imaginary number i imply that $\vec{E}_y$ is out of phase by angle $\pi/2$. Figure 3.1 shows the cavity geometry and the orientations of the static CAST magnetic field and an example of a TE field (not TE_{101} for visual purposes) in the cavity. TE_{101} means that the electric field oscillates in x direction and has half a wavelength fit along the length L_z of the cavity. Substituting the dimensions $L_x \sim 0.025$ m and $L_z \sim 0.50$ m of a CAST-CAPP cavity in Equation 3.1 results $f_{101} \sim 6$ GHz. This calculation does

not take the dielectric tuning strips in the cavity which have a minor effect on the frequency.

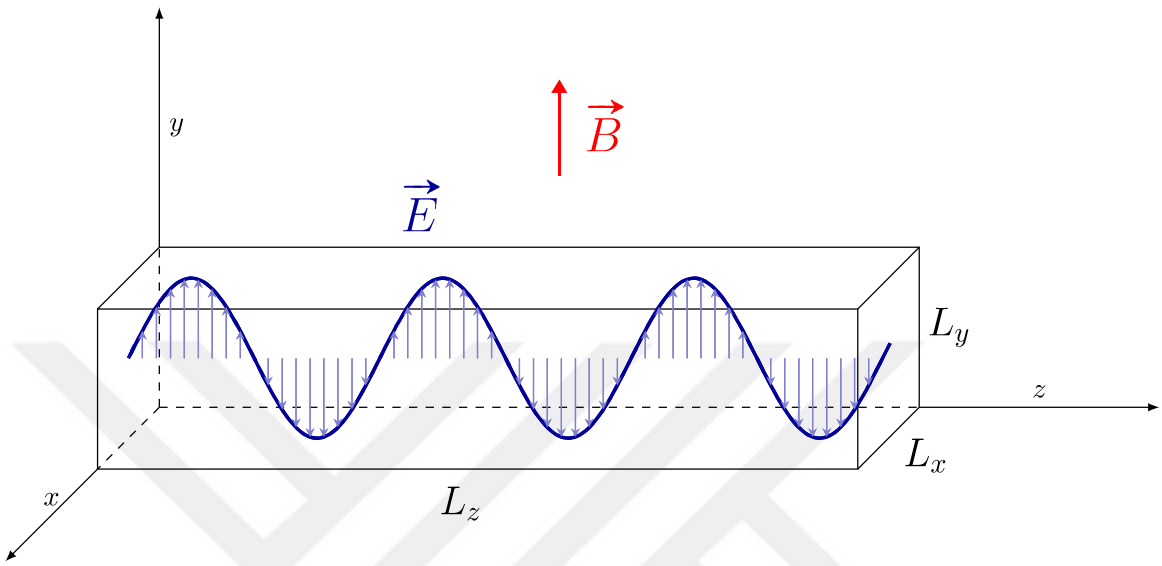

Figure 3.1. Sketch of a CAST-CAPP cavity.

Shape of a cavity resonance mode resulting from the frequency distribution the electromagnetic energy in the cavity is given by Lorentzian function in Equation 3.3 where U, $\vec{E}$, f, f_0, Q, f_0/Q are stored energy, electric field, frequency, mode center frequency, quality factor and the full width at half maximum (FWHM) of the resonance peak, respectively. [36]

$$U \propto \left|\vec{E}(f)\right|^2 \propto \frac{1}{(f - f_0)^2 + (f_0/Q)^2/4} \tag{3.3}$$

Equation 3.3 shows the frequency distribution of stored energy in a cavity implying that cavity output power is proportional to the inverse square of the frequency distance from the resonance mode center. Figure 3.2 shows the Lorentzian profile of the resonance mode.

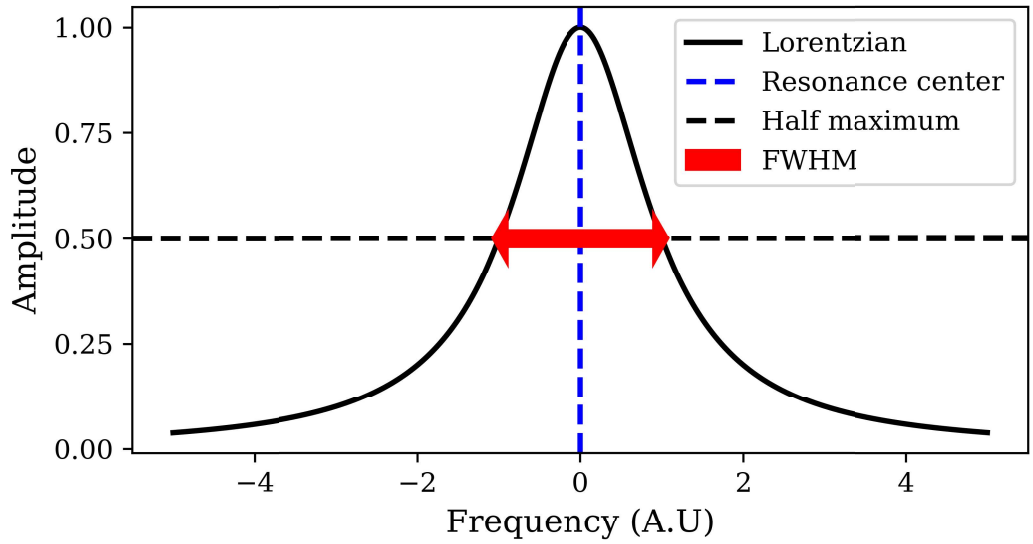

Figure 3.2. Lorentzian shaped profile of the cavity resonance mode.

3.1. Microwave Cavities in Analogy with RLC Circuits

Cavity properties around an arbitrary frequency mode can be modeled by an RLC circuit where a sole LC circuit models a lossless resonator and resistance R introduces losses. In Figure 3.3(a), blue box indicates the unloaded cavity, that is without connection to the receiver. Average power is given by

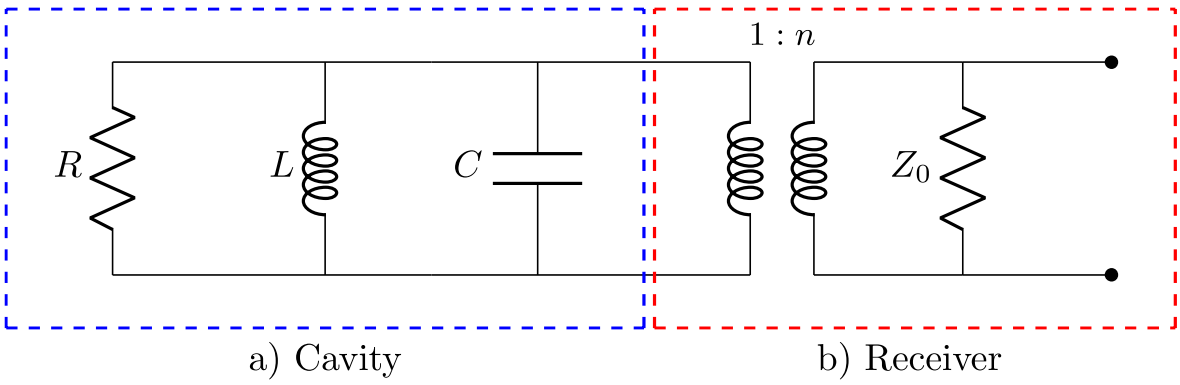

Figure 3.3. Unloaded RLC circuit as a model of a resonant cavity.

$$P_{ave} = I_{RMS}^2 R = \frac{V_{RMS}^2 R}{Z^2} = \frac{V_{RMS}^2 R}{R^2 + \left(\omega L - \frac{1}{\omega C}\right)^2} \tag{3.4}$$

where L is inductance and C is the capacitance of the unloaded circuit. Second term in the denominator is a function of the frequency. Resonance frequency of the unloaded cavity that conditionally maximizes the average power is given by

$$\omega_0 = \frac{1}{\sqrt{LC}} \tag{3.5}$$

Combining Equations 3.4 and 3.5 yields the Lorentzian shape of the resonance peak centered at $\omega = \omega_0$. Quality factor is defined as the resonance frequency divide by the full width at half maximum of the peak, $\omega_o/\Delta\omega$.

$$Q_0 = R\sqrt{\frac{C}{L}} \tag{3.6}$$

Quality factor of the unloaded cavity cannot be directly measured without a receiver which in turn alters the quality factor when added to the circuit. Red dashed box of Figure 3.3(b), represents the receiver that is coupled to the cavity with an antenna (in our analogy transformer stands for the cavity antenna). Quality factor is also defined as the energy stored in the resonator divided by the average power loss power cycle, $Q_0 = \omega_0 U/P_R$ where U is the energy stored in the cavity and P_R is the power dissipated by R. Power losses in circuit diagram in Figure 3.3 result from R and Z_0. Quality factor of the loaded circuit is

$$\frac{1}{Q_L} = \frac{P_R + P_{Z_0}}{\omega_0 E} = \frac{1}{Q_0} + \frac{1}{Q_r} \tag{3.7}$$

where Q_r is the quality factor of the receiver. Equivalent resistance of the impedance of the cavity as viewed by the receiver is n^2R, n being the transformer wiring ratio as shown in Figure 3.3. Ratio of the quality factors is equal to the ratio of the corresponding power loss terms.

$$\beta = \frac{Q_0}{Q_r} = \frac{n^2 R}{Z_0} \longrightarrow Q_L = \frac{Q_0}{1+\beta} \tag{3.8}$$

where β is called the coupling factor (of the cavity-antenna system). $\beta < 1$ and $\beta > 1$ cases are called undercoupled and overcoupled, respectively. Impedance matching ensures $\beta = 1$ which is called critical coupling and is favored as it maximizes the power transfer by minimizing the signal reflection. Equation 3.9 gives the reflection coefficient at resonance frequency. Evidently, $\beta = 1$ makes Γ vanish.

$$\Gamma = \frac{n^2 R - Z_0}{n^2 R + Z_0} = \frac{\beta - 1}{\beta + 1} \tag{3.9}$$

3.2. Geometry Factor

Geometry factor is a measure of the coupling between the resonance electric field $\vec{E}_{lmn}$ in the cavity of volume V and the static magnetic field B. Equation 3.10 shows the geometry factor for a given cavity resonance mode of parameters lmn.

$$C_{lmn} = \frac{\left| \int d^3\vec{x}\ \vec{E}_{lmn}(\vec{x}) \cdot \vec{B} \right|^2}{B^2 V \int d^3\vec{x}\ \epsilon(\vec{x}) \left| \vec{E}_{lmn}(\vec{x}) \right|^2} \tag{3.10}$$

where $\epsilon(\vec{x})$ is permittivity. Geometry factor of CAST-CAPP cavities was calculated to be 0.53 with $\sim 10\%$ uncertainty at $\nu \sim 5.4$ GHZ by simulations.

3.3. Signal Power

In order to derive the power of the signal through the cavity output antenna, we use the definition of the quality factor alternative to Equation 3.6. We can manipulate this equation to give the power dissipation through the coupling to the output antenna as shown in Equation 3.11.

$$Q = \omega_0 \frac{U}{P_{loss}} \quad \longrightarrow \quad P_{signal} = \omega_0 \frac{U}{Q_r} = \omega_0 \frac{U}{Q_L} \frac{\beta}{1+\beta} \tag{3.11}$$

where the stored energy U in the cavity due to photons converted from axions can be calculated using modified Maxwell Equations 2.7 - 2.10 [37] which results in Equation 3.12.

$$\begin{aligned} U &= \left(g_{a\gamma\gamma}^2 \frac{\rho_a}{m_a^2} \right) \frac{B^2}{\mu_0} V C_{lmn} \frac{Q_L^2}{1 + (2Q_L(\nu - \nu_0)/\nu_0)^2} \\ &= \left(g_\gamma^2 \frac{\alpha^2 \hbar^3 c^3 \rho_a}{\pi^2 \Lambda^4} \right) \frac{B^2}{\mu_0} V C_{lmn} \frac{Q_L^2}{1 + (2Q_L(\nu - \nu_0)/\nu_0)^2} \end{aligned} \tag{3.12}$$

where α is the fine structure constant, $\hbar$ is the reduced Planck constant, c is the speed of light and μ_0 is the Vacuum permeability. Equation 3.13 gives the power of the axion induced EM signal in a cavity. Table 3.1 gives an account of the parameters in Equations 3.12 and 3.13.

$$P_{signal} = \left(g_\gamma^2 \frac{\alpha^2 \hbar^3 c^3 \rho_a}{\pi^2 \Lambda^4} \right) \left(\omega_0 \frac{1}{Q_L} \frac{\beta}{1+\beta} \right) \frac{B^2}{\mu_0} V C_{lmn} \frac{Q_L^2}{1 + (2Q_L(\nu - \nu_0)/\nu_0)^2} \tag{3.13}$$

Equation 5.25 in Section 5.9 is the modified equivalent of Equation 3.13 for the experimental parameters of CAST-CAPP.

Table 3.1. Parameters that contribute to axion power in an RF cavity.

Symbol	Name	Constants
$g_{a\gamma\gamma}$	Axion-photon coupling	$\alpha \lvert g_\gamma \rvert m_a \pi^{-1} \Lambda^{-2}$
g_γ	Unitless coupling constant	-0.97 (KSVZ), 0.36 (DFSZ)
ρ_a	Axion DM energy density	$\approx 4.5 \times 10^{14}$ eV/m^3
m_a	Axion mass	Unknown
Λ	A constant parameter	$\approx$ 78 MeV

4. CAST-CAPP EXPERIMENT

4.1. Hardware

CAST-CAPP is installed on the sunrise side (left side of the CAST on the photograph in Figure 1.2) where solar axion detectors were once installed. Cavities and piezo electric tuner motors and amplifiers are installed in the CAST magnet bore kept at 2 K and 9 T. Controller PC, vector network analyzer (VNA), spectrum analyzer, data recorder and power supplies of temperature sensors, piezoelectric motors and amplifiers are installed on an instrument rack on the CAST supporting trolley platform. Figure 4.1 shows the connection scheme of the instruments in CAST-CAPP setup. [1] Indicated on the figure are Keysight N9030B PXA spectrum analyzer for cavity antenna (1), Agilent E5063A vector network analyzer (2), National Instruments FSW-0020 signal generator (3), RF switches by Mini-circuits (4), post-power combiner amplifier (5), custom-made power combiner (6), adjustable attenuators (7), power splitter to match the frequency references of the devices in our setup to that of the source device, Keysight N9030B PXA spectrum analyzer (8), local area network modem (9), Bird IQC5000 Data recorder and its RAID storage (10), commercial external antenna (11) and its Keysight EXA N9010A spectrum analyzer (12), LakeShore T-Monitor 224 temperature monitor (13), power supply of the external amplifiers (14), pre-power combiner amplifiers (15), 300 K flange on CAST magnet (16), cavity frequency tuner's piezoelectric motor's power supply (by JPE) (17), power supplies of the amplifiers (Low Noise Factory LNC4-8D) on cavities (18), webcam (19) to monitor displays of (18). local storage drives of 23 TB in total (20), computer with 8-core Intel i7 processor and high-speed SSD drive (21), USB ports connected to PC (22).

[1] Figure by Spyros and Marios Maroudas

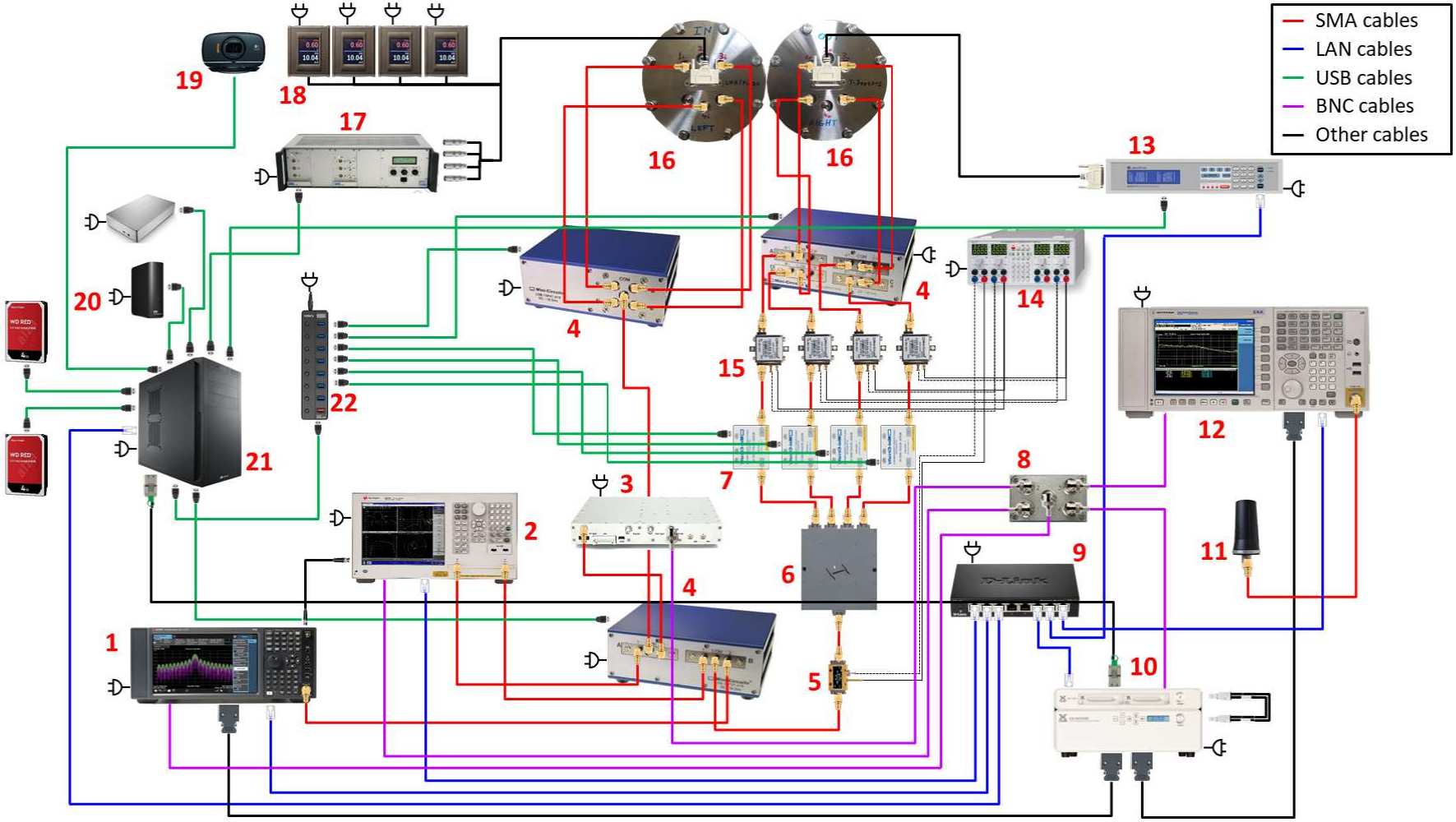

Figure 4.1. CAST-CAPP experiment setup devices and connections. Names of the instruments are given in text.

Figure 4.2 shows the cavity connections through the CAST cryostat layers. CAST hall is at room temperature ∼300K where signal generator, network analyzer, spectrum analyzer, power combiner and RF switches are installed. These instruments are connected to the 300K flange on CAST cryostat. All cables are connected to 2K flange through a clamp on the copper vessel kept at 70K. Inside the CAST magnet are the four cavities and their low noise amplifiers. Signal output of each cavity is connected to the power combiner through 2 amplifiers, one at 2K chamber on the cavity, the other at room temperature outside CAST. The single output of the power combiner is connected to an RF switch through an amplifier. RF switch directs the signal to VNA or spectrum analyzer. Cavity signal inputs are connected to an RF switch which allows the VNA or the signal injector to send signals to a single cavity at a time.

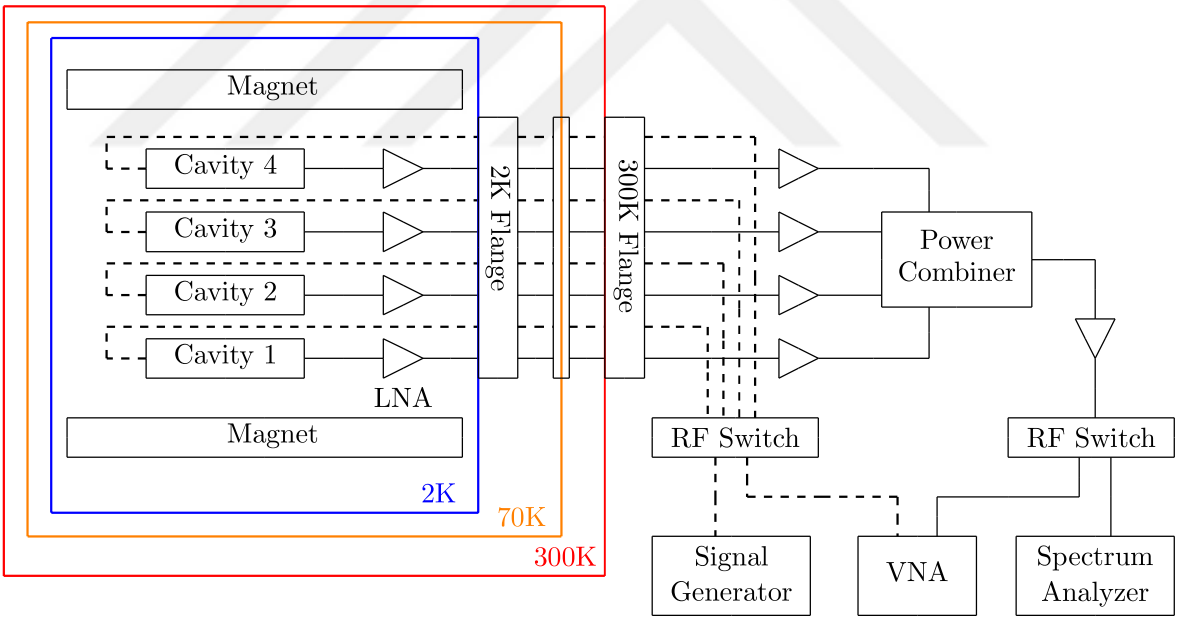

Figure 4.2. CAST-CAPP system diagram. Dashed lines indicate cavity input connections. Solid lines show receiver i.e., cavity output connections. CAST cryostat layers are indicated by colors. The drawing shows the cavities on top of each other in order to fit the diagram in the page. In reality, 4 cavities in the magnet bore are aligned on the axis of their length.

4.1.1. Cavities

CAST-CAPP employs rectangular cavities with tunable resonance frequency to scan a range of axion masses. Each of four cavities has dimensions 23 mm x 25 mm x 390 mm. Therefore, the volume of each cavity is $224 \times 10^{-6}\ m^3$. Figure 4.3 shows a CAST-CAPP cavity. On the 2 ends of the rectangular cavities, piezoelectric tuning motor and cavity locking mechanism are located, making the total length $\sim$ 50 cm. Locking mechanisms are used to fix each cavity inside CAST magnet bore. A low-noise amplifier is connected right after the coupler (antenna). Cables of the piezoelectric motor, temperature probe, signal input, and signal output are also fixed on the cavity by kapton tape.

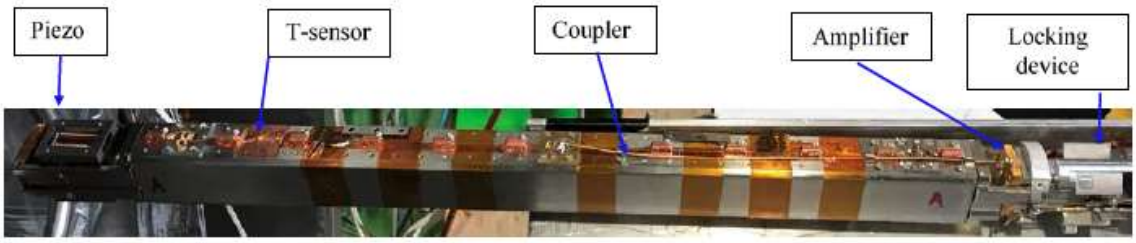

Figure 4.3. CAST-CAPP cavity.

Inside each cavity, two dielectric sapphire rods of relative permittivity $\epsilon_r = 9$ and of sizes 2.56 mm x 12 mm x 360 mm are symmetrically placed as shown in Figure 4.4 (a). As these rods move towards the center, the resonance frequency of TE_{101} mode is designed to be tuned from 4.2 to 5.8 GHz as the Figure 4.4 (b) indicates, however in reality, due to low ambient temperature in CAST magnet (2K), we are currently able to scan a frequency range, 4.75 to 5.5 GHz which corresponds to 19.7 - 22.5 μeV axion mass range. Considering the volume occupied by tuner rods, the empty volume inside each cavity is $\sim 202 \times 10^{-6}\ m^3$. [4]

Figure 4.5 shows the wheel tuning mechanism in our cavities. A coupling rod transmits the pushing force of the piezoelectric motor and rotates the wheel. Wheel is connected to two tuning plates and as it rotates the two plates are moved to the opposite sides along the long axis of the cavity.

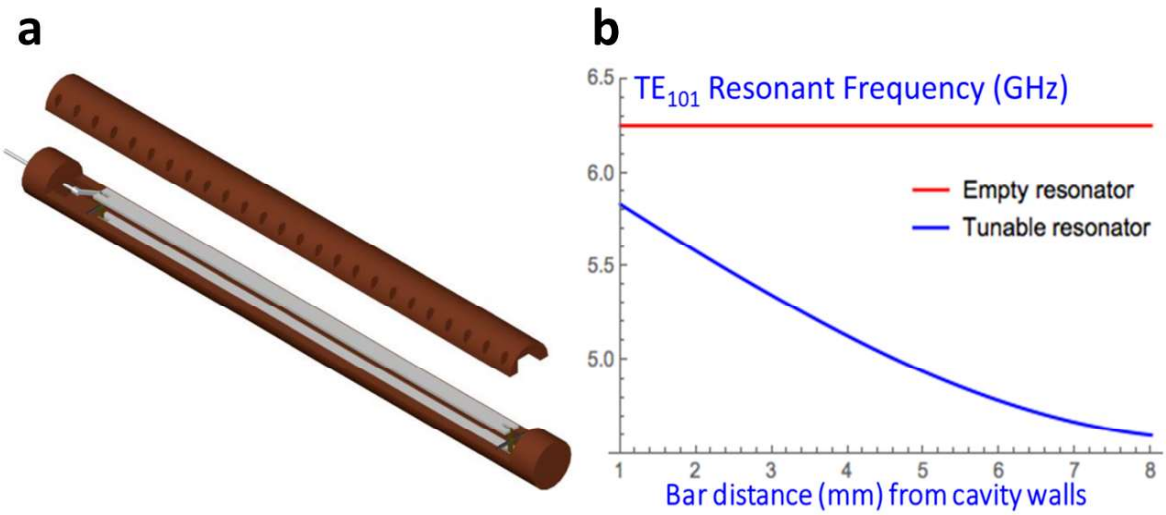

Figure 4.4. CAST-CAPP cavity inside view and tuner bars (a). Potential tuning range of the cavities (b). Resonance frequency as a function of the insulating bar positions (blue) and that of the empty cavity (red), all for TE_{101} mode. [4]

There are 4 temperature sensors are installed on CAST-CAPP that are connected to Lakeshore T-monitor 224 outside the cryostat. Single temperature sensors are installed in cavities 1 and 4. Two sensors are mounted on cavity 2. No temperature sensors are installed on cavity 3 due to limited space in the CAST magnet bore. In order to measure the temperature of cavity 3, we use the average temperature readings of two of the closest sensors from cavities 2 and 4.

Figure 4.5. CAST-CAPP tuning mechanism. Locomotive wheel and the coupling rod are indicated by red circle on both the photograph and the technical drawing.

4.1.2. Vector Network Analyzer

We use Keysight E5063A vector network analyzer (VNA) to monitor cavity resonance modes in transmission mode and to measure resonance mode frequency, amplitude and quality factor. In transmission mode, VNA sends a strong signal to the cavity through the weakly coupled input port that is sweeping the frequency span that is set by the user. Then the signal through the critically coupled cavity output is measured. Figure 4.6 shows the cavity resonance modes visualized on VNA screen in transmission mode in frequency range around ∼5.3 GHz. Each peak on the screen denotes a different resonance mode that signify a unique wavelength combination of standing electromagnetic waves in a 3-dimensional cavity. For the axion search, we are interested in TE_{101} resonance mode which is the mode with the lowest resonance frequency (leftmost on the VNA screen) and the largest geometry factor.

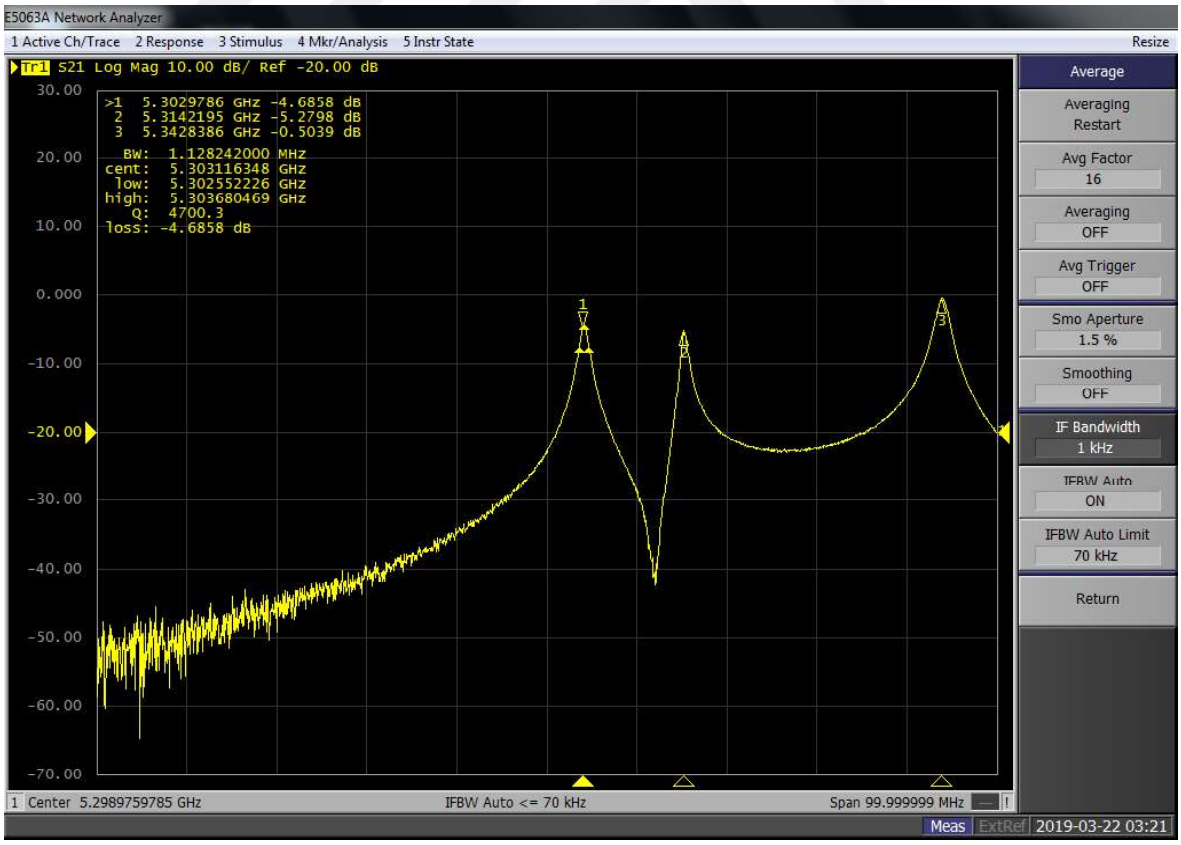

Figure 4.6. VNA monitor showing the CAST-CAPP cavity resonance modes in 100 MHZ range about ∼5.3 GHz.

4.1.3. Spectrum Analyzer

We use Keysight N9030B PXA spectrum analyzer to take axion sensitive data from the critically coupled output antenna of the cavities. In order to check the quality of the cavity output signal, we observe the noise bump of the cavity resonance mode on the spectrum analyzer. We expect that noise bump to have an amplitude at least 1 dB above the noise floor. Figure 4.7 shows the noise bump of cavity 4 for resonance mode TE_{101} which is ∼1 dB above the noise level. On the spectrum analyzer, we do not observe sharp peaks as we do with VNA, because in contrast to VNA a spectrum analyzer does not apply an input sweeping signal on the cavities.

Figure 4.8 shows the spectrum analyzer screen showing the strong test signal applied to cavity 4 by a synthesized sweeper. The test signal is depicted as a narrow blue line in the frequency domain measurement, whereas it is shown as a sine wave in the time domain.

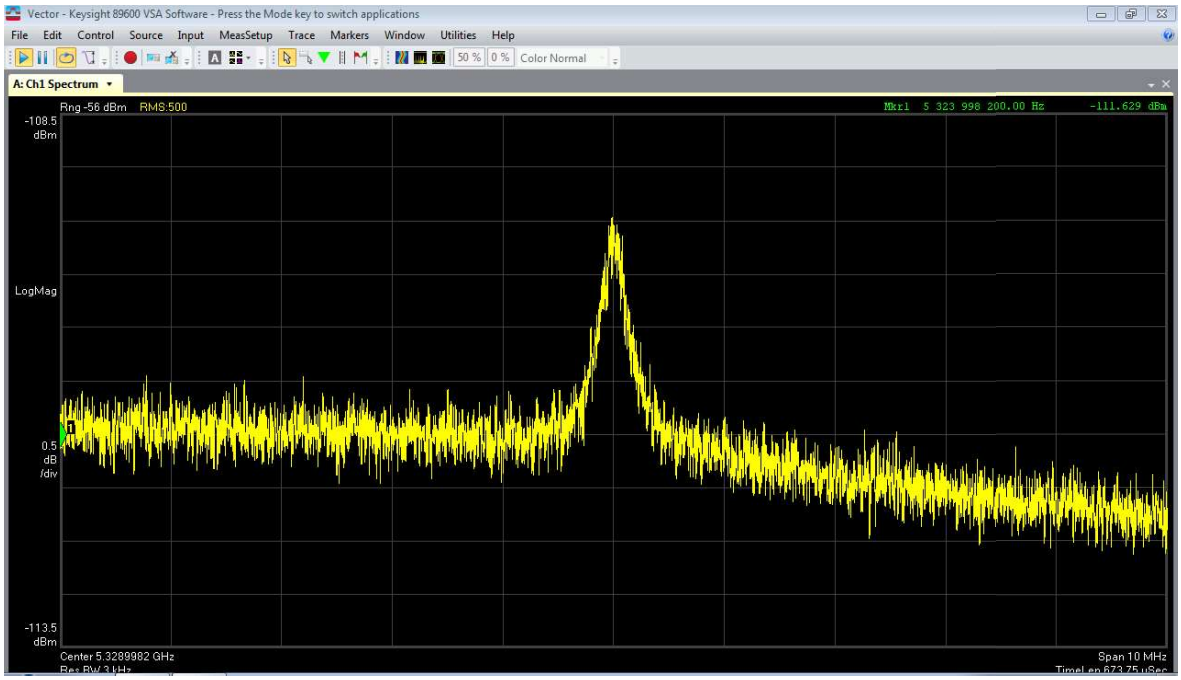

Figure 4.7. Noise bump of the cavity displayed by the spectrum analyzer indicates good quality of the receiver chain.

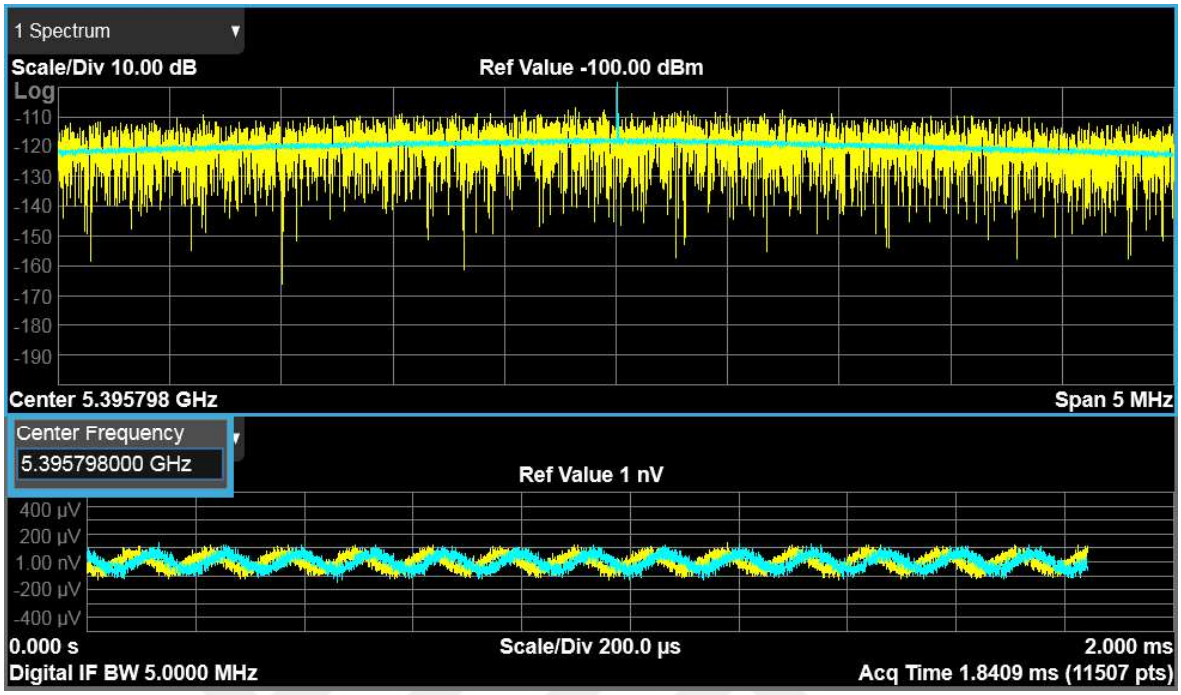

Figure 4.8. Visualization of the cavity output during a test signal injection to the cavity input. Sine shape of the test signal is visible time trace (lower part of the screen) where the complex IQ measurements are depicted as different (blue and yellow) sine waves of shifted phase. The upper box on the spectrum analyzer screen shows the frequency domain plot of the measurement where the sine wave appears as a narrow line (blue) in the middle of the screen.

In 2020 run, we also installed a second spectrum analyzer, Keysight EXA N9010A, that is connected to an external antenna mounted on CAST operating at room temperature and zero magnetic field. This receiver takes simultaneous data at the same frequency with cavity receiver. The main reason is to better identify the outlier data origins, such as EMC/EMI, and discard them easily from the candidate list. Although CAST's steel magnet body acts as a Faraday cage preventing electromagnetic signals from outside, in case there is an electromagnetic leakage a signal that is induced from outside CAST should show up in both cavity and external antenna receivers.

4.1.4. Installation in Summer 2019

In the summer of 2019, CAST-CAPP cavities were installed on the CAST magnet for the second time. First installation of CAST-CAPP, in summer 2018, served for several test on data-taking, tuning and the calibration of the setup electronics. By the end of 2018, tuners of all cavities had stopped responding and connection to cavity 4 was completely lost. Thus, it was not possible to take full advantage of the hardware let alone the phase-matching of the cavities which is the unique property that distinguishes CAST-CAPP from its counterparts.

There were only 2 installations of CAST-CAPP cavities that is the cavities were extracted only once from the CAST magnet for maintenance and improvements. The main reason for this is that the installation procedure occupies at least 1 month considering warming, disassembling, assembling and cooling the CAST magnet. Steps below define the procedure we follow to disassemble the magnet and to extract CAST-CAPP cavities:

- CAST endcap (diameter ∼1 m) is opened and moved to CAST hall. (Figure 4.9)
- 300 K flanges are removed and all cables and connectors disconnected. (Figure 4.9 -left, indicted with yellow circle.)
- 70 K clamp is removed from copper vessel of cavities. All cables and connectors inside and outside the copper vessel are disconnected. (Figure 4.9 -right, indicted with red circle.)
- Copper vessel is unmounted. (Figure 4.9 -right, indicted with red.)
- 2K clamp and flange are removed. Cavities are pulled from within the magnet bore on by one. (Figure 4.9 -right, indicted with green.)

CAST has 2 identical magnet bores. CAST-CAPP cavities are inside the bore on the right. The one on the left is used by RADES, the other cavity experiment in CAST. Figure 4.9 (right) shows the magnet bore on the right is uncovered whereas the copper vessel and the 70 K flange of the left bore are still not disassembled.

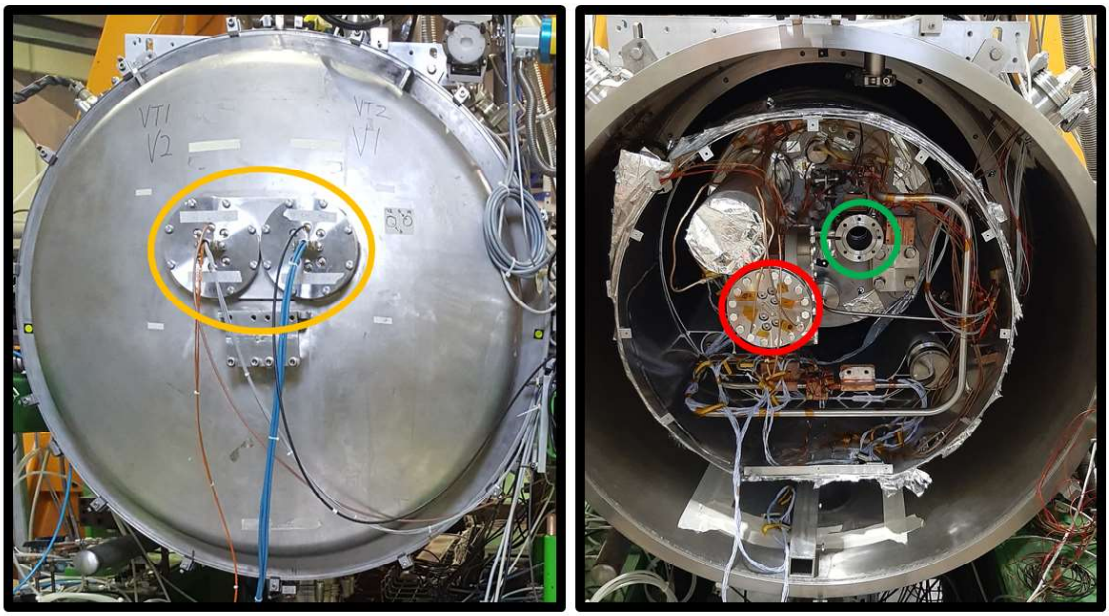

Figure 4.9. Photographs of CAST magnet closed (left) and opened (right). Several important parts are indicated with color: 300 K (warm) flange (yellow), 70 K clamp on copper vessel (red), magnet bore after 2 K flange removed (green). CAST-CAPP uses the the one on the right (green) of the two identical magnet bores.

All cavities were disassembled. Tuner systems were repaired and tested in room temperature. Vibration dampers are added to tuning plates. General maintenance of tuner motors, cavity antennas and low noise amplifiers (LNA) were carried out. Tuners are run by piezoelectric motors and supported by double springs (see Figure 4.10 (a) and (b)). When tuning towards higher frequencies we are moving with the spring force while when we tune towards lower frequencies we are moving against the springs by piezoelectric force. Tuners are calibrated by adjusting the spring forces. Temperature probes of CAST-CAPP were repaired. (In the first run, we had been relying on CAST's general purpose temperature probes only.)

We crafted cavity locking mechanism with screws and aluminum strips in order to fix the cavities and the cables (of cavity antenna, temperature sensor and power cables of tuners) so that they do not move independently in the magnet bore. (see Figure 4.10(c))

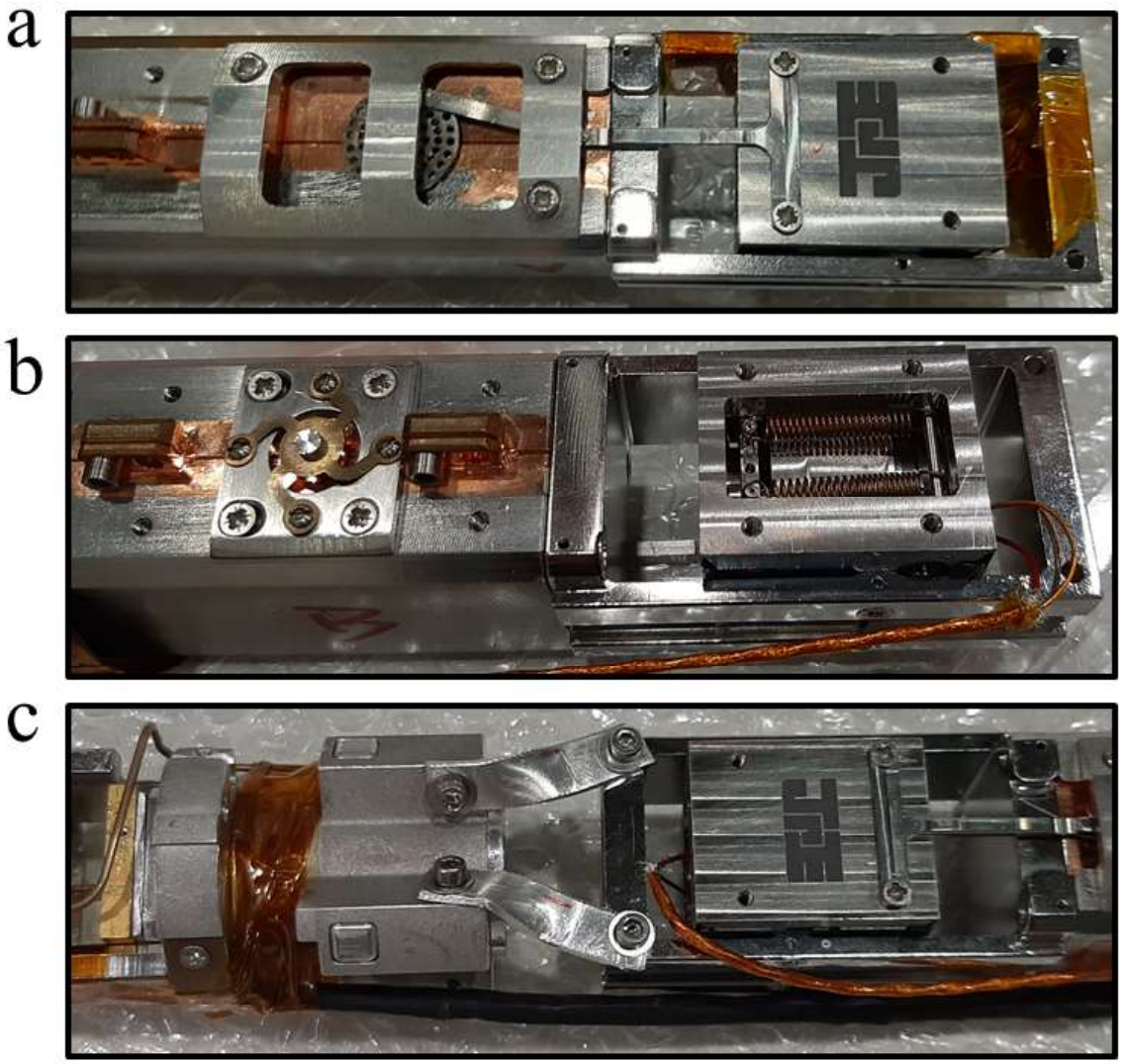

Figure 4.10. Images of piezoelectric tuner motor and its locomotive wheel (a), double springs on the rear side of the motor (b) and aluminum lock strips between 2 cavities (c).

Output signal of each cavity were tested using VNA and spectrum analyzer. Optimal and maximal tuning ranges for each cavity were determined. Table 4.1 shows the optimal and maximal frequency ranges of operation for each cavity. Figure 4.15 in Section 4.5 depicts the data-taking ranges and data acquisition times for each cavity. Cavity tuners cannot exceed the boundaries indicated by the maximal rage. Tuning outside the optimal ranges create a risk of tuner getting stuck. In Section 4.8, we discuss an upgrade of piezoelectric motors to increase the torque and therefore expand the optimal ranges.

Table 4.1. CAST-CAPP cavity tuning optimal and maximal ranges for each cavity.

	Optimal range (GHz)	**Maximal range (GHz)**
Cavity 1	5.20 - 5.34	5.13 - 5.50
Cavity 2	5.20 - 5.35	5.07 - 5.49
Cavity 3	5.25 - 5.45	5.03 - 5.50
Cavity 4	4.75 - 5.23	4.74 - 5.40

The sapphire axis holding the 2 sapphire tuning plates together inside cavity 4 had been broken after the first installation during the tuning tests. Broken shaft has a diameter of 2 mm and a length of 3.4 cm. Figure 4.11 shows the broken axis of the cavity tuner mechanism indicated by red circles on a photograph and a drawing. The broken axis was repaired by using a cryogenic glue, however this intervention caused a shift of the tuner frequency range towards lower frequencies. Luckily, it also expanded the range that cavity 4 can scan safely. (see Table 4.1)

Figure 4.11. Photograph (left) and technical drawing (b) of the broken shaft of the tuner plates in cavity 4 indicated by red circles.

4.1.5. Amplifiers

We use amplifiers in multiple stages of our receiver chain. At room temperature, we have 4 amplifiers for each cavity before the cavity output signals enter the power combiner. And an extra amplifier is connected to the output of the power combiner before the signal enters the spectrum analyzer. We also have a low noise amplifier (LNA, Low Noise Factory LNC4-8D) on each cavity in the CAST magnet which plays a key role to amplify the cavity signal when the noise is low due to low temperatures.

Figure 4.12 shows the gain and noise profile LNAs given by its manual for ambient temperature ≈ 5K. Amplifiers on the cavities is one of the 2 reasons of local heating. (The other is frequency tuning of the cavities.) When the amplifiers are off the cavity temperatures read ∼3K. When they are on and operated at with the current-voltage parameters suggested by the manual, the average temperatures rise up to 13K given the heat dissipation is 7 mW. We had optimized the operational parameters in accordance with the manufacturer to have a heat dissipation of 1.5 mW. With this optimization the cavity temperatures became ≈8 K.

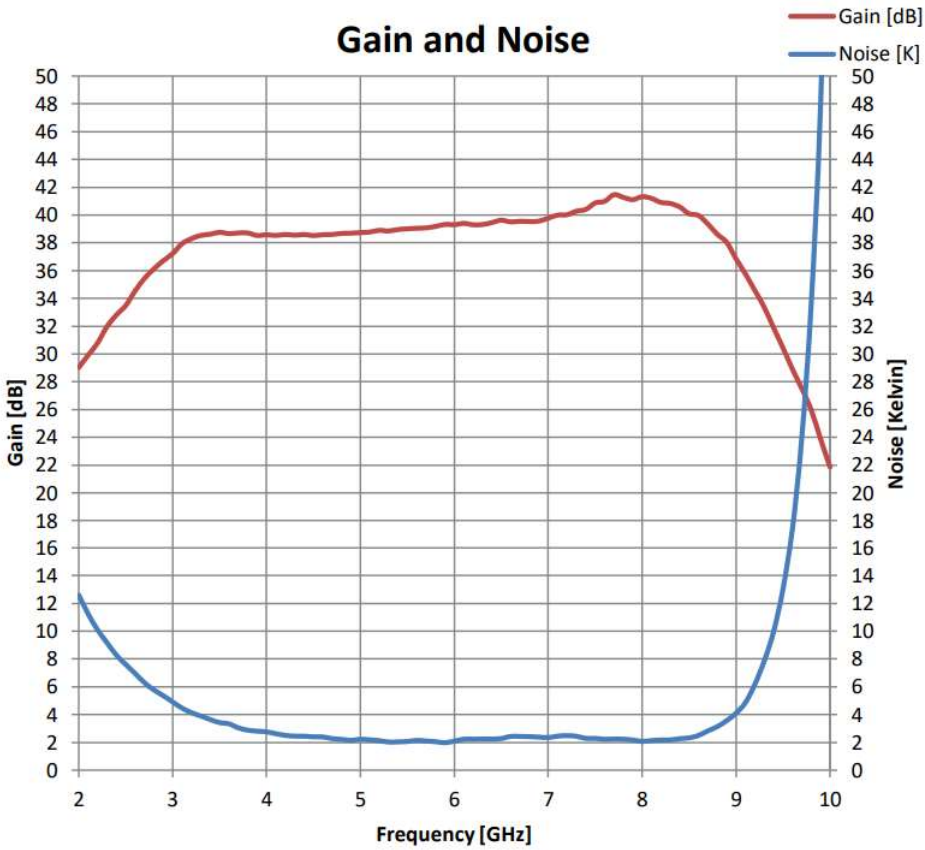

Figure 4.12. Low noise amplifier gain and noise measurement as a function of frequency at temperature ≈ 5K.

4.2. Coherence of Axion signal

It is essential for an axion detector that the axion induced electromagnetic wave phases are (approximately, if not exactly) equal over the experiment setup. That is, the axion signal through the detector should be coherent to maximize the signal strength given the assumption that axion field is coherent. We can illustrate this condition using the example of axion induced photons inside the detector. If the wave phases of these photons are changing across the detector axion signal would be attenuated considerably due to the destructive interference. Equation 1.1 in Section 1.1 introduced axion signal coherence condition for solar axion. As for the axion haloscopes that aim to detect virialized galactic axion dark matter where, contrary to solar axions, the kinetic energy is small compared to the rest mass. The coherence condition requires the experiment size to be much smaller than the de Broglie wavelength of non-relativistic axion. Equation 4.1 gives the axion wavelength for the average axion mass $20\mu eV/c^2$ for which CAST-CAPP is coherent, considering $v/c \sim 10^{-3}$ roughly for approximate velocity of the DM in the galaxy halo. Since 4 CAST-CAPP cavities are aligned on an axis with total length of 2 meters, we can safely assume that axion signal phase over all 4 cavities are approximately equal.

$$\lambda = \frac{h}{p} = \frac{h}{m_a v_a} = \frac{hc}{mc^2 \cdot v/c} = \left(\frac{1.24\mu eV m}{20\mu eV}\right)\left(\frac{v}{c}\right)^{-1} \sim 60m \tag{4.1}$$

4.3. Combining Multiple Cavities with Phase-matching

Combination of N uncorrelated noise sources of mean power P_{single} and standard deviation σ_{single} result in a total noise of $P_{\text{total}} = NP_{\text{single}}$ and $\sigma_{\text{total}} = \sqrt{N}\sigma_{\text{single}}$. This follows from the addition of uncorrelated noise voltages V_i^u which is given by Equation 4.2 where the last term of covariance is zero and we have Equations 4.3 and 4.4 for the total voltage and powers, respectively.

$$V_{total}^2 = \left\langle \left(\sum_N V_i^u \right)^2 \right\rangle = \sum_N \left\langle (V_i^u)^2 \right\rangle + 2 \sum_N \langle V_i^u V_j^u \rangle \tag{4.2}$$

$$V_{total}^2 = \sum_N \left\langle (V_i^u)^2 \right\rangle \tag{4.3}$$

$$P_{total} = \sum_N P_i^u \tag{4.4}$$

With the assumption of N equal powers $P_i \approx P_{\text{single}}$, we get $P_{total} \approx N P_{\text{single}}$. This scaling of power for the combination of uncorrelated noise is also valid for the combination of uncorrelated signals. On the other hand, correlated noise voltages V_i^c add up as shown by Equation 4.5 using the assumption for the correlated axion signals through multiple cavities to be $V_i^c \approx V_{\text{single}}$.

$$V_{total}^2 = \left\langle \left(\sum V_i^c \right)^2 \right\rangle = \langle N^2 V_{\text{single}}^2 \rangle = N^2 \langle V_{\text{single}}^2 \rangle \tag{4.5}$$

$$P_{total} = N^2 P_{\text{single}} \tag{4.6}$$

The total power scales with N^2 for correlated signals in contrast to the uncorrelated noise where the scaling is with N. In other words, uncorrelated signals add in power whereas correlated signals add in voltage. When operated independently, signal outputs of each of N cavities are uncorrelated. In order to benefit from N^2 scaling of the signals from multiple cavities, those cavities should be phase-matched. In order to phase-match multiple cavities, first, all cavities must be tuned to the same frequency. Then, a power combiner is used to merge multiple cavity output signals. Phase-matching requires axion signal originating from all 4 cavities simultaneously must arrive at the power combiner at the same time to match the phases of sine waves (in case there is a signal) To this end, we measured propagation delays for the outputs of each 4 cavities to be in the order of 100 nanoseconds using VNA in time domain impulse mode. This delay depends mainly on the length of the wire from cavity output to the power combiner. We adjusted the wire lengths from cavity outputs to the power combined to match their propagation delays.

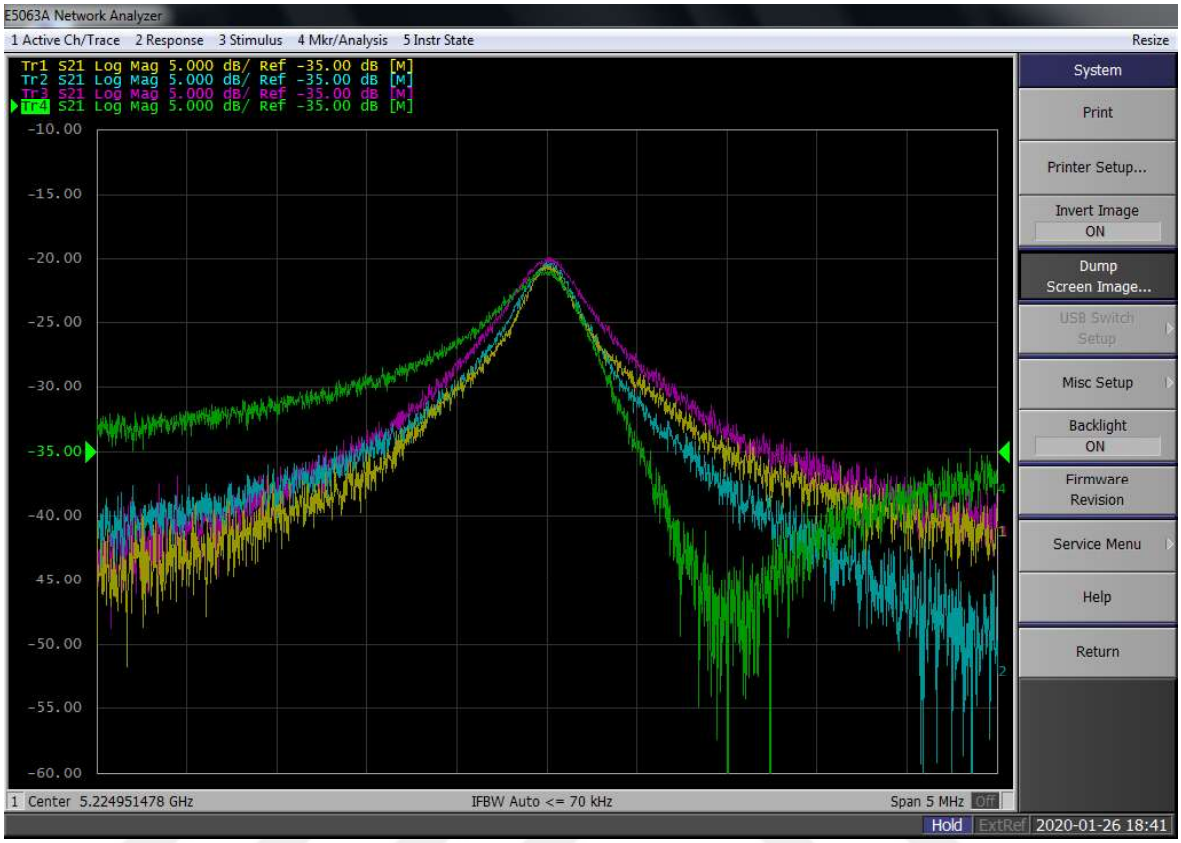

Figure 4.13. VNA screen showing that 4 cavity modes are aligned with respect to frequency and amplitude.

Figure 4.13 shows phase-matching of 4 cavities on a VNA in transmission mode. Cavities were tuned to the same frequency within ± 10 kHz and their mode amplitudes were balanced within ± 0.5 dB using attenuators as they were monitored with VNA (see). The reason of amplitude alignment of the phase-matched cavities might not be as obvious as the reason of their frequency alignment. Total noise output of the power combiner scales as $\sim \sum A_i n_i$ where the sum is over the phase-matched cavities and A_i are the cavity resonance mode amplitudes and n_i are noise. Total signal output of the power combiner scales as $\sim \sum A_i S_i$ where S_i are signal amplitudes from each cavity. In the SNR calculation for a single cavity mode amplitude terms would cancel out. In case of multiple cavities, mode amplitude terms cancel out if only all A_i terms are equal. Hence the resulting SNR for the phase-matched configuration would considerably be bigger than that of a single cavity. On the other hand, if at least one of them is considerably large, that is $A_j >> A_{i \neq j}$ then all $A_{i \neq j}$ terms in both sums would be negligible and the resulting SNR would be equal to that of a single cavity.

So, we conclude that we should have the cavity resonance mode amplitudes of the phase-matched cavities approximately equal. We are currently working to demonstrate phase-matching with signal injections to the cavities.

An important parameter in signal processing is signal-to-noise ratio (SNR) which can be defined in two ways. First is SNR = P_{signal} / P_{noise} and second is SNR = P_{signal} / σ_{noise}. Table 4.2 gives the scaling of SNR for correlated (phase-matched) and uncorrelated signals with the combination of N cavities for both SNR definitions. Coherence of the output signals thorough phase-matching of N cavities multiplies the SNR by a factor N for both definitions of SNR.

Table 4.2. Scaling of SNR with the combination of N correlated/uncorrelated signals versus noise (uncorrelated by default) for the distinct definitions of SNR.

	P_{signal} / P_{noise}	P_{signal} / σ_{noise}
Uncorrelated signal	$N/N = 1$	$N/\sqrt{N} = \sqrt{N}$
Correlated signal	$N^2/N = N$	$N^2/\sqrt{N} = N\sqrt{N}$

4.4. Data Acquisition

Data acquisition software (DAQ) operates all the instruments in our setup with Python programming language. DAQ is fully optimized to take data automatically once started with required parameter inputs. We also implement various safety measures to protect the tuners with piezoelectric motor in our cavities which are the most delicate parts of our setup. Our digital data treatment is composed of several stages:

- Data acquisition using a spectrum analyzer.
- Recording data on RAID storage system.
- Data offload from RAID system to local drive.
- Data processing on local drive with Fast Fourier Transform (FFT).
- Data analysis on local drive.
- Upload data from local drive to CERN Advanced STORage manager (CASTOR).

CAST-CAPP records time series of I/Q samples as 16-bit binary data. At each measurement, we record, along with the binary data file, a human readable header file containing data-taking parameters such as center frequency, acquisition bandwidth (span), sample rate, start and stop timestamps. I/Q couple voltage readings can be thought of as the real and imaginary components of a measurement, thus carrying the information of both amplitude and phase.

We record data in files of 1-minute measurements of file size ~ 1.5 GB. We have fixed acquisition bandwidth of 5 MHz which is well above the minimum requirements determined by cavity resonance peak width $\nu_{center}/Q \sim 300kHz$. Sampling rate is 6.25 MHz (6.25×10^6 I/Q samples per second). This corresponds to 375×10^6 data samples in a single 1-minute datafile. Each of our raw spectra has a bandwidth 6.25 MHz, however 10% on both left and right edges of the spectra are the roll-off of the IF filter. In the analysis, we crop both ends, removing 20% of the samples in each spectrum, to have refined spectra of 5 MHz bandwidth.

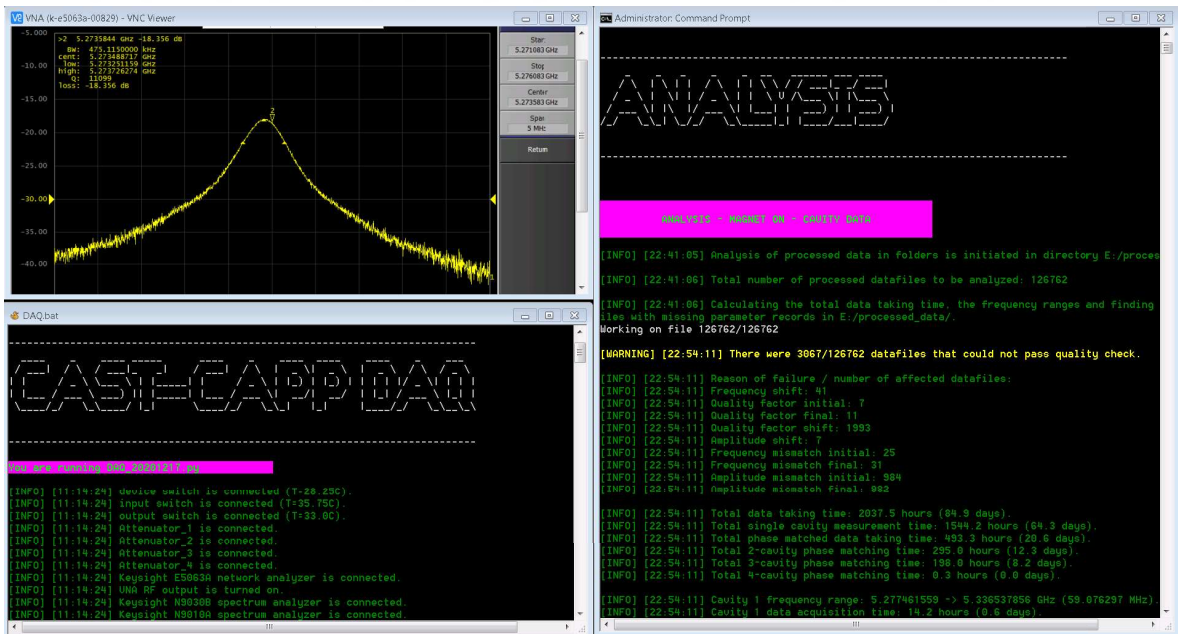

Figure 4.14. Screen of the local CAST-CAPP PC during simultaneous data-taking and analysis.

CAST-CAPP records data from two channels using two spectrum analyzers. First channel is connected to the cavities and the second channel is connected to an external antenna mounted on CAST magnet. Bandwidth and the canter frequencies of both channels are the same. The second channel was installed before 2020 data-taking run, in order to better characterize the outlier signals and their origins.

In ideal conditions, CAST-CAPP data-taking duration is limited by data offload from RAID recorder system to local drive. This process requires $\sim$ 2 hours per day and cannot be performed simultaneously with data-taking. Remaining $\sim$ 22 hours are devoted to data-taking. However, CAST hosts experiments which also require solar tracking. In the days that CAST does solar tracking, we utilize up to 18 hours per day for data taking. We prefer not to take data during solar tracking because of the increasing mechanical vibrations at CAST due to 50-ton system being moved.

As soon as the time-domain raw data is offloaded from the RAID recorder to the local PC, it is processed by Fast Fourier Transform in small chunks (explained in Chapter 5). Processed data size is 4 MB per 1-minute recording which is much smaller compared to raw data. Analysis is performed on the processed data files and we do not use the raw data anymore throughout the analysis procedure.

Considering both data channels of CAST-CAPP, we collect up to $\sim$ 4 TB of data per day. Since we do not have enough local storage at CAST for such big amounts of data, we transfer the raw data to CERN Advanced STORage manager (CASTOR) using the fiber optic infrastructure of CERN as soon as we finish processing it. We save the processed data ($\sim$ 5 GB/day) to both local drives and to CASTOR. As of December 2020, we have $\sim$ 500 TB of data stored at CASTOR.

4.4.1. Data-taking Run of 2018

This run served for tests and calibrations. Frequency tuners with piezoelectric motors were tested to identify the frequency limits of the tuners in cryogenic temperatures. We studied the oscillations of the tuning plates induced by the vibrations of CAST vacuum pumps. Due to malfunctions of several tuner and signal receiver electronics, neither of the cavities could complete the tuning tests successfully, and only cavity 4 passed signal receiving tests. CAST-CAPP took test data of 134 hours in 2018 with cavity 4 only in fall of 2018.

4.4.2. Data-taking Run of 2019

After the second CAST-CAPP installation in the summer of 2019, we completed signal receiving and tuning tests of all cavities. We automatized the data-taking with frequency tuning using our DAQ software. We developed phase-matching procedure for four cavities by improving fine tuning of the piezo tuners and by installing adjustable attenuators connected to signal channels of all cavities and a power combiner to merge and direct the signal cable to the spectrum analyzer. We demonstrated phase-matched data taking for 2, 3 and 4-cavity systems. In this period, we established the connection between the local CAST-CAPP PC and CASTOR in order to fulfill increasing need of data recording space.

During 2019 data taking run we have managed to measure successfully with all four CAPP cavities a total frequency range of 280MHz (in steps of 200kHz) for a total acquisition time of 637.9h (26.6days). More specifically, for single cavity measurements we measured for a total acquisition time of 195.3hours, with phase-matched cavities we measured for a total acquisition time of 442.6h. The total scanned ranges for each individual cavity were:

- Cavity 1: 68.913MHz (5.2860GHz – 5.3500GHz)
- Cavity 2: 157.365MHz (5.2239GHz – 5.3813GHz)

- Cavity 3: 58.653MHz (5.2836GHz – 5.3422GHz)
- Cavity 4: 135.179MHz (4.9119GHz – 5.0471GHz)

4.4.3. Data-taking Run of 2020

In September 2020, we could start CAST-CAPP data-taking run with a big delay because of COVID-19 pandemic. This also led us to skip any installations that we would like to conduct which required opening CAST magnet. Luckily, CAST-CAPP detector was working fine and ready to start a new data taking run. In 2020 run, we incorporated a second signal receiver channel to acquire electromagnetic radiation outside the CAST magnet.

4.5. Data Acquisition Statistics

CAST-CAPP has scanned a continuous range from 4.77 GHz to 5.43 GHz (660 MHz bandwidth) corresponding to axion masses 19.7 - 22.4 μeV. As of December 2020, we have recorded ∼127,000 1-minute datafiles, corresponding to a total time 85 full-day with magnetic field on, that is, sensitive to axion. Figure 4.15 shows the data-taking time of each cavity as a histogram over the frequency range. Table 4.3 gives an account of the statistics of recorded data, classified for either single cavity identities of different combinations of phase-matched (PM) cavities. Table 4.4 yields the same statistics for cavity background data taken with magnetic field off. Background data does not cover the whole frequency range as that of magnet-on data because background measurements were mainly focused around the observed candidate signals (see Section 5.14). Contributions to the statistics from discarded data are not counted. In Section 5.6 we explain our criteria to select qualified measurements.

Table 4.3. CAST-CAPP data acquisition statistics classified according to cavity identities for axion sensitive measurements taken with magnetic field on. PM denotes phase-matched cavities.

Cavity combinations	**Time**	**Frequency range**
Total	84.9 days	4.774 → 5.434 GHz (660 MHz)
Single cavity (all)	64.3 days	4.774 → 5.434 GHz (660 MHz)
PM cavities (all)	20.6 days	5.222 → 5.352 GHz (130 MHz)
PM 2-cavities (all)	12.3 days	5.277 → 5.352 GHz (75 MHz)
Cavity 1	14.2 hours	5.277 → 5.337 GHz (59 MHz)
Cavity 2	25.9 days	5.182 → 5.381 GHz (199 MHz)
Cavity 3	12.7 days	5.293 → 5.434 GHz (141 MHz)
Cavity 4	25.1 days	4.774 → 5.246 GHz (472 MHz)
PM cavities 1-2	11.2 days	5.277 → 5.352 GHz (75 MHz)
PM cavities 1-3	25 hours	5.284 → 5.299 GHz (15 MHz)
PM cavities 2-3	5 minutes	5.293 → 5.298 GHz (5 MHz)
PM cavities 1-2-3	8.2 days	5.292 → 5.330 GHz (38 MHz)
PM cavities 1-2-3-4	20 minutes	5.222 → 5.227 GHz (5 MHz)

Table 4.4. CAST-CAPP data acquisition statistics classified according to cavity identities for axion insensitive measurements with magnetic field off. PM denotes phase-matched cavities.

Cavity combinations	**Time**	**Frequency range**
Cavity 1	1.1 hours	5.285 → 5.290 GHz (5 MHz)
Cavity 2	12.5 days	5.198 → 5.342 GHz (144 MHz)
Cavity 3	2.3 days	5.329 → 5.433 GHz (104 MHz)
Cavity 4	21 hours	4.789 → 4.856 GHz (67 MHz)
PM cavities 1-2	5.2 hours	5.285 → 5.290 GHz (5 MHz)

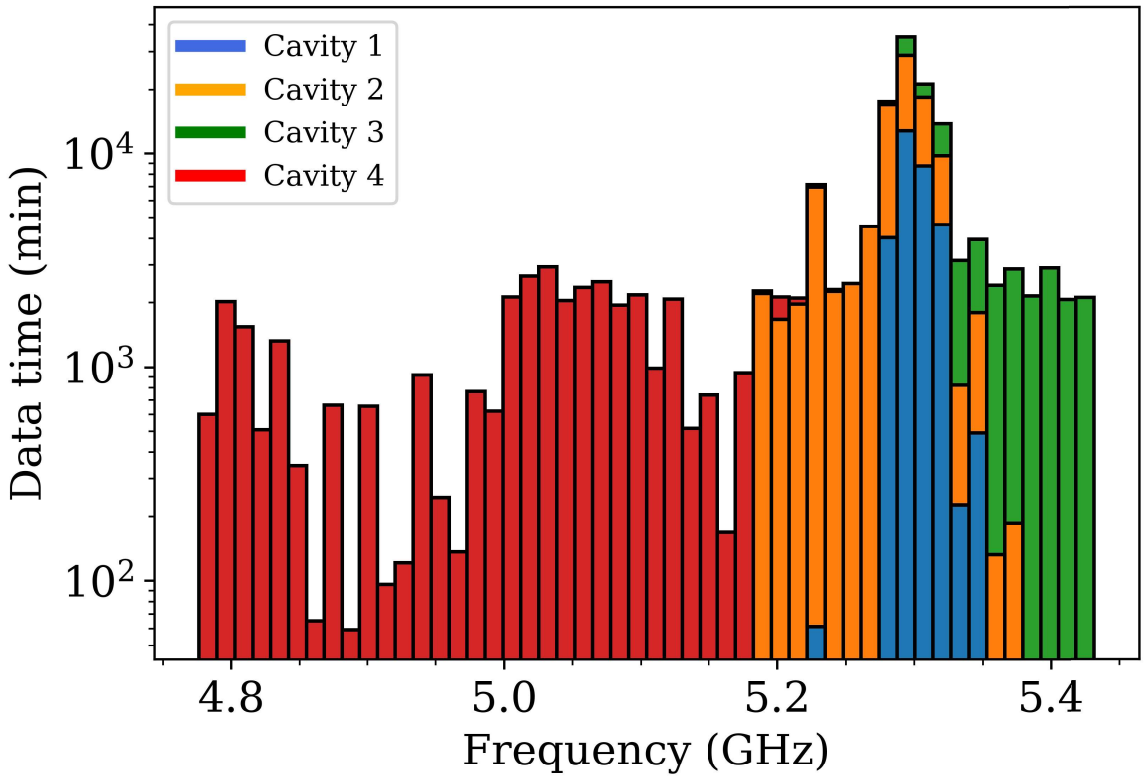

Figure 4.15. Histogram of cavity data-taking times over the frequency range. Colors denote cavities 1 (blue), 2 (orange), 3 (green), 4 (red).

4.6. Data Acquisition Strategies

4.6.1. Fast Tuning Method

CAST-CAPP focuses on two channels of axion detection. First is the detection of halo axion which is the conventional target for all axion haloscopes. Second is the detection of axion streams or mini clusters. Fast scanning method (FSM) aims to fulfill both detection channels by maximizing the sensitivity for the streaming axions while causing no setback on the sensitivity for halo axions.

Conventional haloscopes can be sensitive to axion streams on daily basis considering the anticipated huge amplification of local axion densities. Research shows that axion streams gravitational focused in the solar system can ideally boost axion densities up to the order of 10^{11}. [38] (See also the discussion in Section 2.5) However,

a significant drawback, axion streams may occur as short lasting bursts rather than being persistent as halo axions. In this case, FSM maximizes the chance of axion stream detection by scanning the broadest possible frequency range in a short time interval by tuning cavity resonance mode fast. Maximum scanning speed of CAST-CAPP cavities is 10 MHz/min. Therefore, the maximum scanning range (∼660 MHz) can be covered within ∼1 hour. Considering the data-taking times, CAST-CAPP can scan 10 MHz/hour.

FSM also requires daily analysis of the data to establish a feedback loop in search of the transient signals. This feedback loop ensures that any signal candidate is realized by the operators within a day and results in daily update of the tuning plans in order to explore the narrow bands around the transient candidate signals.

4.6.2. Wide Band Scanning

Wide Band Scanning (WBS) technique is devised as a plan b to the fast scanning method. WBS is intended for axion stream search only. It is the fastest technique to continuously scan for DM axion streams, however it lacks the sensitivity to the conventional DM axion. Idea of WBS is to keep a cavity at a constant frequency and scan a wide frequency range around the TE_{101} mode of the cavity which is sensitive to axion. Power of the cavity resonance mode is inversely proportional to the square of the frequency distance from the resonance mode center. Therefore, even for axion streams with power bursts we are likely to lose sensitivity if the signal is away from the mode center.

We measured the signal amplitudes as a function of frequency distance from cavity resonance mode's center frequency of cavity 1. We varied the input signal power from -120 to -50 dBm with 10 dBm steps and we measured the output power amplitude with respect to the noise floor with 10 MHz steps from 0 (resonance center) to -300 MHz. We could not verify the detection of signals with -120 and -110 dBm amplitudes and for frequency distance >160 MHz. Figure 4.16 shows the variation of

output signal power vs frequency distance from TE_{101} mode for B = 9T, $Q \sim 2 \times 10^4$, $T \approx 15K$, measurement time at each frequency step = 10 s. We conclude that, given the parameters above, we are sensitive to signals up to 160 MHz (for -50 dBm) away from the mode center.

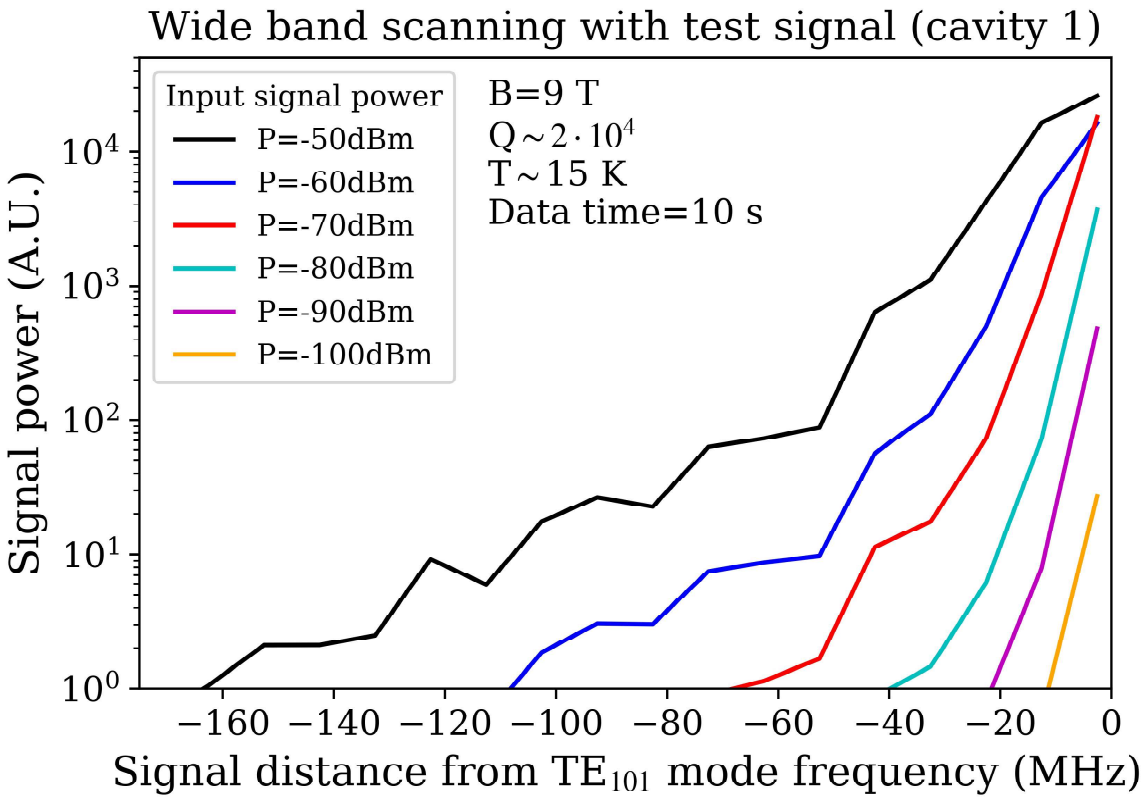

Figure 4.16. WBS test measurements with an injected (fake) signal of power varied powers. Output powers are plotted as a function of the frequency distance from TE_{101} resonance mode center.

Figure 4.16 was plotted for the left (lower frequency) side of the resonance mode because TE_{101} mode has the lowest frequency and there are other modes on its right side which would distort our measurements with injected signal. However, those resonance modes are not sensitive to an axion signal. Therefore, considering an input axion signal, we can safely assume that measured curves on Figure 4.16 are symmetric about x = 0 line.

In CAST-CAPP, we have taken WBS measurements with single cavities for test purposes. WBS is most feasible with multiple cavities tuned with a constant frequency spacing over a wide range of frequency. The frequency spacing of cavities and measurement time should be derived from the axion stream power estimations. Considering the maximum span (25 MHz) of our spectrum analyzer and the measurement time 10 s at each step we are able to sweep 200 MHz range in less than 2 minutes with WBS. Such high sweeping speeds make WBS favorable to search for axion streams with burst-like transient signals.

4.7. Sensitivity Prospects

In order to obtain an estimation of a limit on the unitless coupling g_γ as a function of total data-taking time t and data bandwidth $\Delta\nu$, we use the results of the discussion in Section 5.4. Specifically Equation 5.23 can be rewritten as

$$\frac{\Delta\nu}{t} \approx \frac{Q_a}{Q_L}\frac{\Delta\nu_a}{t} = \frac{Q_a}{Q_L}\left(\frac{[P_{\text{signal}}]_{\text{effective}}}{k_B T_s}\frac{1}{\text{SNR}_{\text{target}}}\right)^2 \tag{4.7}$$

$$\approx \frac{Q_a}{Q_L}\left(\frac{P_{\text{signal}}(\nu=\nu_0)}{k_B T_s}\frac{1}{\text{SNR}_{\text{target}}}\right)^2 \tag{4.8}$$

where $P_{\text{signal}}(\nu = \nu_0)$ is the axion conversion power exactly on the cavity resonance frequency and $[P_{\text{signal}}]_{\text{effective}}$ is the sum of the overlapping conversion powers (Lorentzian profile) as the cavity is tuned step by step over a given frequency ν. In Section 5.12, we explain $\text{SNR}_{\text{target}}$ is selected to be 5. We can write Equation 4.8 as

$$\frac{\Delta\nu}{t} \approx g_\gamma^4\left(\frac{1}{k_B T_s}\frac{1}{\text{SNR}_{\text{target}}}\frac{\alpha^2\hbar^3c^3\rho_a}{\pi^2\Lambda^4}\omega_0\frac{\beta}{1+\beta}\frac{B^2}{\mu_0}VC_{lmn}\right)^2 Q_L Q_a \tag{4.9}$$

Figure 4.17 shows CAST-CAPP detector's capability to probe axion-photon coupling with respect to KSVZ model (y axis) given the data acquisition time (x axis), scanning bandwidth (line colors) and number of phase-matched cavities (dashed and

solid lines for minimum - single - and maximum - 4 - values, respectively). Current operational parameters of CAST-CAPP are best represented by black curves (500 MHz data acquisition range) around $t \sim 10^2$ days.

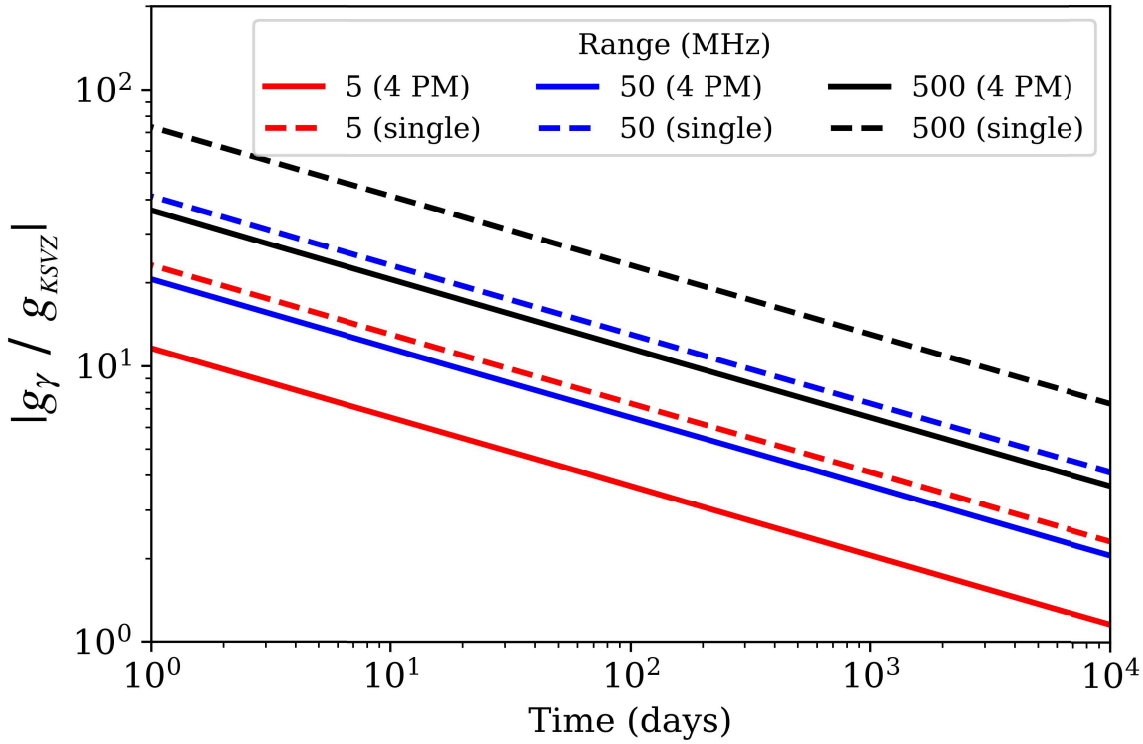

Figure 4.17. Axion-photon coupling exclusion prospects as a function of time, given the frequency tuning range (data acquisition range) with colors: Red (5 MHz), blue (50 MHz), black (500 MHz). Solid lines denote the case for 4 phase-matched cavities whereas dashed lines mark the single cavity case.

Figure 4.18 displays the time required to reach a sensitivity target of KSVZ or DFSZ theoretical values or their multiples, given the data acquisition bandwidth (x axis) for the best case where we use 4 phase-matched cavities. Unfortunately, reaching the parameter space around KSVZ and DFSZ theoretical bands (red and black solid lines, respectively) is not probable considering the reasonable short- and medium-term plans with data-taking time $t < 10^3$ day with the given experimental setup. We discuss how we can change this scenario through several hardware updates in Section 4.8. With the current capabilities of CAST-CAPP, we are focused on the parameter space around KSVZ (DFSZ) x10 given by red and black dashed lines.

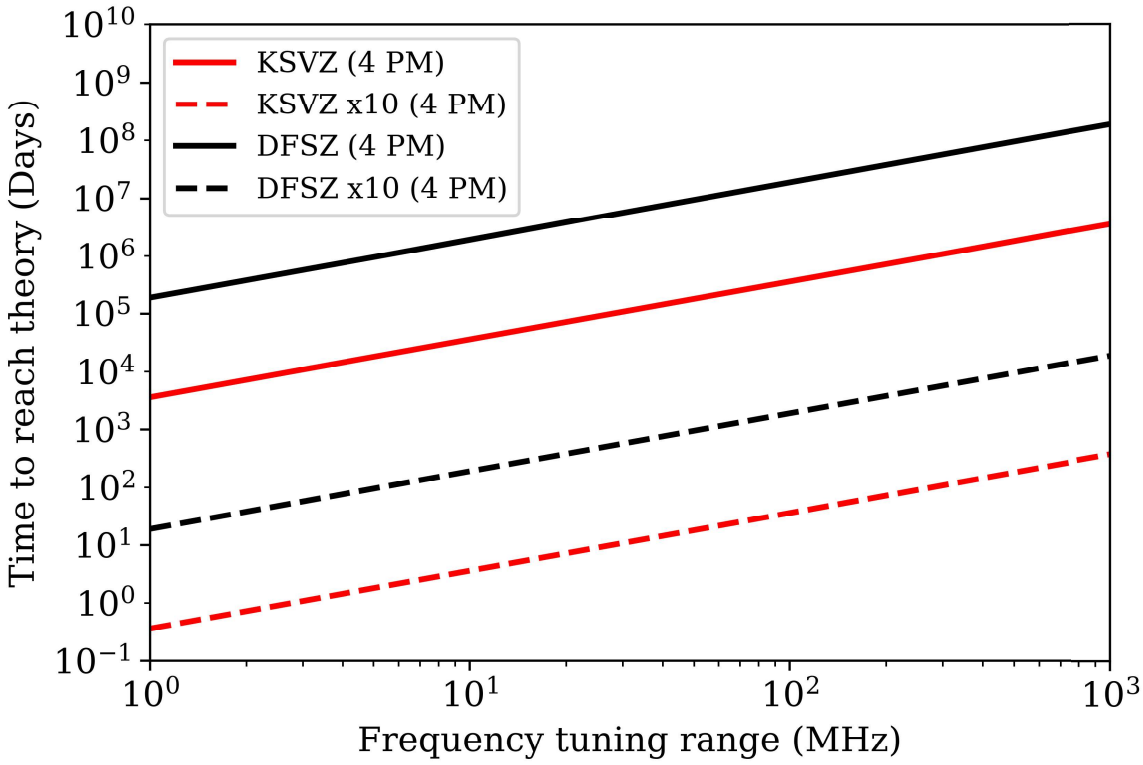

Figure 4.18. Time to reach KSVZ (solid, red) and DFSZ (solid, black) axion coupling sensitivity as a function of tuning range. Dashed lines indicate KSVZ & DFSZ axion coupling x10 with colors red & black, respectively.

4.8. Future of CAST-CAPP

In short-term (6 months), CAST-CAPP will continue scanning 4.8-5.4 GHz range with 4 cavities by fast scanning method looking for both halo and transient axions. Figure 4.19 shows the parameters space we aim to explore in the first half of 2021 with single cavity (region bounded by red line) and 3 phase-matched cavities (region bounded by blue line). We will also keep scrutinizing the outlier signals we have detected so far using measurements with cavities (magnet on/off) and external antenna. We will also keep improving our analysis methods and apply them for the new data as well as the existing dataset of total size > 500 TB. We do not plan to extract cavities from the CAST magnet in short-term.

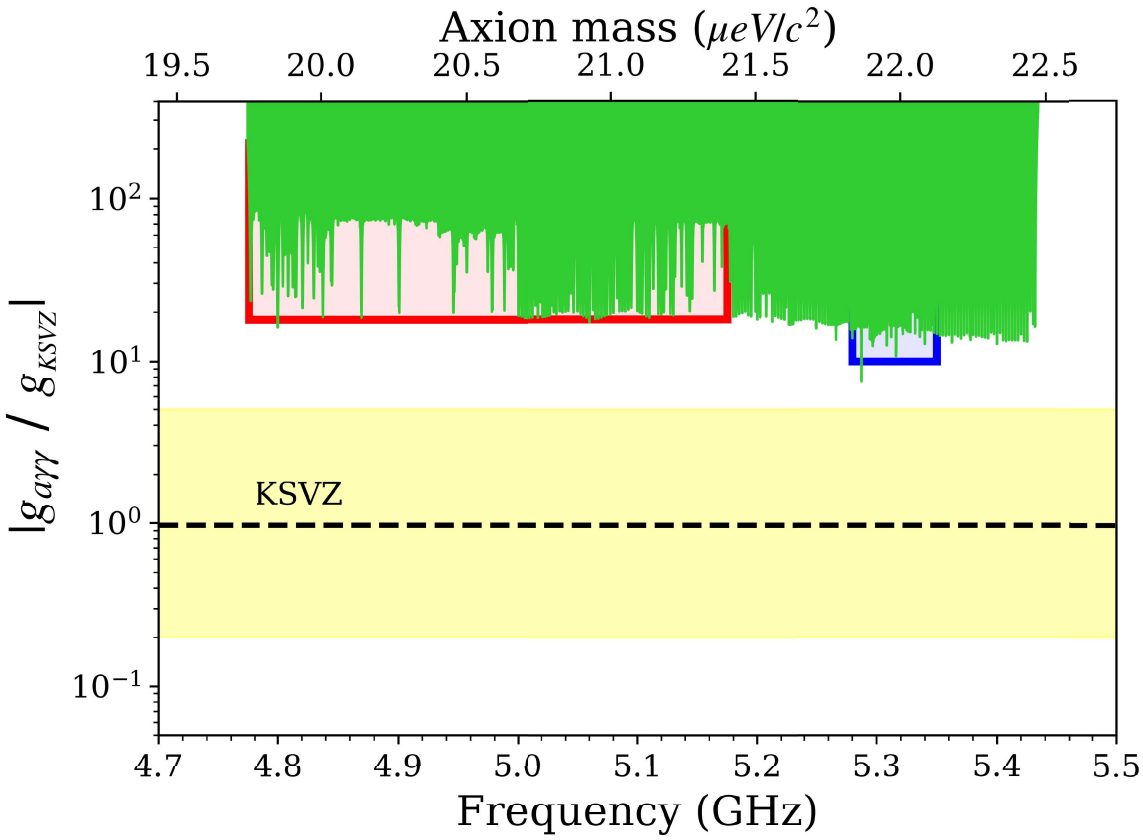

Figure 4.19. CAST-CAPP axion parameter space scanning prospects in short-term. The region bounded by red line is to be scanned by a single cavity and the one with blue line boundary is to be scanned by 3 phase-matched cavities.

In long-term, we plan to do several hardware improvements which will also require the extraction of cavities from the CAST magnet:

- Upgrade of the tuning systems including piezo motors inside our cavities to have a wider tuning range for all cavities as well as a smoother tuning capability. This change will increase the overall frequency range to $\sim$ 1 GHz and make it possible to scan a wider range with phase-matched cavities.
- Improvement of the thermal contact of each cavity with CAST magnet to reduce cavity temperatures. CAST-CAPP temperature sensors read $\sim$7 K, while CAST cryostat operates at 2 K. There are 2 reasons for this increased temperature: First is the amplifiers on each cavity which have $\sim$ 1.5 mW (optimized) power dissipation. Second is the heat dissipation of piezoelectric tuner motors. A better

thermal contact should bring cavity temperatures closer to 2 K.

- Superconducting coating to the inner surfaces of our cavities to boost the cavity quality factor up to $\sim 10^6$. Ongoing R&D work in IBS/CAPP (at South Korea) where high temperature superconductor (HTS) cavities using $YBa_2Cu_3O_{7-x}$ tape on their inner surface keep their superconducting phase even at 8 T (the highest B-field available during the test). The development of the superconducting cavity, by attaching HTS tape on the cavity inner surface, will take at least half a year before it can be implemented. [39]
- Integration of Hall probes near cavities in CAST magnet.

5. DATA PROCESSING AND ANALYSIS

5.1. From Time Domain to Frequency Domain: Fourier Transform

A function $f(x)$ that is continuous in an interval can be expressed as a superposition of a set of orthogonal functions that is complete in that interval. Fourier series utilizes an infinite sum of sine and cosine functions which form a complete orthogonal set in interval $[-\pi, \pi]$. Fourier series of a function f(x) which is periodic in interval $[-L/2, L/2]$ of length L is written as in Equation 5.1 whereas Equation 5.2 is the complex representation of the same Fourier series based on the Euler's formula $e^{ix} = cos(x) + isin(x)$. [40]

We want to decompose our time domain data to its constituent harmonics using Fourier formalism. To this end, in Equation 5.3, we rewrite Equation 5.2 by transforming the interval $[-L/2, L/2] \rightarrow [-\tau/2, \tau/2]$ where τ is the time length of data, $x \rightarrow t$ and $2\pi k/L \rightarrow 2\pi k/\tau \rightarrow \omega_k$. Equation 5.4 gives the amplitude of each frequency component as a function of frequency.

$$f(x) = \frac{a_0}{2} + \sum_{k=1}^{\infty} a_k cos\left(\frac{2\pi kx}{L}\right) + \sum_{k=1}^{\infty} b_k sin\left(\frac{2\pi kx}{L}\right) \tag{5.1}$$

$$f(x) = \sum_{k=-\infty}^{\infty} c_k exp\left(i\frac{2\pi kx}{L}\right) \tag{5.2}$$

$$f(t) = \sum_{k=-\infty}^{\infty} A(\omega_k) e^{i\omega_k t} \tag{5.3}$$

$$A(\omega_k) = \frac{1}{\tau}\int_{-\tau/2}^{\tau/2} f(t) e^{-i\omega_k t} dt \tag{5.4}$$

In the discussion above, we assumed we have a continuous time domain data $f(t)$. However, in reality, our data consists of a set of discrete samples of the underlying continuous function where we take samples with equal time intervals Δt with sampling rate $(\Delta t)^{-1}$. And our aim is to reconstruct that continuous function as good as can

be in both time and frequency domains using the finite samples at hand. Therefore, we have $f(t) \rightarrow f(t_n) \equiv f_n$ and $n = 0, 1, ..., N-1$ where N is the number of samples in our data. Frequency amplitudes $A(\omega_k) \equiv A_k$ have the index $k = 0, 1, ..., N-1$ to denote frequency components resulting from Discrete Fourier Transform (DFT). In this case, Equations 5.3 and 5.4 are transformed into Equations 5.5 and 5.6 which represent inverse DFT and DFT, respectively. As the equation indicate, having N samples limits the number of frequencies to N and for the discrete case Equation 5.6 is no longer an integral.

$$f_n = \frac{1}{N} \sum_{k=0}^{N-1} A_k e^{i2\pi kn/N} \tag{5.5}$$

$$A_k = \sum_{n=0}^{N-1} f_n e^{-i2\pi kn/N} \tag{5.6}$$

5.2. Sampling Theorem

Sampling theorem states that using samples $f(t_n)$, we can fully retrieve the underlying continuous $f(t)$ if all of its Fourier series components have frequencies $\omega_k/2\pi = k/\tau = k/N\Delta t$ in interval $[-\nu_c, \nu_c]$ where Nyquist critical frequency, ν_c, is half of the sampling rate $(\Delta t)^{-1}$ as given by Equation 5.7. That is, to monitor a given bandwidth $\Delta\nu$, we need $(\Delta t)^{-1} = \Delta\nu$ samples per second. As indicated by Nyquist interval DFT results in negative and positive frequencies. The diagram in Figure 5.1 manifests the correspondence between index k and frequencies ν where the 0 Hz component ($k = 0$) indicates DC offset of time series and $k = N/2$ implies Nyquist frequency $\nu = \pm\nu_c$. [41]

$$\nu_c = \frac{1}{2\Delta t} \tag{5.7}$$

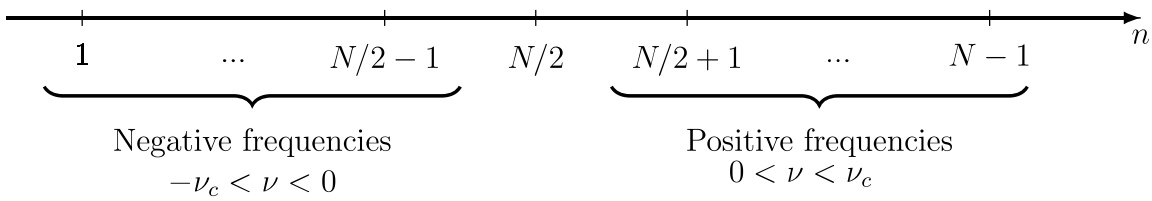

Figure 5.1. A diagram of DFT output frequencies.

In case $f(t)$ has some frequency components that exceed Nyquist critical frequency ($|\omega_k/2\pi| > \nu_c$) power spectrum of $f(t)$ will be distorted due to aliasing effect. In order to refrain from disruptive effect of aliasing one should confine DFT input $f(t)$ to a frequency bandwidth in the Nyquist interval $[-\nu_c, \nu_c]$. This can be done by filtering $f(t)$ to a narrower band or by increasing the sampling rate to broaden the Nyquist interval.

An intuitive way to understand (inverse) DFT is to examine it as a matrix transformation between 2 vectors $f_n \leftrightarrow A_k$. Equation 5.8 shows DFT as a matrix transformation, equivalent of Equation 5.6 where $w = e^{-i2\pi/N}$ is the Nth root of unity. Execution of this $N \times N$ matrix equation requires N^2 operations (multiplication followed by a summation) and computation time by a computer scales with $O(N^2)$. Algorithms that calculate DFT considerably faster than $O(N^2)$ are called Fast Fourier Transform (FFT). For data processing, we use Cooley–Tukey FFT algorithm which computes the Equation 5.8 with with $O(Nlog_2N)$ operations, scaling the computation time from days to hours. (see Appendix B)

$$\begin{pmatrix} A_0 \\ A_1 \\ A_2 \\ \vdots \\ A_{N-1} \end{pmatrix} = \begin{pmatrix} 1 & 1 & 1 & \cdots & 1 \\ 1 & w & w^2 & \cdots & w^{N-1} \\ 1 & w^2 & w^4 & \cdots & w^{2(N-1)} \\ \vdots & \vdots & \vdots & \ddots & \vdots \\ 1 & w^{N-1} & w^{2(N-1)} & \cdots & w^{(N-1)^2} \end{pmatrix} \begin{pmatrix} f_0 \\ f_1 \\ f_2 \\ \vdots \\ f_{N-1} \end{pmatrix} \tag{5.8}$$

5.3. Zeroth Frequency and Data Detrending

In every FFT spectrum we observe a peak that is exactly at the center (0 Hz) which is caused by the DC offset in the time domain data as mentioned in Section 5.2. Although it is absent in the diagram of Figure 5.1, DFT (or equivalently FFT) output involves 0th frequency component which is equal to the DC offset of time-domain data. A possible solution to get rid of this artificial peak is to detrend the data before applying FFT in order to make DC offset naught. Detrending means to fit a line to the data and subtract it from the data. After detrending, 0 Hz bin in the FFT spectrum becomes zero. However, there are 2 disadvantages of detrending:

- Amplitudes of several bins around the central bin (0 Hz) are also affected by this operation and their amplitudes are reduced.
- Total processing time is more than doubled with detrending.

We verified that detrending does not affect the data distribution in the following steps of analysis. In, conclusion, we decided not to detrend data before FFT. Instead, we will discard 0 Hz bin from the analysis procedure.

5.4. Data Processing and Noise Characteristics

Raw data structure of CAST-CAPP was mentioned in Section 4.4. After the raw data is offloaded from RAID system to the local drive and uploaded from the local drive to CASTOR, the next step is data processing. A custom-made Python program is used to process raw data. Main function of processing is to convert I/Q type time series binary data to human readable arrays of power spectrum by applying Fast Fourier Transform (FFT).

First, I/Q samples are converted to voltage values by multiplying them with a scale factor that is recorded in the header file specific to each measurement. Thus we obtain complex samples $z(t) = I(t) + iQ(t)$ where $i = \sqrt{-1}$. Then, we convert time

domain data to frequency domain using FFT algorithm obtaining $z(f)$. We can use I/Q or equivalently z to calculate the root mean square (RMS) voltage as given by Equation 5.9. We can compute RMS power from V_{RMS} considering a circuit with 50 Ω load in units of Watt (see Figure 5.10) and dBm (see Figure 5.11).

$$V_{RMS} = \sqrt{\frac{I^2 + Q^2}{2}} = \sqrt{\frac{z^* z}{2}} \tag{5.9}$$

$$P_{RMS} = \frac{V_{RMS}^2}{R} = \frac{I^2 + Q^2}{2R} = \frac{z^* z}{100} \tag{5.10}$$

$$P(dBm) = 10 \times log_{10} \left(\frac{P_{RMS}(\text{Watt})}{1mW} \right) \tag{5.11}$$

Complex z samples and underlying complex counterparts $I(f)$ and $Q(f)$ have Gaussian distribution. This results in χ and χ^2 distributions of 2 degrees of freedom for FFT voltage and power outputs, respectively. Equations 5.12 and 5.13 show the probability density functions (PDFs) of χ and χ^2 distributions.

$$PDF\left(\chi^2, r\right) = \frac{1}{2^{(r/2)-1}\Gamma(r/2)}\ x^{r-1} e^{-x^2/2} \tag{5.12}$$

$$PDF\left(\chi, r\right) = \frac{1}{2^{r/2}\Gamma(r/2)}\ x^{r/2-1} e^{-x/2} \tag{5.13}$$

where r specifies the degrees of freedom, Γ is the gamma function and $x \in [0, \infty)$. Figure 5.2 shows the normalized histograms of voltage and power spectra resulting from FFT.

Before applying FFT, we divide our dataset into k chunks of length N such that each datafile consists of kN samples. N is determined to ensure the desired value of the resolution bandwidth of the processed spectra, $\delta\nu_P$. Time length of an FFT chunk ($\tau = \Delta t$ N = N / sampling rate) determines the minimum sine wave frequency we can fit into it through FFT; therefore it determines the resolution bandwidth of the FFT spectrum. Equation 5.14 shows the inverse proportionality relation between the time length of an FFT chunk and the resulting resolution bandwidth of the FFT spectrum.

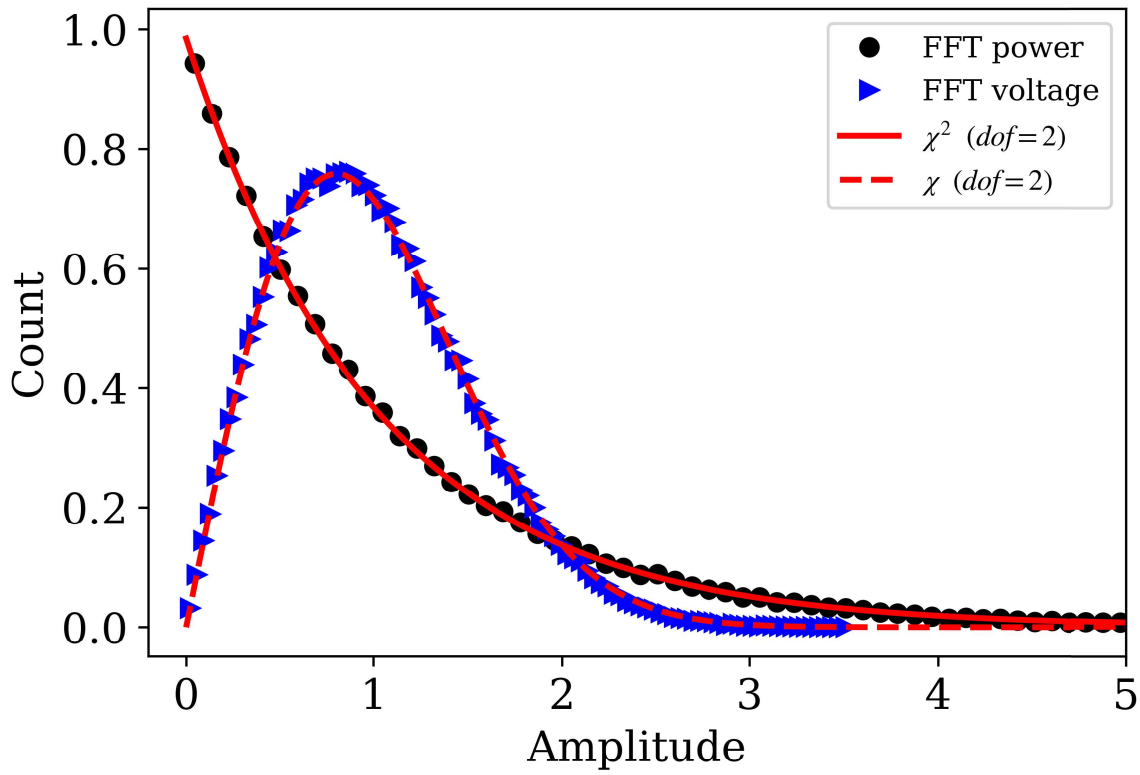

Figure 5.2. Normalized distribution of FFT voltage and power outputs. FFT power spectrum displays χ^2 distribution of 2 degrees of freedom. Because it is given by (Equation 5.10) the sum of squares of 2 normally distributed parameters. FFT voltage spectrum has χ distribution as it is proportional to the square root of the power spectrum as indicated by Equation 5.9. Baselines of both FFT power and voltage spectra were removed before histogramming and distribution functions were scaled.

$$\delta\nu_P = \frac{1}{\tau} \tag{5.14}$$

In order to obtain $\delta\nu_P = 50$ Hz, we set chunk time length to $\tau = 0.02s$ which in turn corresponds to select $N = 0.02s \cdot 6.25MS/s = 1.25 \times 10^5$ samples. Considering that CAST-CAPP records 1-minute datafiles of kN samples, the number of FFT chunks for each datafile is $k = 1$ minute / $\tau = 3000$. We average these FFT chunks to obtain an FFT spectrum. Figure 5.3 shows the FFT spectrum of a single chunk and the average of 3000 chunks. Although each FFT chunk has χ^2 distribution as indicated by

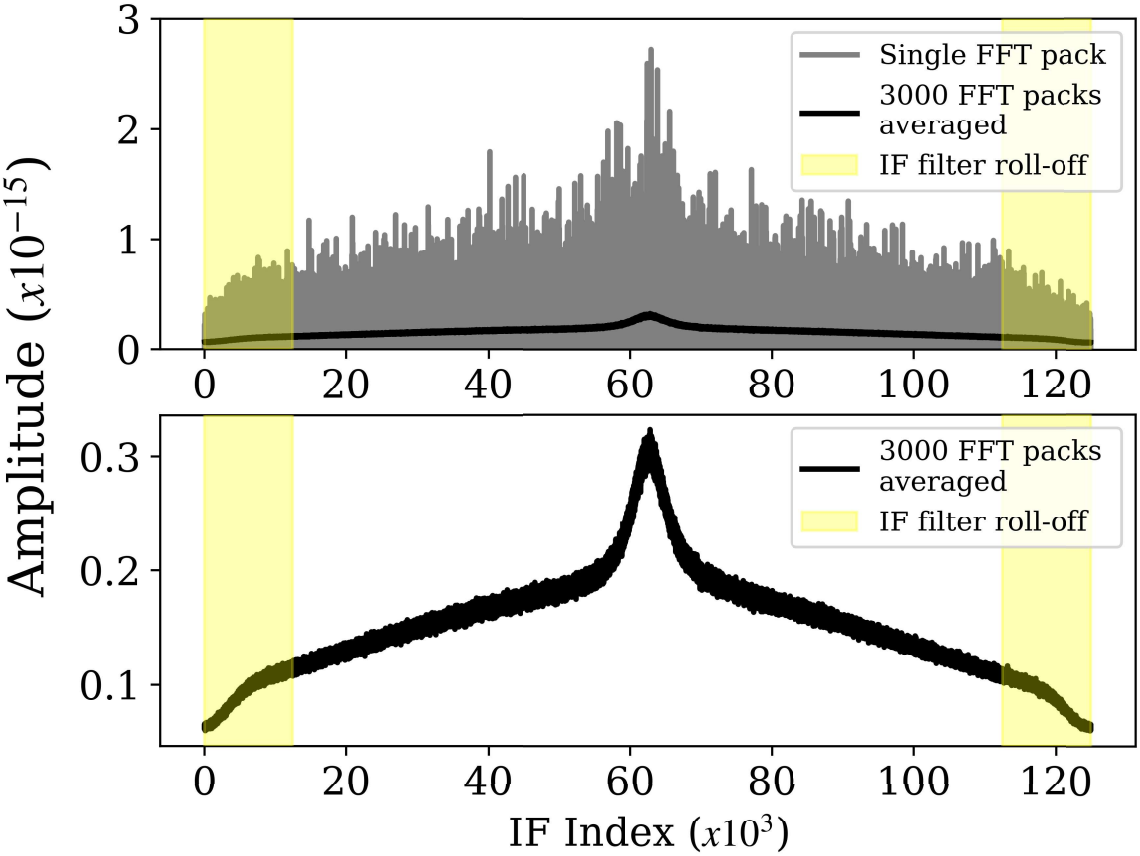

Figure 5.3. CAST-CAPP FFT spectrum of a single chunk (grey) of 0.02s data and 3000 packs averaged (black) of 1-minute data. Yellow band is the IF filter roll-off.

Figure 5.2, as we average $k = 3000$ spectra the distribution becomes χ^2 of $2k$ degrees of freedom which converges to normal distribution for $k >> 1$. Figure 5.4 shows the distribution of the averaged ($k = 3000$) FFT power spectra became Gaussian due to central limit theorem.

Power drop on the edges of the FFT power spectrum is due to spectrum analyzer's IF filter roll-off. These sections are indicated by yellow bands in Figure 5.3. In analysis, we crop these roll-off data which constitutes 20% of the whole from our spectra. Therefore, the number of samples in a spectrum becomes $N = 10^5$.

Random fluctuations of power of each bin in a spectrum is called noise. The baseline of power around which the random fluctuations occur, also called noise floor, is generally frequency dependent. That is, noise floor can have a shape defined by a

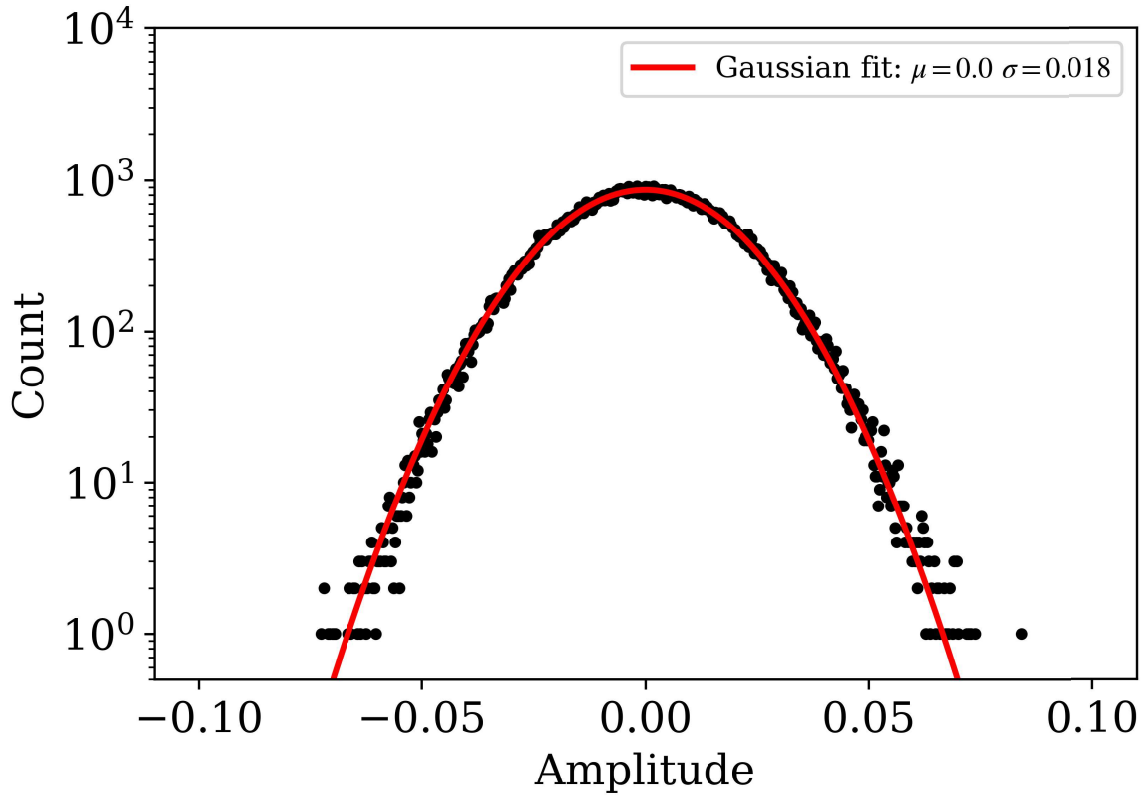

Figure 5.4. FFT spectrum of 1-minute data as an average of FFT power spectra of 3000 chunks. Baseline of the spectrum was removed before histogramming.

curve across the spectrum. Shape of the noise floor is redundant in the search for a signal in the spectrum and therefore removed using a digital filter (explained in Section 5.8). Remaining is Nyquist-Johnson (thermal) noise generated by thermal excitation of electrons in the conductor. Spectral density of thermal noise is constant throughout the spectrum for $f \lesssim 10$ THz, therefore it is also called white noise. The average noise power deposited in a bandwidth $\Delta\nu$ is given by Nyquist-Johnson noise formula (see Equation 5.15) as a function of bandwidth and noise temperature, T_S, in Kelvins where $N_0 = k_B T_S$ is the noise power density (Watt/Hz).

$$P_{noise} = k_B T_s \Delta\nu = N_0 \Delta\nu \tag{5.15}$$

We are also interested in the standard deviation of the noise power around P_{noise}. We repeat Equation 5.10,

$$P_{noise} = \frac{1}{M} \sum_{M} \frac{I^2 + Q^2}{2R} \tag{5.16}$$

where the sum is over M samples of measurements and both I and Q have are normally distributed as $N(0, \sigma)$. We can rewrite this equation without disturbing the variance of P_{noise} as

$$P_{noise} = \frac{1}{2M} \sum_{2M} \frac{A^2}{2R} \tag{5.17}$$

$$= \frac{1}{2R} \frac{1}{2M} \sum_{2M} (A - \mu_A)^2 = \frac{1}{2R} \sigma^2 \tag{5.18}$$

where A is also a sample from $N(0, \sigma)$ ($\mu_a = 0$) that we invented to work with instead of I and Q and we have $2M$ samples of A. Equation 5.18 is remarkably relates the mean noise to the variance I/Q samples. [42] $A = \sigma n$ where n is a sample of $N(0, 1)$. Applying error propagation to A^2, we see

$$A^2 = \sigma^2 n^2 \quad \longrightarrow \quad \sigma^2_{A^2} = \sigma^4 \sigma^2_{n^2} = 2\sigma^4 \tag{5.19}$$

where n^2 is a sample from $\chi^2(r = 1)$ and therefore $\sigma^2_{n^2} = 2r = 2$. [43] Variance of P_{noise} is

$$\sigma^2_{P_{noise}} = \sigma^2_{noise} = \sum_{2M} \left(\frac{\partial P_{noise}}{\partial A^2} \right)^2 \sigma^2_{A^2} = \sum_{2M} \left(\frac{1}{2R} \frac{1}{2M} \right)^2 \; 2\sigma^4 = \frac{2}{2M} \left(\frac{\sigma^2}{2R} \right)^2 \tag{5.20}$$

Using Equation 5.18, we obtain

$$\sigma_{noise} = \sqrt{\frac{2}{2M}} \; P_{noise} \tag{5.21}$$

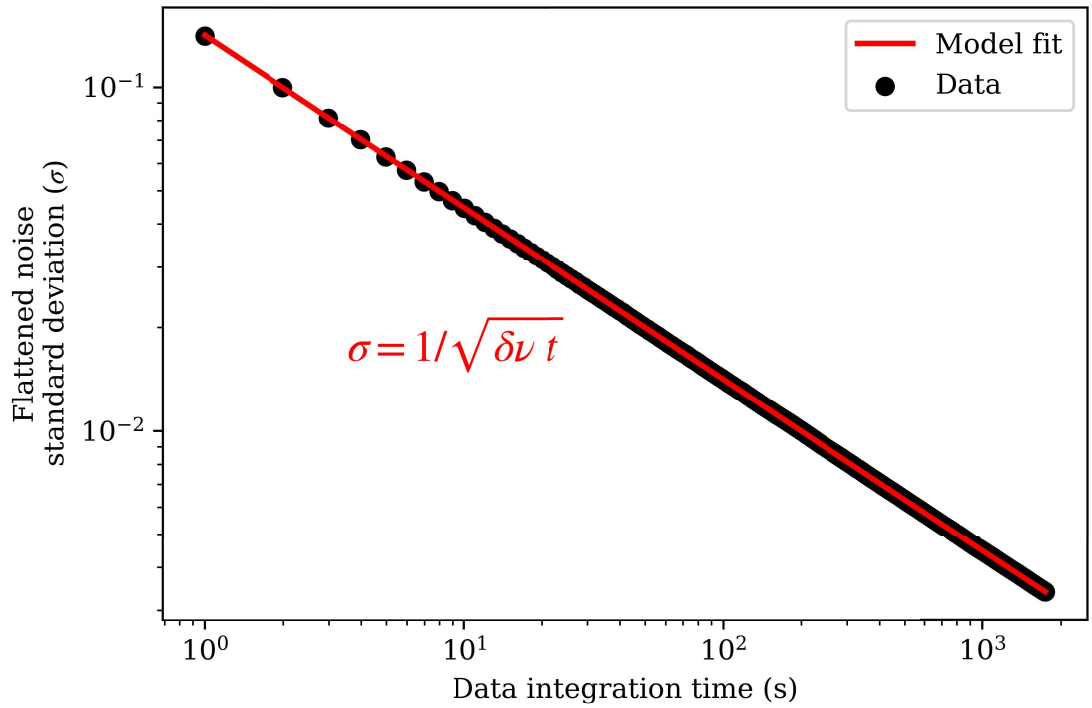

Figure 5.5. Standard deviation of flattened noise spectrum versus data taking time.

Noting $\nu_c = 1/2\Delta t = N/2t$ (Equation 5.7) where t is the total integration time and replacing the number of samples N with its counterpart $2M$, we get $2M = 2\tau\nu_c$. Bandwidth $\Delta\nu$ in our spectra is equal to Nyquist critical frequency ν_c, so we can write $2M = 2\tau\Delta\nu$ and we conclude on the standard deviation of noise

$$\sigma_{noise} = \frac{P_{noise}}{\sqrt{\Delta\nu\ t}} = \frac{k_B T_s \Delta\nu}{\sqrt{\Delta\nu\ t}} = k_B T_s \sqrt{\frac{\Delta\nu}{t}} \tag{5.22}$$

The standard deviation of each noisy bin of width $\delta\nu_P$ is $\sigma_{noise} = P_{noise}/\sqrt{\delta\nu_P\ t}$. However, doing the treatment of removing the noise baseline using a filter reduces the sigma to $\sigma = 1/\sqrt{\delta\nu_P\ t}$. For $\delta\nu_P = 50$Hz and $t = 60$s, we get $\sigma = 0.018$ which is exactly what we see in Figure 5.4. Figure 5.5 shows the standard deviation of the flattened power spectra as a function of the integration time.

Signal-to-noise ratio (SNR) for the thermal noise and a signal of power P_S is given by Dicke Radiometer equation. [44]

$$\mathrm{SNR} = \frac{P_S}{\sigma_{noise}} = \frac{P_S}{k_B T_S}\sqrt{\frac{t}{\Delta\nu}} \tag{5.23}$$

where, t is the integration time. In order to calculate the SNR of an axion signal we do the conversion $\Delta\nu \longrightarrow \Delta\nu_a \approx 5$ kHz.

5.5. Analysis Overview

We follow mainly the procedure developed by HAYSTAC [30], ADMX [45] and IBS/CAPP [46] experiments. Still, we make several small-scale modifications on the procedure in order to increase its compatibility to our data. Brief outline of the analysis procedure is as follows:

- Start by taking data qualification steps, we qualify each of our datafiles for the analysis procedure by checking the file specific auxiliary parameters obtained by the spectrum analyzer, VNA and temperature sensors.
- Scan our spectra for intermediate frequency (IF) interference, meaning parasitic lines that appear on the same integer index of our spectra independent of the RF frequency of the measurements.
- Use a digital low pass filter to remove the noise baselines of our processed spectra.
- Scale each flattened spectrum and combine them with vertical weighted averaging using the RF index to obtain the combined spectrum.
- Generate the grand spectrum by horizontal averaging in order to maximize SNR of a KSVZ axion that can occur in the spectrum.
- Set a threshold and accept the grand spectrum bins that exceed the threshold as rescan candidates.
- Scrutinize each candidate in order to verify a possible discovery.
- If none of the candidates survive exclude the corresponding axion-photon coupling parameter space.

Table 5.1 shows the number of spectrum bins and resolution bandwidth for all spectra we generate throughout the analysis procedure. Initials of the spectrum names are also used as superscripts to specify bin amplitude, mean standard deviation etc. of the samples from each spectrum. Scale column denotes the horizontal axis of each spectra we use in our plots and calculations where intermediate frequency (IF) is the unitless, integer bin index and RF is the radio frequency with Hz unit. Number of bins, N and the RF resolution bandwidths, $\delta\nu$ of each spectrum type is also listed. FFT and processed spectra are in fact identical, only the IF filter roll-off regions are cropped in the processed spectrum. So, we may use these names interchangeably.

Table 5.1. An account of the spectra we generate in the analysis procedure.

Spectrum name	**Superscript**	**Scale**	**N**	**Res. BW**
FFT	-	IF	1.25×10^5	50 Hz
Processed	P	IF	10^5	50 Hz
Flattened	F	IF	10^5	50 Hz
Scaled	S	IF	10^5	50 Hz
Combined	C	RF	13.2×10^6	50 Hz
Rebinned	R	RF	4.7×10^5	1.4 kHz
Grand	G	RF	4.7×10^5	1.4 kHz

5.6. Data Qualification

We impose several selection criteria on the datafiles and we discard the ones that do not fulfill those from the analysis procedure. These criteria aim to discriminate the data affected adversely by mechanical vibrations (that distort tuner positions causing a shift of tuner frequency, signal amplitude etc), temperature and magnetic field shifts. We rely on VNA cavity signal transmission measurements and temperature sensor readings to evaluate the quality of datafiles. We consider the following criteria.

(i) Center frequency of cavity should not shift more than 0.1 MHz during the measurement (see Equation 5.24). We measure the center frequency of the TE_{101}

resonance mode before and after every measurement with VNA and we expect the absolute value of the difference to be distinctly smaller that the cavity width, ν_0/Q, FWHM.

$$|\nu_{0,first} - \nu_{0,second}| < 10^5\text{Hz} \approx \frac{1}{5}\frac{\nu_0}{Q} \tag{5.24}$$

Center frequency is calculated by averaging the 2 points at which cavity resonance peak on VNA screen intersects the horizontal line at half amplitude (3 dB) of the resonance peak. This reading is equivalent to the position of the signal maximum if the cavity resonance peak is symmetric. However, in both cases the first method that we use is more reliable when cavity signal noise and the mechanical vibrations are considered.

(ii) Quality factor, Q, of cavity transmission signal should be in the limits 10^3 - 4×10^4. These limits are determined considering the observed values of quality factors of 4 CAST-CAPP cavities. The most probable Q values are within the range 10^4 - 2×10^4.

(iii) Quality factor shift during a measurement should not exceed 7×10^3 during the measurement. This limit is determined by an examination of observed values which concludes that Q shift values above 7×10^3 are very rare.

(iv) Cavity resonance amplitude shift during the measurement should not exceed 3 dB. A shift of the resonance amplitude can stem from several origins such as a mechanical vibration induced shift of the resonance frequency, amplifier gain fluctuations.

(v) Cavity temperature shift during a measurement should not exceed 3 K. Temperatures of each cavity are measured before and after data-taking. Observed temperature shifts are mostly below 1 K and not even a single data file is discarded due to this criterion, up to now.

(vi) We do not impose a limit on the cavity temperatures in CAST-CAPP as the data with higher temperatures does not interfere with the analysis quality and in the analysis procedure such data have lower weight in the analysis procedure. Just in case a temperature reading fails and returns an unreasonable value we make sure that cavity temperatures are in range 1 - 273 K.

Table 5.2. Statistics of datafiles discarded from the analysis of CAST-CAPP data due to not fulfilling the standards set for qualification. "Initial" and "Final" labels indicate the measurements before and after a measurement, respectively.

Reason of disqualification	**Number of affected datafiles**
Frequency shift during measurement	41
Amplitude shift during measurement	7
Quality factor (initial)	7
Quality factor (final)	11
Quality factor shift during measurement	1993
Frequency mismatch (initial)	25
Frequency mismatch (Final)	31
Amplitude mismatch (initial)	984
Amplitude mismatch (Final)	982
Total	3067

Next three qualifications concern the phase-matched measurements where we want to minimize the mismatch among the parameters that are discussed below.

(vii) Center frequency mismatch among phase-matched cavities should not exceed 20 kHz for the initial and 80 kHz for the final measurements. Previous studies show that we can apply phase-matching in CAST-CAPP successfully as long as the center frequency mismatch is smaller than $(\nu_0[GHz]/Q) \times 0.42$ GHz ≈ 100 kHz. [47] We tune the cavities to the same frequency before the measurement and the initial limit 20 kHz is set considering the intrinsic tuner vibrations in the order of 10 kHz. We do not actively track and correct center frequencies of cavities during the measurement, so we set a bigger limit 80 kHz for the end of the measurement.

(viii) Amplitude mismatch among phase-matched cavities should not exceed 1 dB for both initial and final measurements. Prior to the measurement we adjust the cavity resonance amplitudes to the same level using adjustable attenuators.

(ix) Temperature mismatch among phase-matched cavities should not exceed 3 K for both initial and final measurements. We impose this condition to eliminate a possible heterogeneous temperature distribution over phase-matched cavities.

Using the criteria above, we have discarded 3067 datafiles out of 126762 from the subsequent analysis procedure. Table 5.2 shows the number of files disqualified because of the standards we set. The reason for most of the disqualifications is the mechanical vibrations about CAST. Remarkably, we did not need to discard even a signal file due to temperature readings. This implies a good temperature stability in CAST magnet.

5.7. IF Interference Detection

Intermediate frequency (IF) interference is a single bin power excess that is originated mostly from the receiver electronics or numerical artifacts. Such a contamination occurs on the bin with the same index within all processed spectra, this makes it easier the filter out IF interference. Unlike RF interference which occurs on a fixed frequency instead of a fixed processed spectrum index imitating a prospective axion signal (see Section 5.14 for a discussion), an IF interference can by no means be mistaken for a candidate signal.

In order to search for IF interference, we split the whole dataset into 3 groups and take average of each group according to bin indexes (IF frequency). In order to flatten these 3 averaged spectra, we use median filter which is a digital filter that iterates over every bin in the spectrum and replaces them with the median value of the surrounding bins in a window. We set window length to 100, that is the window spans the 50 bins on both left and right side of each bin. The fact that median filter is blind to single bin spikes in the spectrum makes it useful for our purpose. We flatten each three averaged processed spectra by subtracting their median filters from them. Three flattened averaged spectra have approximately the Johnson-Nyquist (white) noise of Gaussian distribution. In each spectrum, we label the bins exceeding 5σ threshold. Considering that we have $N^P = 1.25 \times 10^5$ bins in processed (FFT) spectra, the

number of bins expected to exceed this threshold due purely statistical fluctuations is just 0.04. Labeled bins in each 3 groups are compared and the indexes that appear at least in 2 of 3 lists are flagged. Thus, we obtain a list of flagged bin indexes that will be removed from all processed spectra. Lastly, we flag also 2 more bin indexes that are on the left and the right side of each flagged bins.

On every processed spectrum, we remove the bins with indexes in the flagged bin list. We have in total 6 bins flagged as contaminated, originating from 2 detected IF interference. One of the two is due to FFT Zero-Hertz effect mentioned in Section 5.4. The other one results from receiver electronics. Since we take multiple measurements in close frequency ranges and CAST-CAPP cavities are tuned throughout the data-taking campaign the RF counterparts of flagged IF indexes keep changing and thus all bins in the combined spectrum have contributions from multiple processed spectra such that no spectrum bin in the final combined spectrum is empty due to IF interference removal.

5.8. Flattening Processed Spectra

Processed spectra have a baseline shape affected by the cavity resonance mode and the amplifier gain profile. In two steps, we flatten the processed spectrum by removing the noise baseline. First, we utilize Savitzky Golay (SG) filter to reproduce the baseline of the processed spectra. SG filter is a digital filter that is used widely for data smoothing. SG filter is composed of least-square fits of low order polynomials on sample window that moves by one bin at each step of evaluation. At each step, the center bin of the window is equated to the corresponding value of the polynomial fit. [48] Since the empty processed spectrum bins that are removed from spectra due to IF interference would distort SG filter, we replace such bins with the median filter counterparts of the processed spectrum temporarily to have a successful SG filter evaluation. Then, we apply SG filter of polynomial order $P = 4$ and window length $W = 1001$.

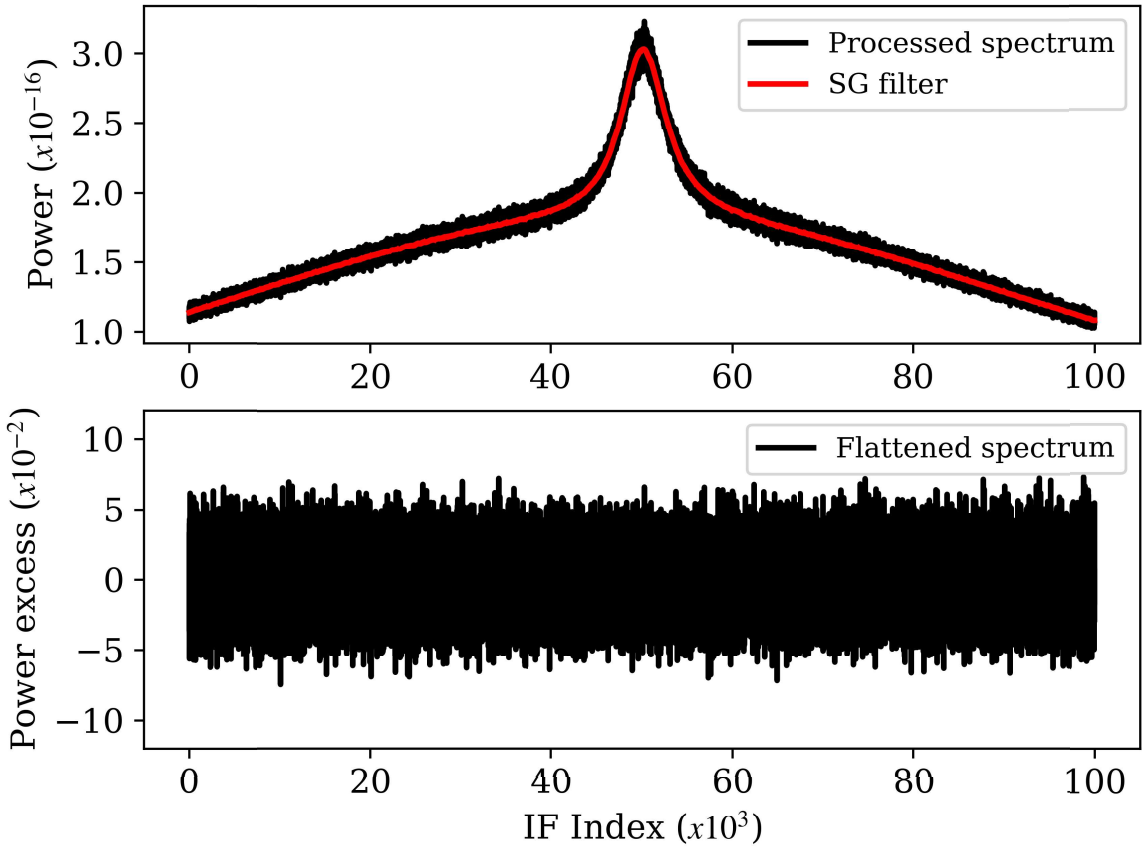

Figure 5.6. Processed spectrum 1-minute data as an average of FFT power spectra of 3000 chunks and the SG filter applied to it (upper). Processed spectrum noise baseline is removed to obtain the flattened spectrum (lower).

To obtain flattened spectrum, we divide the processed spectrum by its SG filter. And we crop the spectrum parts on both edges that are reflecting spectrum analyzer's IF filter roll-off which make up 20% of all samples. Thus, the flattened spectrum has $N^F = 10^5$ samples that have Gaussian distribution of mean $\mu^F = 1$ and standard deviation $\sigma^F = 1/\sqrt{\delta\nu^F\tau} = 1/\sqrt{50 \cdot 60} \sim 0.018$. Second, we subtract 1 from the flattened spectrum so that it has mean, $\mu = 0$. Figure 5.6 shows the processed spectrum, its SG filter and the flattened spectrum. Figure 5.4, in Section 5.4, shows the histogram of flattened spectrum bin amplitudes.

Figure 5.7 shows the transmission function of SG filter in spectrum bin domain with the parameters we use. 3 dB point of the filter with parameters $W = 1001$ and $d = 4$ sits at $\sim$ 15 dB. Therefore, SG filter is preferred due to its flat pass-band for

relatively big spectral shapes such as the noise bump and its relatively good stop-band performance for small scale spectral shapes such as an axion signal. As we do flattening by dividing each spectrum with its SG filter output, we observe the large scale spectral shapes are flattened completely and we foresee an axion signal will survive this process with a small scale attenuation which can be quantified by a simulation.

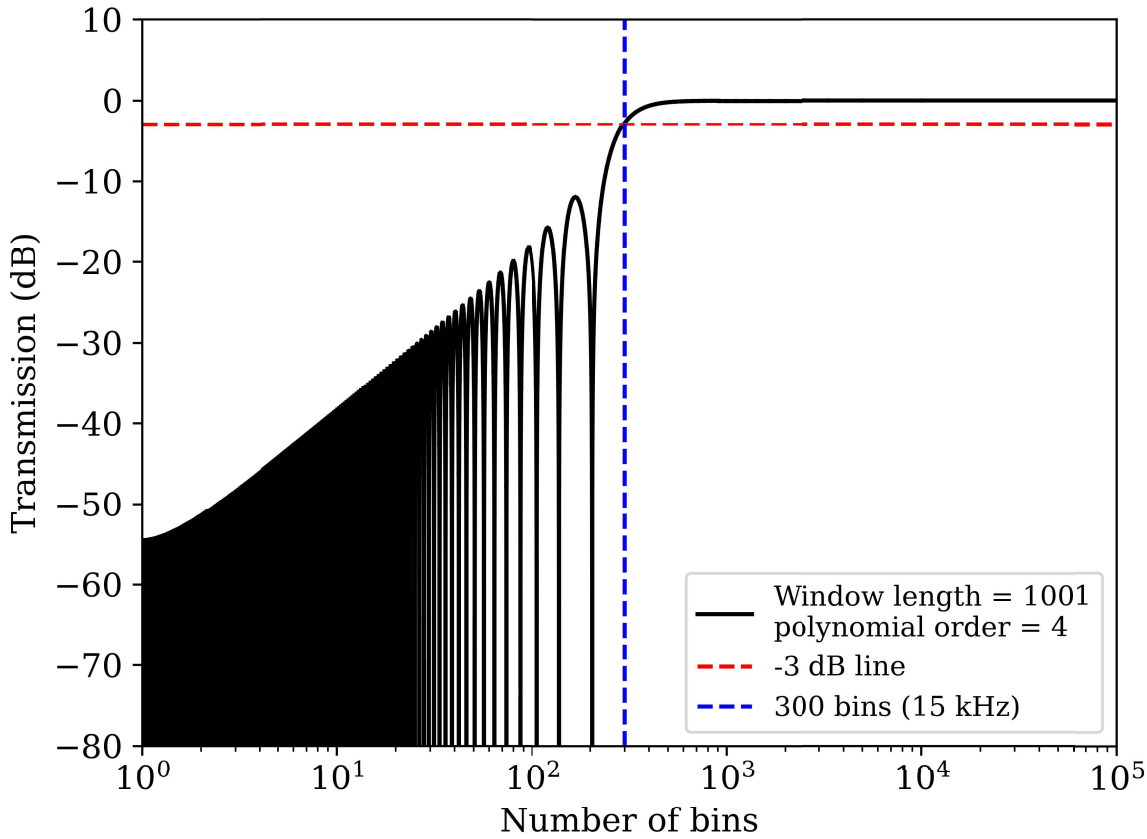

Figure 5.7. Transfer function of Savitzky-Golay filter with parameters: Window length = 1001, polynomial order = 4.

In conventional haloscope analysis, the averaged noise baseline is subtracted from the processed spectra prior to flattening with SG filter. This does not diminish a spectrum bin with axion signal because the averaged noise baseline is calculated according to IF frequency and the axion signal that has a constant RF value would occur on a wide IF range and therefore such an RF signal would smoothly spread on IF bins of averaged noise baseline. However, in our procedure, we calculate the daily combined spectra and then combine all daily combined spectra to obtain the combined spectrum. Therefore, we would need to subtract from each processed spectra the average noise

baseline the corresponding day. Doing this subtraction on a daily basis poses a high risk of axion signal attenuation. Because, on the days that we do not tune the cavity resonance frequency sufficiently, the RF location of axion would not be spread on a wide range on the IF scale of the averaged noise baseline and the averaged baseline itself may have an axion peak. In this case, subtracting the averaged baseline from each processed spectrum would remove the positive bins carrying axion power. As a result, we do not subtract the averaged baseline from processed spectra.

5.9. Combining Multiple Spectra

Until now, our discussion was based on noise characteristics of our spectra. We should now take into account how an axion signal would come out in our spectra. Axion signal power in a single CAST-CAPP cavity is given by Equation 5.25. The last two terms of this equation implies that axion detection power depends on the frequency ν and the frequency distance from cavity resonance mode $|\nu - \nu_0|$. That is, an axion signal amplitude changes across the flattened spectrum. The last term gives the axion power a Lorentzian profile as expected due to cavity resonance mode shape.

$$\begin{aligned} P_{Axion} = {} & 2.2 \times 10^{-24}\, W \\ & \times \left(\frac{\beta}{1+\beta}\right)\left(\frac{V}{0.224\, l}\right)\left(\frac{B}{9\, T}\right)^2\left(\frac{C_{nlm}}{0.53}\right)\left(\frac{g_\gamma}{0.97}\right)^2\left(\frac{\rho}{0.45\, GeV/cm^3}\right) \\ & \times \left(\frac{Q_{Axion}}{10^6}\right)\left(\frac{Q_{cavity}}{2\times 10^4}\right)\left(\frac{\nu}{5\ \mathrm{GHz}}\right)\left(\frac{1}{1+(2\, Q_{cavity}(\nu-\nu_0)/\nu_0)^2}\right) \end{aligned} \tag{5.25}$$

At every step of analysis, we will assume that all the axion power will be deposited in a single bin of the spectrum we work on. That is, we assume axion signal fits in a bin of $\delta\nu = 50$Hz for now. Before combining multiple spectra, we want to scale each flattened spectrum such that each bin p_i^F will have mean $\mu^F = 0$ except the one with axion signal which will have $\mu^F = 1$. Equations 5.26, 5.27 show the scaling relations for power and sigma values.

$$p_{ij}^{S} = \frac{k_B T_{s,j} \delta\nu}{P_{Axion,ij}} \; p_{ij}^{F} \tag{5.26}$$

$$\sigma_{ij}^{S} = \frac{k_B T_{s,j} \delta\nu}{P_{Axion,ij}} \; \sigma_{ij}^{F} \tag{5.27}$$

Unitless scaling factor P_{noise}/P_{Axion} is the ratio of Dicke's radiometer equation $P_{noise} = k_B T_{s,j} \delta\nu$ (see Section 5.4) to axion power. Subscript j denotes different spectra. Noise temperature $T_{s,j}$ varies across spectra and axion power $P_{Axion,ij}$ varies across spectra and across the bins in a spectrum. Denominator of the scaling factor ensures that an axion signal has mean $\mu = 1$ in any spectrum bin, whereas the numerator normalizes the noise power across different spectra and also guarantees the the scaling factor is unitless. Figure 5.8 shows the scaled spectrum in which each spectrum bin p_i^S is a sample drawn from normal distribution N(0, σ_i^S).

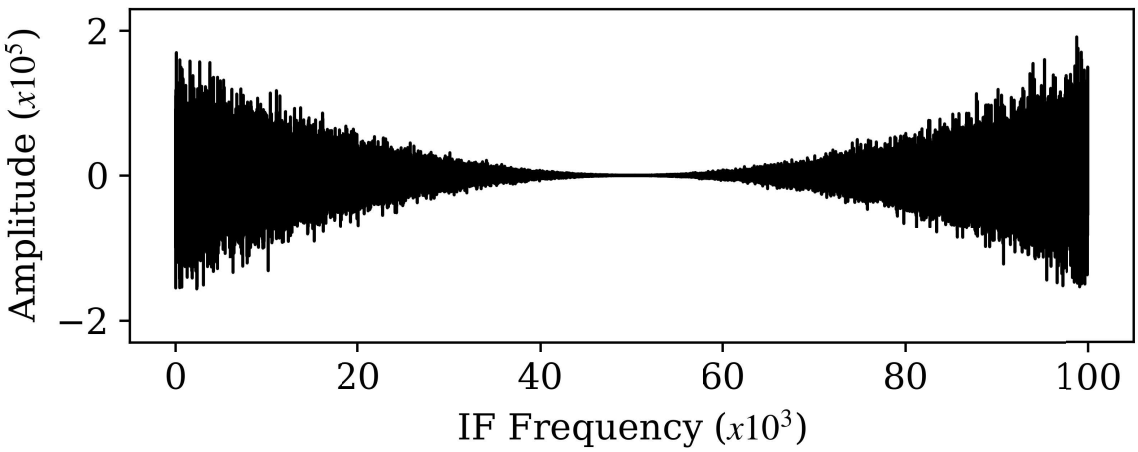

Figure 5.8. Scaled spectrum.

In order to generate the combined spectrum using a set of scaled spectra denoted by index j, we define a new index k which is the RF equivalent of IF index i in scaled spectra. Equation 5.28 shows the conversion between the IF and RF frequencies.

$$\nu = f_{RF} = \nu_0 - \Delta\nu/2 + \delta\nu \; f_{IF} \tag{5.28}$$

where ν_0 is the center frequency (and also the resonance frequency of the cavity), $\Delta\nu$ is the bandwidth (span) and $\delta\nu$ is the bandwidth resolution of the spectrum. f_{IF} is the unitless spectrum bin index and f_{RF} is the frequency with Hertz unit.

We define combined spectrum bins with their RF index k, instead of i. $p_{ij}^S = p_{kj}^S$ if i^{th} bin of the scaled spectrum corresponds to frequency k. We do weighted averaging of the scaled spectrum bins p_{ij}^S that correspond to k^{th} bin of the combined spectrum. That is, every combined spectrum bin p_k^C is composed of p_{kj}^S from m_k different scaled spectra with $j = 1, 2, ..., m_k$. This process is called vertical averaging (in RF domain). Figure 5.9 shows how we obtain the combined spectrum through the vertical averaging of 9 sample scaled spectra. Equation 5.29 show the weighted averaging that result in combined spectrum power p_k^C and Equation 5.30 gives the uncertainty propagation for grand spectrum sigma σ_k^C values. As provided by Maximum likelihood (ML) method, Equation 5.31 shows the weights are reciprocal of variances normalized by a sum. Using ML weights is the best option as it minimized standard deviation, maximizing signal-to-noise ratio (SNR).

$$p_k^C = \sum_{j=1}^{m_k} w_{kj}\ p_{kj}^S \tag{5.29}$$

$$\sigma_k^C = \sqrt{\sum_{j=1}^{m_k} w_{kj}^2\ (\sigma_{kj}^S)^2} \tag{5.30}$$

$$w_{kj} = \frac{(\sigma_{kj}^S)^{-2}}{\sum_{j=1}^{m_k} (\sigma_{kj}^S)^{-2}} \tag{5.31}$$

Since k index denotes RF center of a bin, $(k+1)-k = 50$ Hz, resolution bandwidth of the combined spectrum. RF centers of different scaled spectra may not align. In that case we shift the RF k values of all scaled spectrum by the smallest possible amount so that it aligns with k indices of the combined spectrum. Absolute value of this shifts is $\delta\nu/2 = 25$ Hz at maximum. That is, $-\delta\nu/2 \leq \nu_{shift} \leq \delta\nu/2$.

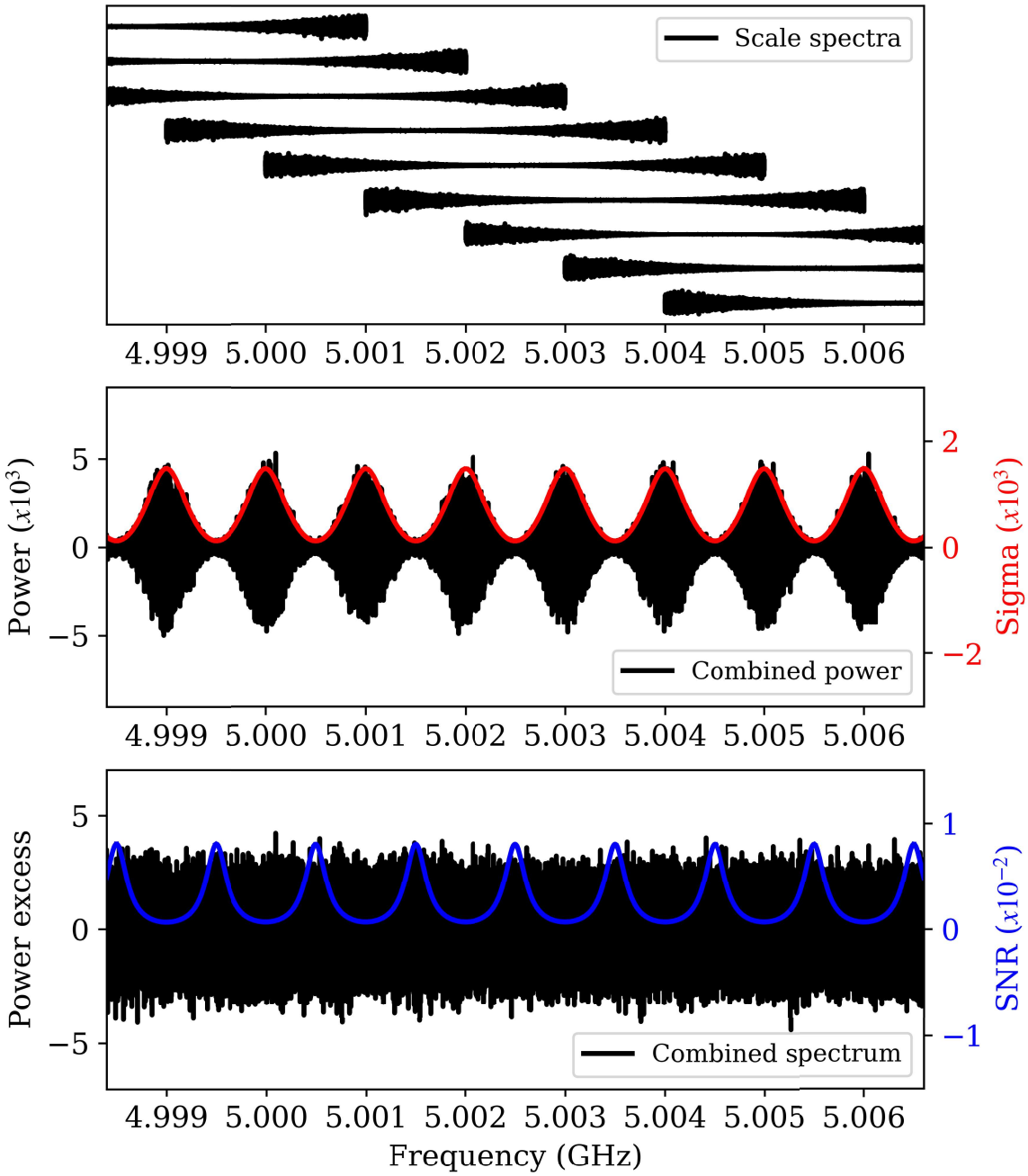

Figure 5.9. Vertical averaging of scaled spectra demonstrated on 9 sample scaled spectra. Scaled spectra are aligned according to RF index (top). Weighted averaging of the scaled spectra with maximum likelihood method (middle) where data in black and red represent p_k^C and σ_k^C. Lower plot shows the normalized combined spectrum where data in black and blue represent $x_k^C = p_k^C/\sigma_k^C$ and $(\sigma_k^C)^{-1}$.

Each combined spectrum bin p_k^C is a sample from Gaussian distribution of $\mu = 0$ and standard deviation σ_k^C. Only the bin that deposits axion signal power has $\mu = 1$ and standard deviation σ_k^C and SNR $(\sigma_k^C)^{-1}$. To have a standard sample distribution in the combined spectrum we normalize the spectrum $x_k^C = p_k^C/\sigma_k^C$. Combined spectrum of samples x_k^C have $\mu = 0$ and standard deviation $\sigma = 1$ except the bin that deposits axion signal power which has $\mu = (\sigma_k^C)^{-1}$, $\sigma = 1$ and SNR $= (\sigma_k^C)^{-1}$. Figure 5.10 shows the combined spectrum and its SNR for an axion signal.

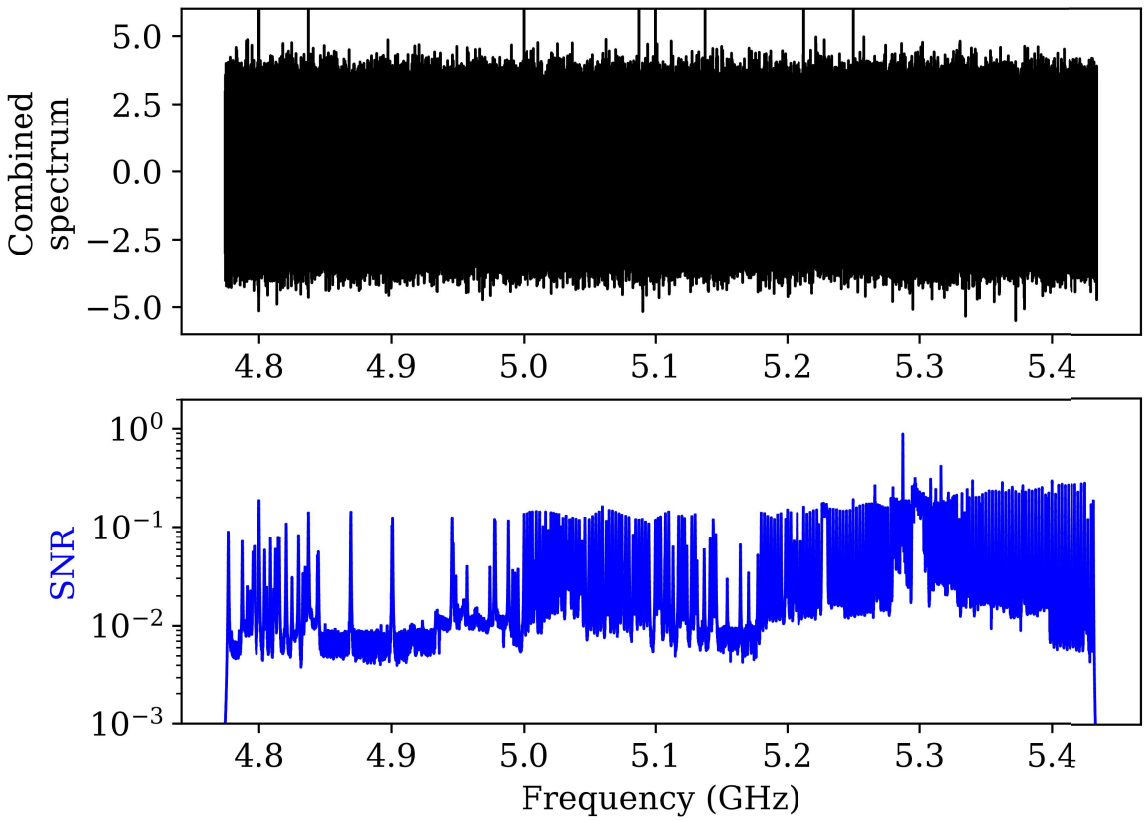

Figure 5.10. Combined spectrum (top black) and its SNR for a prospective axion signal (bottom blue).

There are 8 peaks in the combined spectrum that exceed 6σ which are hard to explain with statistical fluctuations only. We crop them from the plot for visual purposes. In Section 5.14, we examine the origins of such outlier signals.

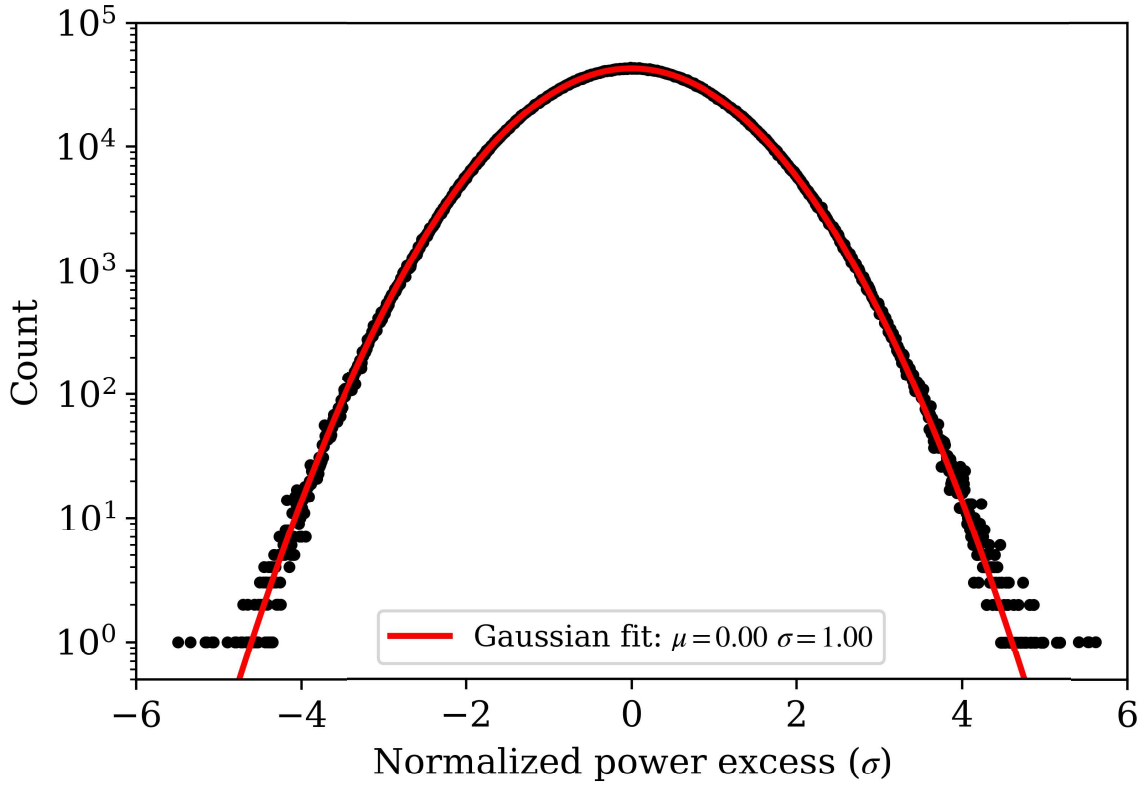

Figure 5.11. Combined spectrum histogram.

Figure 5.11 shows the histogram for the combined spectrum. As mentioned in Section 4.6.1, we calculate combined spectra daily to have fast feedback for possible transient signals. In order to obtain the "unified" combined spectrum out of all daily combined spectra, we use Equations 5.29 - 5.31 with p^S_{kj}, σ^S_{kj} replaced by p^C_{kj}, σ^C_{kj}.

5.10. Grand Spectrum

We want to maximize the SNR of a halo axion signal in the combined spectrum. This requires rebinning of the combined spectrum bins so that the bin width is comparable to the expected width of the axion signal. Following the discussion in Section 2.4, we expect $\sim 90\%$ of the axion signal curve to fit in a bin of width $\delta\nu_a = 7$ kHz. However, when scaling the flattened spectra (Equations 5.26, 5.27), we assumed that the whole axion conversion power is deposited in one bin of those spectra. Apparently, that assumption exaggerates the SNR of axion signal in the combined spectra. Thus, we begin with correcting this inaccuracy by multiplying both power and sigma values

of the combined spectrum by $K = 7\text{kHz}/50\text{Hz} = 140$. This leads to $p_k^C \to K p_k^C$ and $\sigma_k^C \to K\sigma_k^C$. Thus, normalized power excess $x_k^C = p_k^C/\sigma_k^C$ is unchanged and SNR is scaled as $(\sigma_k^C)^{-1} \to (\sigma_k^C)^{-1}/K$. After this scaling, a combined spectrum bin x_k^C that deposits $1/K$ of axion power is a sample of normal distribution with $\mu = (\sigma_k^C)^{-1}$ and $\sigma = 1$.

We rebin the combined spectrum in 2 steps. First, we take weighted average of $K_r = 28$ adjacent combined spectrum bins using ML weights. This process is called horizontal averaging. The product of this operation is the rebinned spectrum which has resolution bandwidth $\delta\nu^R = 1.4$ kHz. Therefore, the total number of bins N^C in the combined spectrum is reduced to $N^R \approx N^C/K_r$ in the rebinned spectrum.

The digital low-pass filter (SG) that we use to flatten spectra causes negative correlations among consecutive combined spectrum bins within a range smaller than that of the filter window. In Section 5.11, we quantify the elements of the correlation matrix via a simulation. Equations 5.32 and 5.34 give the power and standard deviation of rebinned spectrum bin as a weighted averaging of combined spectrum bins considering the elements of the correlation matrix.

$$p_r^R = \sum_{k=rK_r}^{(r+1)K_r-1} w_k \, p_k^C \tag{5.32}$$

$$w_k \approx \frac{(\sigma_k^C)^{-2}}{\sum_{k=rK_r}^{(r+1)K_r-1} (\sigma_k^C)^{-2}} \tag{5.33}$$

$$(\sigma_r^R)^2 = \sum_{k=rK_r}^{(r+1)K_r-1} \left(w_k^2 \, (\sigma_k^C)^2 + 2 \sum_{k'=rK_r}^{k-1} w_k w_{k'} \, \mathrm{COV}\left(p_k^C, p_{k'}^C\right) \right) \tag{5.34}$$

where we use RF index subscript r for the rebinned spectrum which is the counterpart of k in the combined spectrum, to prevent a confusion. Summations in Equations 5.32 and 5.34 are over combined spectrum windows of K_r bins. These Equation of horizontal averaging are equivalent to the Equations 5.29-5.31 of vertical averaging to

construct the combined spectrum. The difference (the second term in the summation of Equation 5.34) is due to the correlations of the neighboring bins in the combined spectrum because of SG filter. The approximate sign in Equation 5.33 implies a higher order deviation from the equality (negligible for our case) due to those correlations. The horizontal averaging of the combined spectrum results in the rebinned spectrum with bins $x_r^R = p_r^R/\sigma_r^R$ that are samples drawn from a normal distribution N(0,1), except the bins that deposit $1/K_g$ of axion power which are samples of N($(\sigma_r^R)^{-1}$,1).

In order to attain the grand spectrum, we apply a window function that has the shape of first $\Delta\nu_a = 7$ kHz of the axion power curve in lab frame (see Section 2.4) excluding its tail to the rebinned spectrum in windows of $K_g = 5$ bins. To find the weights for each bin, we integrate the axion lineshape within the boundaries of each bin. Equation 5.35 gives the integral for each bin for $q = 0, 1, ..., K_g - 1$, and even though f_{Lab} is normalized, there is K_g multiplier to ensure grand spectrum bins have $\mu = 1$. In each K_g-bin boxes we first normalize bins for the axion lineshape. That is, we divide p_r^R and σ_r^R with corresponding L_q. Equation 5.36 is the equivalent of Equation 5.32 for the grand spectrum as a summation over K_g bins that are normalized by L_q. Equation 5.38 depicts the standard deviation of bins corrected for the SG filter induced correlations.

$$L_q = K_g \int_{\nu_a + q\delta\nu_r}^{\nu_a + (q+1)\delta\nu_r} f_{Lab}(\nu) d\nu \tag{5.35}$$

$$p_g^G = \sum_{r=g,\ q=0}^{q=K_g-1} w_{r+q}\ p_{r+q}^R / L_q \tag{5.36}$$

$$w_{r+q} \approx \frac{(\sigma_{r+q}^R / L_q)^{-2}}{\sum_{q=0}^{K_g-1} (\sigma_{r+q}^R / L_q)^{-2}} \tag{5.37}$$

$$(\sigma_g^G)^2 = \sum_{r=g,\ q=0}^{q=K_g-1} \left(w_{r+q}^2\ (\sigma_{r+q}^R)^2 + 2 \sum_{q'=0}^{q-1} w_{r+q} w_{r+q'}\ \mathrm{COV}\left(p_{r+q}^R, p_{r+q'}^R\right) \right) \tag{5.38}$$

where the subscript g is the RF index that is the equivalent of r for the rebinned spectrum and k for the combined spectrum. Figure 5.12 depicts the grand spectrum (black) and its SNR (blue). Figure 5.13 shows the distribution of the grand spectrum.

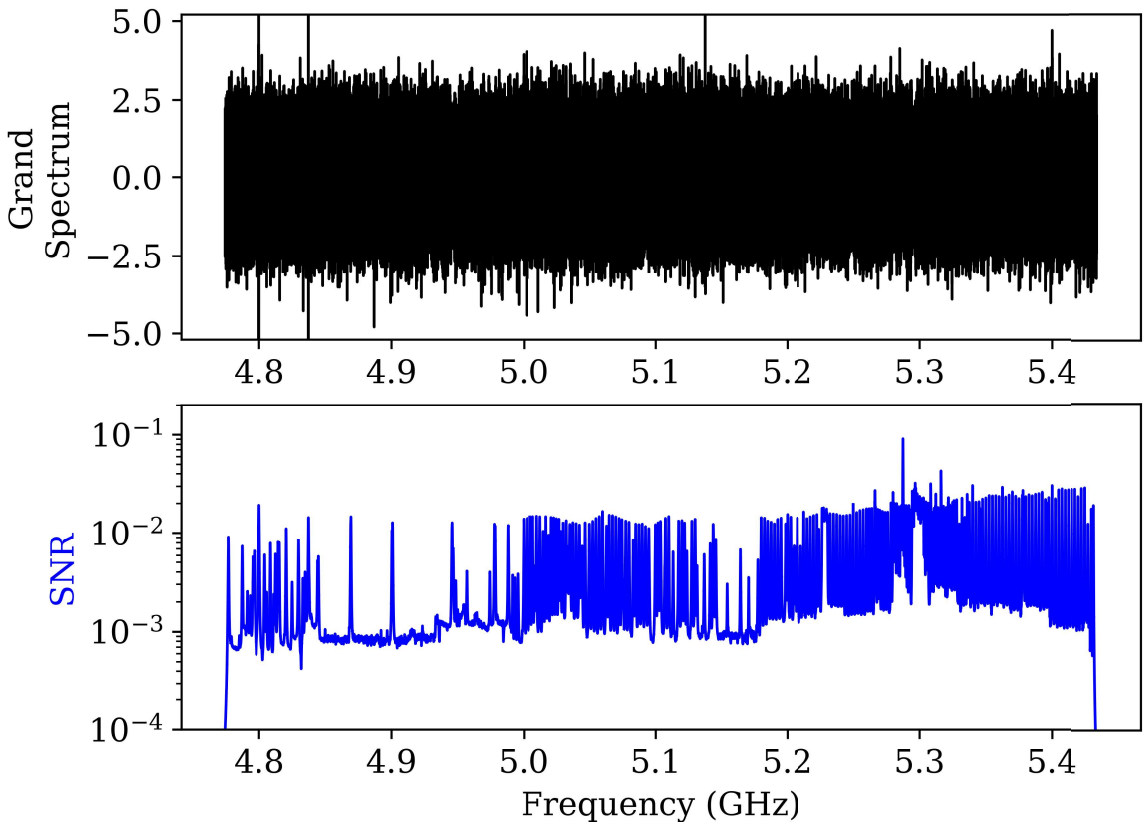

Figure 5.12. Grand spectrum (top, black) and its SNR for a prospective axion signal (bottom, blue).

5.11. A Simulation to Account for Grand Spectrum Correlations

We conducted a simulation to account for the reduction of standard deviation of grand spectrum data. This simulation confirmed that this reduction effect stems from the Savitzky-Golay (SG) filter used to flatten the processed spectra.

In each 10^4 iteration of the simulation, we followed the algorithm below.

(i) Create $n = 100$ Gaussian noise spectra of $N^P = 1.25 \times 10^5$ bins with $\mu = 1$ and $\sigma = (\Delta\nu^P \cdot \tau^P)^{-1/2} = 0.018$ using a random number generator.

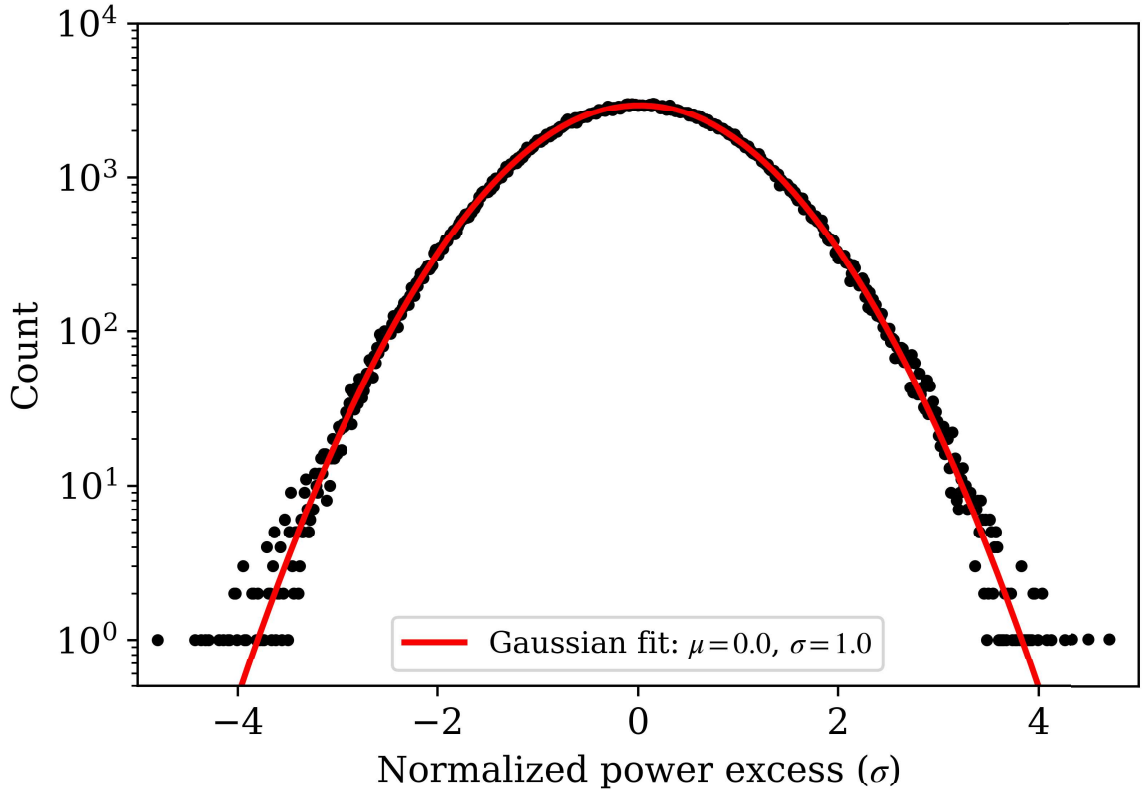

Figure 5.13. Grand spectrum histogram.

(ii) Multiply these spectra with random sample spectrum baselines derived from the experimental processed spectra to obtain the simulated processed spectra (SPS).

To create sample spectrum baselines, first, we average 50 processed spectra, second, remove contaminated bins and last, apply SG filter window size (in terms of bins), $W = 1001$ and polynomial order, $P = 4$. This filter serves as a sample spectrum baseline. We created 1000 such sample baselines for this simulation.

The next step is to obtain simulated flattened spectra (SFS) from SPS. We follow the steps below to this end.

(iii) Divide SPS by the average spectrum baseline.

(iv) Trim the symmetrical excess parts on both edges of SPS where amplifier profile distorts the data. The resulting spectra will have $N^F = 10^5$.

(v) Apply SG filter with $W = 1001$ and $P = 4$ to SPS.

(vi) Divide SPS by the resulting SG filter.

(vii) Subtract 1.

These steps give us n SFS per iteration. We continue processing SFS spectra as follows.

(viii) Average n SFS according to IF index without weighting to obtain the simulated combined spectrum (SCS) with $\mu = 0$, $\sigma = (\Delta\nu^P \cdot \tau^P \cdot n)^{-1/2}$.

(ix) Average horizontally every $N^R/N^C = 28$ bins to obtain the simulated rebinned spectrum (SRS) with $\delta\nu^R = 1.4$ kHz.

We simulated 10^4 SCS and SRS to compute the SG filter induced correlations among the adjacent bins of SCS and SRS separately using equations 5.39 - 5.41 where indices i and j denote iteration and IF index of both SCS and SRS. Equation 5.39 indicates that the covariance of any 2 bins of SCS or SRS depend only on the bin distancing Δj. Equation 5.40 can be simplified to 5.41 as the expected value of any bin of both SCS and SRS is $\mu = 0$.

$$COV(x_j, x_{j+\Delta j}) = COV(\Delta j) \tag{5.39}$$

$$= \langle (x_{i,j} - \langle x_{i,j} \rangle_i)(x_{i,j+\Delta j} - \langle x_{i,j+\Delta j} \rangle_i) \rangle_i \tag{5.40}$$

$$\approx \langle x_{i,j} \;\; x_{i,j+\Delta j} \rangle_i \tag{5.41}$$

We tested the simulation to verify the null hypothesis by excluding the spectrum flattening with SG filter from the procedure, therefore, bypassing steps (ii)-(vii) of the procedure above and creating SFS directly from step (i). In this case we observed no correlations among SCS or SRS bins.

Simulation results shows that the variation of the covariance of SCS bins for $\Delta j < 28$ is negligible. Figure 5.14 displays the variation of covariance is SCS for $0 < \Delta j < 28$.

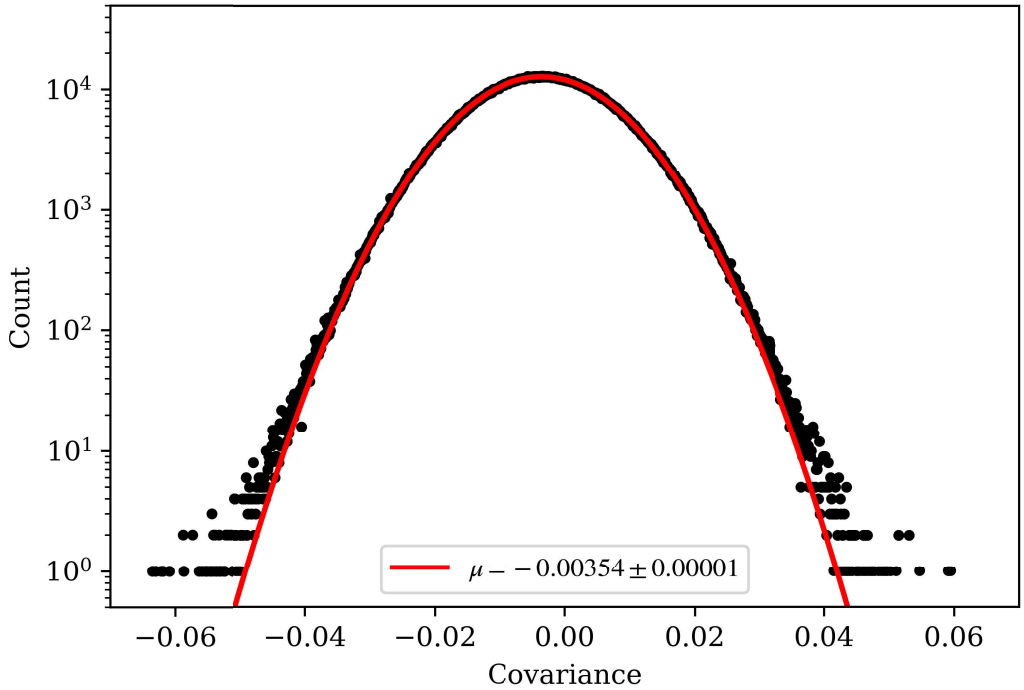

Figure 5.14. Covariance distribution among SCS bins with bin spacing < 28.

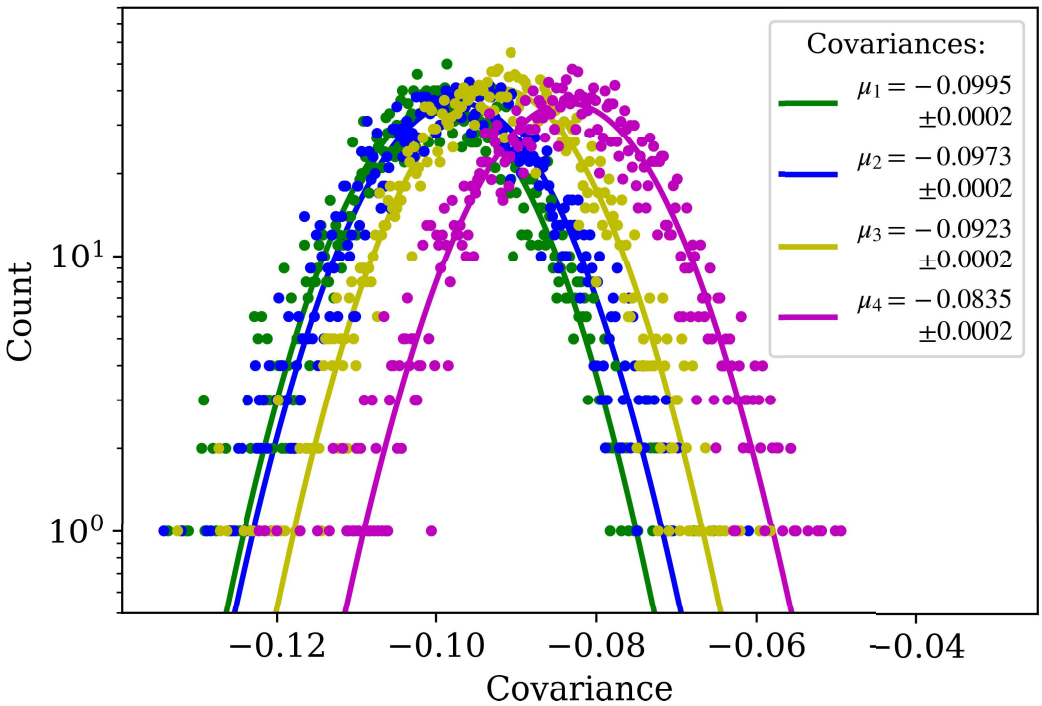

Figure 5.15. Covariance distributions among SRS separately for bin spacing = 1, 2, 3, 4 denoted by colors. Color code: Green for $\Delta j = 1$, blue for $\Delta j = 2$, yellow for $\Delta j = 3$, Magenta for $\Delta j = 4$.

Figure 5.15 shows the histograms and underlying Gaussian fits of $COV(\Delta j)$ for $\Delta j = 1, 2, 3, 4$. The general effect of spectrum flattening through SG filter is induction of negative correlations among the adjacent bins of SCS and SRS. Negative correlations decrease with increasing bin spacing as indicated by Figure 5.15. We expect a cut-off RF spacing Δf_c such that we no longer observe correlations for $\Delta\nu_c W > \Delta f_c$. This is because SG filter is based on polynomial fits within windows of IF width equal to W.

We have applied the result of this simulation to the actual data in order to correct the change of the rebinned and grand spectrum standard deviations due to SG filter induced bin height correlations. Without the correction, the standard deviation of the rebinned and the grand spectra are $\sigma^R = 0.95$ and $\sigma^G = 0.74$. With the correction rebinned spectrum sigma becomes $\sigma^R = 0.99$. When we calculate the grand spectrum (without the correction) using the corrected rebinned spectrum, we get $\sigma^G = 0.78$. And when we calculate the corrected grand spectrum using the rebinned spectrum that is not corrected, we get $\sigma^G = 0.91$. For our analysis, we use the corrected grand spectrum which is calculated using the corrected rebinned spectrum. In this case we get $\sigma^G = 0.96$.

5.12. Threshold for Candidate Selection

An axion signal should show up as spectrum bin(s) with positive excess power. Following the analysis procedure, we first set a target SNR for the axion search. Specifically, we choose $\mathrm{SNR}_T = 5$. That is, we set a minimum condition for an axion of KSVZ coupling in our grand spectrum to fulfill for our hypothesis testing procedure. As a function of the target SNR and the desired confidence level (CL) we set a threshold for candidate bin selection and we label each bin of height exceeding the threshold as axion candidates.

Figure 5.16 shows distribution of hypothetical bins that accommodate axion signal of the target SNR for our hypothesis test as compared to the distribution of the bins of noise only. Horizontal axis is the bin amplitude in the grand spectrum. Dashed

blue line shows the target SNR (SNR_T) whereas the red dashed line gives the threshold of candidate selection. Spectrum bins with noise only are samples of the green normal distribution with mean=0. The spectrum bins that possess the axion signal power are samples drawn from the blue Gaussian distribution with the same standard deviation ($\sigma^G = 1$) but mean = SNR_T. Brown and green regions give the percentages of false negative and false positive, respectively. Confidence level of axion detection is given by the area under the Gaussian PDF of the bin with axion signal (blue) on the right side of the threshold. That is, the sum of blue and green colored areas yields the confidence level.

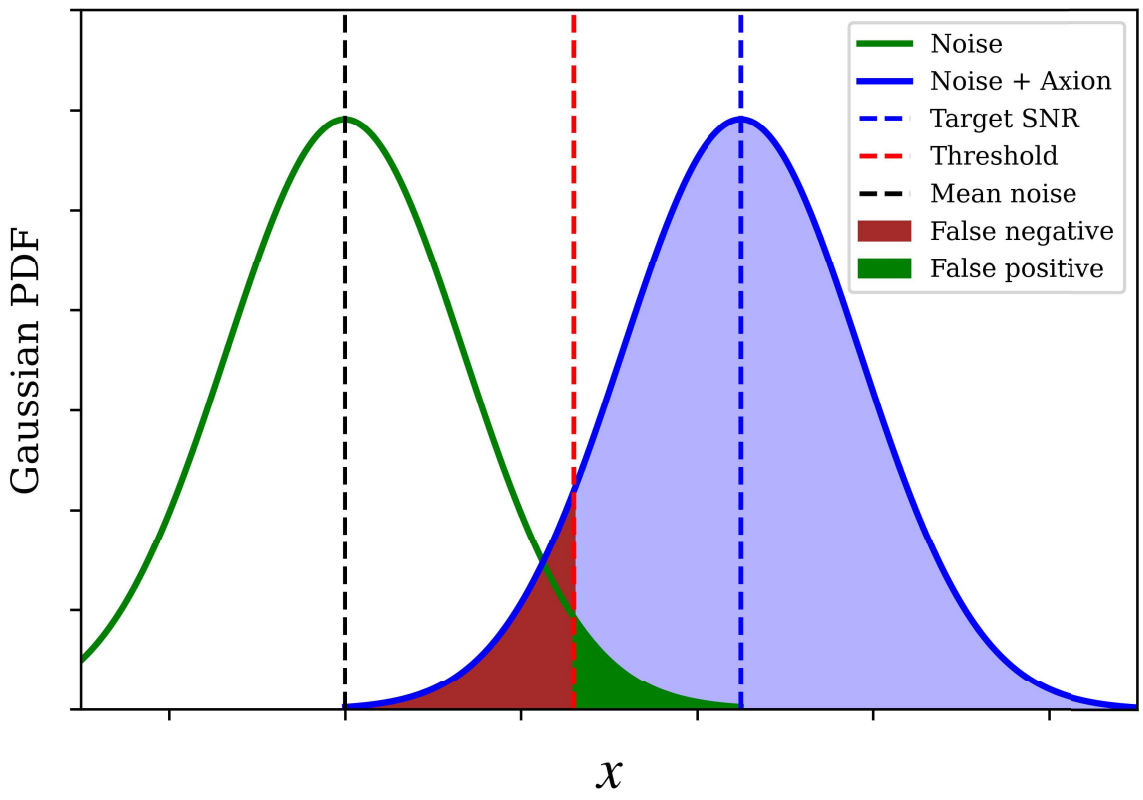

Figure 5.16. Hypothesis testing in search of the axion signal in grand spectrum.

Equation 5.42 gives the threshold Θ as a function of the SNR_T and the cumulative distribution function (CDF) of the bins that possess axion power (Blue curve in Figure 5.16) assuming non-zero SNR_T.

$$\Theta = 2\mathrm{SNR}_T - \mathrm{CDF}_S^{-1}(\mathrm{CL}) \tag{5.42}$$

where CDF_S is the CDF of the signal distribution. With $\mathrm{SNR}_T = 5$ and CL=90%, we obtain threshold $\Theta = 3.72$. Green area in Figure 5.16 represent the candidate bins in the spectrum that we aim to scrutinize by rescanning. The actual number of rescan candidate bins n_C in our grand spectrum is

$$n_C = N^G(1 - \mathrm{CDF}_N(\Theta)) \tag{5.43}$$

where CDF_N is the CDF of the noise distribution. And the expected number of grand spectrum bins that exceed threshold is $n_C \approx 45$. The actual number is $n_C = 41$.

5.13. Exclusion

Rescan analysis of our candidate signals is still ongoing. As a preliminary result we create an exclusion plot where we do not take into account the narrow frequency windows around the outlier signals that we still investigate. In Section 5.12, we explained that we expect an axion with KSVZ coupling g_γ^{KSVZ} to have signal-to-noise ratio $\mathrm{SNR}_T \propto \left(g_\gamma^{KSVZ}\right)^2$. In reality, each grand spectrum bin has SNR_g=$(\sigma_g^G)^{-1}$ where the subscript g is the RF index for the grand spectrum. Given this set of SNRs, for each grand spectrum bin we can exclude axion couplings higher than a minimum g_γ^{min}.

$$|g_\gamma^{min}|_g = \sqrt{\frac{\mathrm{SNR}_T}{(\sigma_g^G)^{-1}}}\ |g_\gamma^{KSVZ}| \tag{5.44}$$

Figure 5.17 shows the preliminary exclusion results for CAST-CAPP. The vertical axis gives $|g_\gamma^{min}|_g/|g_\gamma^{KSVZ}|$ therefore KSVZ axion-photon coupling is indicated by the dashed black line at y=1. Narrow frequency windows around the outliers that are discarded from this plot are not visible to eye. The yellow band indicates the parameter space for theoretically expected axion-photon couplings.

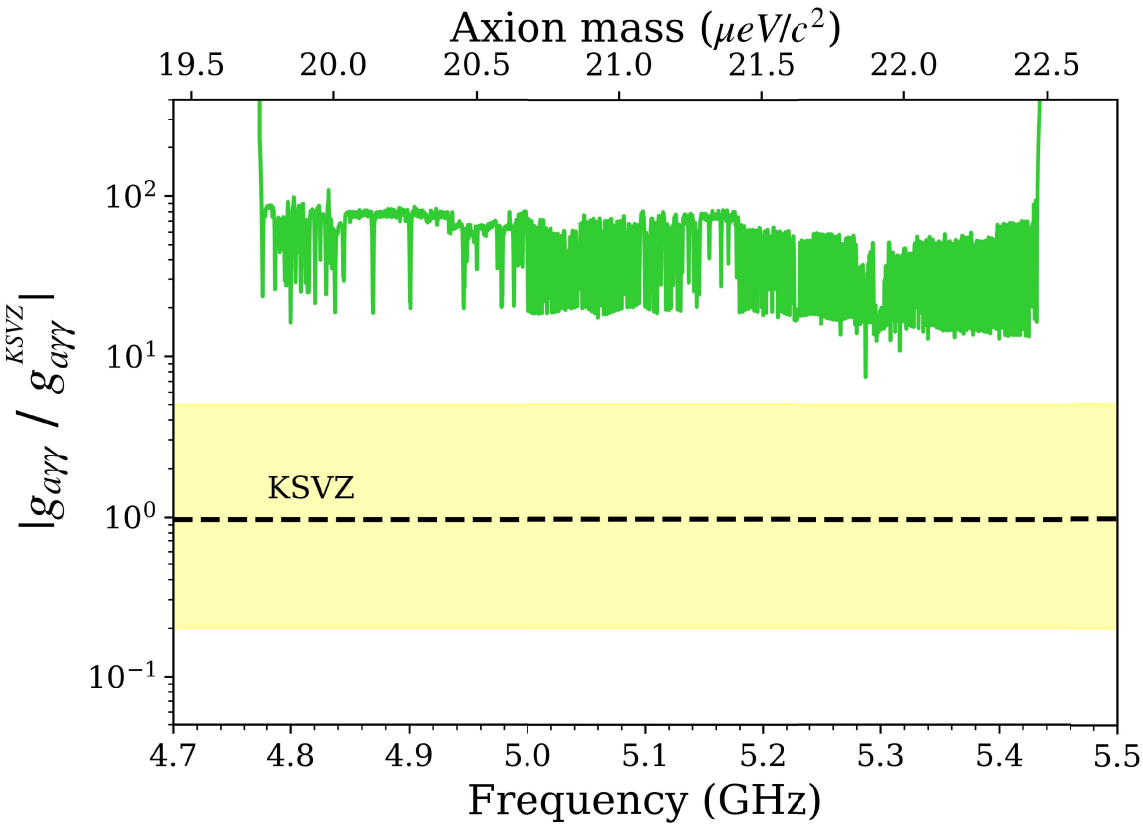

Figure 5.17. Axion-photon coupling exclusion plot for CAST-CAPP data.

Minimum coupling $|g_\gamma^{min}|_g$ in our spectrum ranges from $\sim 10^2$ to 20 $|g_\gamma^{KSVZ}|$. Narrow spikes on the plot are due to fixed frequency measurements. Time required to attain a $|g_\gamma^{min}|$ scales with the fourth root of time.

$$|g_\gamma^{min}|_g \propto \frac{1}{\sqrt{(\sigma_g^G)^{-1}}} = \frac{1}{\sqrt{\mathrm{SNR}_g}} \propto \frac{1}{t^{1/4}} \tag{5.45}$$

5.14. Axion Candidates

CAST-CAPP is the first axion haloscope that intentionally searches for axion streams in addition to galactic halo axions. For these two searches we have different procedures of handling analysis results, scrutinizing outlier signals and excluding axion mass-coupling constant parameter space. Both galactic halo and streaming axion searches assume that the axion mass is unknown. The big difference between the two methods is that the search for the virialized axions estimates the axions have a velocity distribution determined by Maxwell-Boltzmann (see Section 2.4), whereas the velocity distribution for streaming axions is another unknown. Moreover, streaming axion signals are expected to be transient in daily scale. This distinction between the two searches is the reason we separate the candidate examination and exclusion procedures. We apply the following procedure that is still in progress to identify such outlier that exceed the threshold set as explained in Section 5.12.

For galactic halo axions we consider the grand spectrum which is optimized for axion signals of width 5-7 kHz. We observe two types of outliers in the grand spectrum. First kind of candidates have reasonable amplitudes and are likely to be explained by the statistical fluctuations of noise. For such candidates only possible scrutiny is to rescan the narrow frequency intervals around them in order to increase the statistics. If any candidate survives the rescan analysis, we do the following investigations:

- Rescan the corresponding frequency with the same and with different cavity(ies).
- Study the widths and shapes of the possible candidates and compare them to those of the expected axion signal (5-7kHz width).
- If a signal candidate persists then we study its magnetic field dependence comparing B=ON with B=OFF.

The second kind of candidates are rare but have big amplitudes that are unlikely to stem from statistical fluctuations. We assume that this kind is likely originate from electromagnetic interference (EMI). In the beginning of our analysis procedure, we

search for and discard IF EMI (see Section 5.7) but RF EMI are likely to survive that quality check and contribute to our analysis. Still, we do not discard such unexpectedly large outliers and investigate for the small probability of transient axion signals. The following steps are undertaken to scrutinize such outliers:

- Study the time dependence of the outliers.
- Examine the frequency range in which the outlier is in the combined spectrum. Combined spectrum has a resolution bandwidth of 50 Hz, thus may reveal the shape of the signal. Most of the time a peak of width several hundred Hz might originate from a very sharp peak ∼50 Hz in the combined spectrum.
- Compare the cavity data with the data taken by the external antenna. An EMI parasite is likely to show up in both channels. We cross-check whether the peak frequency of an outlier coincides with the environmental background measured in July 2020. In such a case the specific outlier is discarded as EMI/EMC parasite.

Specifically, for streaming axions or mini-clusters we consider the daily combined spectra that has a much higher resolution with a 50 Hz bin width. For this case we do not consider the threshold for the grand spectrum. Instead, we apply a rough 5σ threshold to the daily combined spectra. We have gathered up to now more than 500 TB of raw data in the complex time domain, which eventually will allow us to run a frequency analysis with bandwidths as low as 1 milli-Hz or less. This has the potential to statistically reveal single (axion-related) microwave photons per second with the current CAST setup. In this case we are sensitive to an axion signal width which can be much smaller than that for conventional halo axions; in addition, depending on the gravitational alignment, signals may show up for a short period of time. For their identification we follow the steps below additionally:

- Analyze daily our data taken and plot the daily combined spectra in all cavity(ies) configurations in order to check for occasional power excesses.
- Study outlier daily signals over time in case of multiple Earth crossings by streams.

6. CONCLUSION

After 20 years of successful operation as an axion helioscope, searching for solar axions, CAST is now evolving into an haloscope that hunt for galactic halo axion that is also good candidates for the dark matter. CAST-CAPP is one of the 2 haloscope experiment in CAST and has been operating in the last 2 years. With the ongoing hardware improvements CAST-CAPP is a promising experiment in competitive search for the axion. With 4 tunable cavities that can be operated single or in phase-matched state CAST-CAPP is scanning 19-22 μeV axion mass range corresponding to 4.7-5.4 GHz RF band. With the axion candidate scrutiny still in progress, preliminary results of data analysis indicate that CAST-CAPP is currently able to exclude axion-photon couplings down to $\sim 20 \times g_{a\gamma\gamma}^{\mathrm{KSVZ}}$ in its operation range.

REFERENCES

1. CAST Collaboration, "New CAST limit on the axion–photon interaction", *Nature Physics*, Vol. 13, pp. 584–590, 2017.

2. Barth, K. et al., "Commissioning and First Operation of the Cryogenics for the CERN Axion Solar Telescope (CAST)", *AIP Conference Proceedings*, Vol. 710, No. 1, pp. 168–175, 2004, `https://aip.scitation.org/doi/abs/10.1063/1.1774679`.

3. Stern, I., A. A. Chisholm, J. Hoskins, P. Sikivie, N. S. Sullivan, D. B. Tanner, G. Carosi and K. van Bibber, "Cavity design for high-frequency axion dark matter detectors", *Review of Scientific Instruments*, Vol. 86, No. 12, 2015, `https://doi.org/10.1063/1.4938164`.

4. Miceli, L., "Haloscope axion searches with the cast dipole magnet: the CAST-CAPP/IBS detector", *11th Patras Workshop on Axions, WIMPs and WISPs*, pp. 164–168, 2015.

5. Rubin, V. C. and W. K. Ford, Jr, "Rotation Of The Andromeda Nebula From A Spectroscopic Survey Of Emission Regions.", *Astrophys. J.*, Vol. 159, pp. 379–403, 1 1970, `https://www.osti.gov/biblio/4148861`.

6. Massey, R., T. Kitching and J. Richard, "The dark matter of gravitational lensing", *Reports on Progress in Physics*, Vol. 73, No. 8, jul 2010, `https://doi.org/10.1088/0034-4885/73/8/086901`.

7. Begeman, K. G., A. H. Broeils and R. H. Sanders, "Extended rotation curves of spiral galaxies: dark haloes and modified dynamics", *Monthly Notices of the Royal Astronomical Society*, Vol. 249, No. 3, pp. 523–537, April 1991, `https://doi.org/10.1093/mnras/249.3.523`.

8. XENON Collaboration, "Excess electronic recoil events in XENON1T", *Phys. Rev. D*, Vol. 102, Oct 2020, https://link.aps.org/doi/10.1103/PhysRevD.102.072004.

9. Asztalos, S. et al., "Large-scale microwave cavity search for dark-matter axions", *Phys. Rev. D*, Vol. 64, Oct 2001, https://link.aps.org/doi/10.1103/PhysRevD.64.092003.

10. Semertzidis, Y. K. et al., "Axion Dark Matter Research with IBS/CAPP", *ArXiv e-prints*, 2019, arXiv: 1910.11591.

11. Primakoff, H., "Photo-Production of Neutral Mesons in Nuclear Electric Fields and the Mean Life of the Neutral Meson", *Phys. Rev.*, Vol. 81, pp. 899–899, Mar 1951.

12. Redondo, J. and A. Ringwald, "Light shining through walls", *Contemporary Physics*, Vol. 52, No. 3, p. 211–236, May 2011, http://dx.doi.org/10.1080/00107514.2011.563516.

13. Melcón, A. Á., S. A. Cuendis, C. Cogollos, A. Díaz-Morcillo, B. Döbrich, J. D. Gallego, B. Gimeno, I. G. Irastorza, A. J. Lozano-Guerrero, C. Malbrunot, P. Navarro, C. P. Garay, J. Redondo, T. Vafeiadis and W. Wuensch, "Axion searches with microwave filters: the RADES project", *Journal of Cosmology and Astroparticle Physics*, Vol. 2018, No. 05, pp. 040–040, may 2018, https://doi.org/10.1088/1475-7516/2018/05/040.

14. Zioutas, K. et al., "A decommissioned LHC model magnet as an axion telescope", *Nuclear Instruments and Methods in Physics Research Section A: Accelerators, Spectrometers, Detectors and Associated Equipment*, Vol. 425, No. 3, pp. 480 – 487, 1999, http://www.sciencedirect.com/science/article/pii/S0168900298014429.

15. CAST Collaboration, "The CERN axion solar telescope (CAST): status and prospects", *Nuclear Physics B - Proceedings Supplements*, Vol. 114, pp. 75 – 80, 2003, http://www.sciencedirect.com/science/article/pii/S0920563202018947.

16. Abbon, P. et al., "The Micromegas detector of the CAST experiment", *New Journal of Physics*, Vol. 9, No. 6, pp. 170–170, jun 2007.

17. Krieger, C., J. Kaminski and K. Desch, "InGrid-based X-ray detector for low background searches", *Nuclear Instruments and Methods in Physics Research Section A: Accelerators, Spectrometers, Detectors and Associated Equipment*, Vol. 729, pp. 905 – 909, 2013, http://www.sciencedirect.com/science/article/pii/S0168900213012163.

18. Yildiz, S. C., "X-ray detectors of the CAST experiment", *Journal of Instrumentation*, Vol. 9, No. 03, pp. C03047–C03047, mar 2014.

19. Abbon, P. et al., "The Micromegas detector of the CAST experiment", *New Journal of Physics*, Vol. 9, No. 6, pp. 170–170, jun 2007.

20. CAST Collaboration, "Search for Solar Axions by the CERN Axion Solar Telescope with ^{3}He Buffer Gas: Closing the Hot Dark Matter Gap", *Phys. Rev. Lett.*, Vol. 112, Mar 2014, https://link.aps.org/doi/10.1103/PhysRevLett.112.091302.

21. CAST Collaboration, "First results on the search for chameleons with the KWISP detector at CAST", *Physics of the Dark Universe*, Vol. 26, p. 100367, 2019, http://www.sciencedirect.com/science/article/pii/S2212686419301517.

22. Wu, C. S., E. Ambler, R. W. Hayward, D. D. Hoppes and R. P. Hudson, "Experimental Test of Parity Conservation in Beta Decay", *Phys. Rev.*, Vol. 105, pp. 1413–1415, Feb 1957, https://link.aps.org/doi/10.1103/PhysRev.105.1413.

23. Christenson, J. H., J. W. Cronin, V. L. Fitch and R. Turlay, "Evidence for the

2π Decay of the K_2^0 Meson", *Phys. Rev. Lett.*, Vol. 13, pp. 138–140, Jul 1964, https://link.aps.org/doi/10.1103/PhysRevLett.13.138.

24. Abel, C. et al., "Measurement of the Permanent Electric Dipole Moment of the Neutron", *Phys. Rev. Lett.*, Vol. 124, p. 081803, Feb 2020, https://link.aps.org/doi/10.1103/PhysRevLett.124.081803.

25. Yıldız, S. C., *Search For Axions With MICROMEGAS Detectors in the CERN CAST Experiment*, Ph.D. Thesis, Boğaziçi University, 2013.

26. Peccei, R. D. and H. R. Quinn, "CP Conservation in the Presence of Pseudoparticles", *Phys. Rev. Lett.*, Vol. 38, pp. 1440–1443, Jun 1977, https://link.aps.org/doi/10.1103/PhysRevLett.38.1440.

27. Peccei, R. D. and H. R. Quinn, "Constraints imposed by CP conservation in the presence of pseudoparticles", *Phys. Rev. D*, Vol. 16, pp. 1791–1797, Sep 1977, https://link.aps.org/doi/10.1103/PhysRevD.16.1791.

28. Sikivie, P., "Experimental Tests Of The "Invisible" Axion", *Phys. Rev. Lett.*, Vol. 52, pp. 695–695, Feb 1984, https://link.aps.org/doi/10.1103/PhysRevLett.52.695.2.

29. Turner, M. S., "Periodic signatures for the detection of cosmic axions", *Phys. Rev. D*, Vol. 42, pp. 3572–3575, Nov 1990, https://link.aps.org/doi/10.1103/PhysRevD.42.3572.

30. Brubaker, B. M., L. Zhong, S. K. Lamoreaux, K. W. Lehnert and K. A. van Bibber, "HAYSTAC axion search analysis procedure", *Phys. Rev. D*, Vol. 96, Dec 2017, https://link.aps.org/doi/10.1103/PhysRevD.96.123008.

31. Read, J. I., "The local dark matter density", *Journal of Physics G: Nuclear and Particle Physics*, Vol. 41, No. 6, may 2014, https://doi.org/10.1088/0954-3899/41/6/063101.

32. ADMX Collaboration, "Piezoelectrically Tuned Multimode Cavity Search for Axion Dark Matter", *Phys. Rev. Lett.*, Vol. 121, Dec 2018, `https://link.aps.org/doi/10.1103/PhysRevLett.121.261302`.

33. Zioutas, K. et al., "Search for axions in streaming dark matter", *ArXiv e-prints*, 2017, arXiv: 1703.01436.

34. Eggemeier, B., J. Redondo, K. Dolag, J. C. Niemeyer and A. Vaquero, "First Simulations of Axion Minicluster Halos", *Phys. Rev. Lett.*, Vol. 125, Jul 2020, `https://link.aps.org/doi/10.1103/PhysRevLett.125.041301`.

35. Sofue, Y., "Gravitational Focusing of Low-Velocity Dark Matter on the Earth's Surface", *ArXiv e-prints*, 2020, arXiv: 2005.08252.

36. Jackson, J. D., *Classical electrodynamics; 1st ed.*, Wiley, New York, 1962.

37. Brubaker, B. M., "First results from the HAYSTAC axion search", *ArXiv e-prints*, 2018, arXiv: 1801.00835.

38. Turyshev, S. G., "Wave-theoretical description of the solar gravitational lens", *Phys. Rev. D*, Vol. 95, Apr 2017, `https://link.aps.org/doi/10.1103/PhysRevD.95.084041`.

39. Ahn, D., O. Kwon, W. Chung, W. Jang, D. Lee, J. Lee, S. W. Youn, D. Youm and Y. K. Semertzidis, "Maintaining high Q-factor of superconducting $YBa_2Cu_3O_{7-x}$ microwave cavity in a high magnetic field", *ArXiv e-prints*, 2019, arXiv: 1904.05111.

40. Arfken, G. B., H. J. Weber and F. E. Harris, *Mathematical Methods for Physicists, 7th ed.*, Academic Press, Boston, 2013.

41. Press, W. H., S. A. Teukolsky, W. T. Vetterling and B. P. Flannery, *Numerical Recipes in C (2nd Ed.): The Art of Scientific Computing*, Cambridge University

Press, USA, 1992.

42. Hunter, T. R. and R. Kimberk, "Statistical Topics Concerning Radiometer Theory", *ArXiv e-prints*, 2015, arXiv: 1507.04280.

43. Weisstein, E. W., "Chi-Squared Distribution.", `https://mathworld.wolfram.com/Chi-SquaredDistribution.html`, last visited on 8/1/2021.

44. Dicke, R. H., "The Measurement of Thermal Radiation at Microwave Frequencies", *Review of Scientific Instruments*, Vol. 17, No. 7, pp. 268–275, 1946, `https://doi.org/10.1063/1.1770483`.

45. ADMX Collaboration, "Axion Dark Matter eXperiment: Run 1B Analysis Details", *ArXiv e-prints*, 2020, arXiv: 2010.06183.

46. Ahn, S., S. Lee, J. Choi, B. R. Ko and Y. K. Semertzidis, "Improved axion haloscope search analysis", *ArXiv e-prints*, 2020, arXiv: 2004.08011.

47. Jeong, J., S. Youn, S. Ahn, C. Kang and Y. K. Semertzidis, "Phase-matching of multiple-cavity detectors for dark matter axion search", *Astroparticle Physics*, Vol. 97, pp. 33 – 37, 2018, `http://www.sciencedirect.com/science/article/pii/S0927650517302190`.

48. Schafer, R. W., "What Is a Savitzky-Golay Filter? [Lecture Notes]", *IEEE Signal Processing Magazine*, Vol. 28, No. 4, pp. 111–117, 2011.

49. Landau, L. and E. Lifshitz, *Statistical Physics: Volume 5*, 5. c., Elsevier Science, 2013, `https://books.google.com.tr/books?id=VzgJN-XPTRsC`.

50. Cooley, J. W. and J. W. Tukey, "An Algorithm for the Machine Calculation of Complex Fourier Series", *Mathematics of Computation*, Vol. 19, No. 90, pp. 297–301, 1965, `http://www.jstor.org/stable/2003354`.

APPENDIX A: AXION LINE SHAPE

Galactic halo axion signal shape depends on its energy distribution over frequency space. Assuming that particle energies for virialized halo axions is dominated by their mass, we will apply classical ideal gas formalism to find the frequency distribution of virialized halo axion. Normalized probability distribution function (Equation A.2) for particle momenta is given by Maxwell-Boltzmann distribution. [49]

$$Z = \int\int\int_{-\infty}^{\infty} exp\left(-\frac{p_x^2+p_y^2+p_z^2}{2mk_BT}\right) dp_x dp_y dp_z = (2\pi k_BT)^{3/2} \tag{A.1}$$

$$f(p_x,p_y,p_z)d^3\overrightarrow{p} = \frac{1}{Z}exp\left(-\frac{p_x^2+p_y^2+p_z^2}{2mk_BT}\right) d^3\overrightarrow{p} \tag{A.2}$$

$$= (2\pi mk_BT)^{-3/2}exp\left(-\frac{p^2}{2mk_BT}\right) p^2 dpsin\theta' d\theta' d\phi' \tag{A.3}$$

$$f(p)dp = 4\pi(2\pi mk_BT)^{-3/2}exp\left(-\frac{p^2}{2mk_BT}\right) p^2 dp \tag{A.4}$$

$$f(E)dE = 4\pi(2\pi mk_BT)^{-3/2}m\sqrt{2mE}e^{-E/k_BT}dE \tag{A.5}$$

$$= 2(k_BT)^{-3/2}e^{-E/k_BT}\sqrt{E/\pi}dE$$

Equation A.1 gives the partition function Z as an integral over momenta p_x, p_y, p_z in 3-dimensional space. We benefit from the spherical symmetry of momentum space to write the infinitesimal volume $d^3\overrightarrow{p}$ in terms of dp, polar and azimuthal angles in momentum space (Figure A.3). We integrate over these angles to find the distribution for the absolute value of momentum (Figure A.4). We use the classical dispersion relation $dE = (p/m)dp$ to obtain the distribution function for energy (Figure A.5). Using the probability distribution function we calculate the expected values for energy (Equation A.6) and velocity squared (Equation A.7).

$$\langle E \rangle = \int E f(E) dE = \frac{3}{2} k_B T \tag{A.6}$$

$$\langle v^2 \rangle = 3 k_B T / m_a \tag{A.7}$$

For the discussion above, we used arguments of classical statistical mechanics only. Therefore, we considered E as the kinetic energy. We should also take the rest mass m_a of the axion into account. Total energy of the axion is given by Figure A.8 where we also used Planck's equation to relate particle energy to frequency.

$$E_{Total} = \langle E \rangle + m_a c^2 = h\nu \tag{A.8}$$

$$h\nu_a = m_a c^2 \tag{A.9}$$

$$\langle E \rangle = h(\nu - \nu_a) \tag{A.10}$$

The minimum value of axion energy is limited by its mass, m_a, which also imposes a minimum limit for the axion frequency, ν_a, given by Equation A.9. In order to obtain the distribution function for axion signal over frequency space, we manipulate Equation A.5 using Equations A.7, A.9, A.10 and the relation $dE = hd\nu$. Equation A.11 shows the distribution function for frequency where $\langle \beta^2 \rangle = \langle v^2 \rangle / c^2$. Root mean square (RMS) velocity of the galactic halo in the rest frame of Milky Way is $v_{RMS} = \sqrt{\langle v^2 \rangle} \approx 270 km/s$. [29]

$$f(\nu) d\nu = \frac{2}{\sqrt{\pi}} \left(\frac{3}{\nu_a \langle \beta^2 \rangle} \right)^{3/2} \sqrt{\nu - \nu_a} \;\; exp \left(- \frac{3(\nu - \nu_a)}{\nu_a \langle \beta^2 \rangle} \right) d\nu \tag{A.11}$$

Calculations above are valid for an inertial observer (or a detector) in galactic frame. However our lab (earth) is also moving around the galaxy with velocity $\vec{v}_{Lab} = \vec{v}_{Sun} + \vec{v}_{orbital} + \vec{v}_{rotational}$ where the speed of the sun with respect to galactic frame $v_{Sun} \approx 230 km/s$, Earth's orbital speed around the sun $v_{orbital} \approx 30 km/s$ and the rotational speed of the lab around the earth $v_{rotational} < 0.5 km/s$. Since the directions

of these vectors are not constant $\vec{v}_{Lab}$ varies in time. In lab frame, axion velocity is $\vec{v}_A = \vec{v} - \vec{v}_{Lab}$. For our experiments on earth, we should consider the distribution function in laboratory frame. In the lab frame, the distribution function for energy becomes Equation A.12. [29] Here, $r = v_{Lab}/v_{RMS} \approx 0.85$ is the ratio of the velocity of lab (earth) with respect to the galactic rest frame to RMS velocity of galactic halo. Distribution function for frequency is given by Equation A.13. [30] RMS velocity of DM axion halo in lab frame becomes $v_{a,RMS} = \sqrt{\langle v_a^2 \rangle} \approx 350 km/s$.

$$f_{Lab}(E)dE = \frac{2\sqrt{\beta/\pi}}{m_a v_{Lab}} \; exp\left(-\beta v_{Lab}^2 - 2\beta E/m_a\right) sinh(2\beta v_{Lab}(2E/m_a)^2)dE \tag{A.12}$$

$$f_{Lab}(\nu)d\nu = \frac{\sqrt{6/\pi}}{r\nu_a\langle\beta^2\rangle} \; exp\left(-\frac{3r^2}{2} - \frac{3(\nu-\nu_a)}{\nu_a\langle\beta^2\rangle}\right) sinh\left(3r\sqrt{\frac{2(\nu-\nu_a)}{\nu_a\langle\beta^2\rangle}}\right) d\nu \tag{A.13}$$

APPENDIX B: FAST FOURIER TRANSFORM

Algorithms that calculate DFT considerably faster than $O(N^2)$ are called Fast Fourier Transform (FFT). Such algorithms are being developed since Carl Friedrich Gauss (1805). The most common of such algorithms is Cooley–Tukey algorithm which is computed in $O(Nlog_2N)$ operations by recursively dividing the dataset of length N in to sets of length $N/2, N/4, ...$ and applying DFT. [50] What makes this technique feasible is that we can write a DFT of length N as a sum of DFTs of length $N/2$ as shown in Equation B.2 where we write A_k array as a summation of 2 arrays made up of even and odd indexed components of A_k. Although $A_{k,even}$ and $A_{k,even}$ are of length $N/2$ we can still use index k because both are periodic in k, that is $A_{1,even} = A_{N/2+1,even}$ for example. This property of DFT is called *Danielson-Lanczos Lemma* which we can recursively apply until we get summations (as Equation B.1) of length 1, that is $k = 0$. So, we obtain N Danielson-Lanczos (DL) numbers such as $A_{k,even/odd...even/even}$ that are DFTs of f_n. For a vector of length 1 (a number), DFT matrix is just the identity operator. Therefore $A_{k,even/odd...even/even} = f_n$ for some n. We should figure out for what combination of even/odd which n we get. Let us call each single DL number by an index $j = 0, 1, ..., N-1$. We want to match every single A^j to an f_n. The correspondence between these two is given by bit reversal permutation of f_n vector of length N. That is, we give all f_n a binary code of log_2N bits in order $0...001, 0...010, ..., 1...10, 1...11$ (assuming the ideal case of FFT where N is a power of 2) and we arrange f_n in for bit-reversed order. Thus, bit-reversed f_n becomes f^j and $f^j = A^j$ for all j indices. [41]

$$\begin{aligned} A_k &= \sum_{n=0}^{N-1} w^{-kn} f_n \\ &= \sum_{n=0}^{N/2-1} w^{-2kn} f_{2n} + \sum_{n=0}^{N/2-1} w^{-k(2n+1)} f_{2n+1} \\ &= \sum_{n=0}^{N/2-1} w^{-2kn} f_{2n} + w^{-k} \sum_{n=0}^{N/2-1} w^{-2kn} f_{2n+1} \end{aligned} \tag{B.1}$$

$$A_k = A_{k,even} + w^{-k} A_{k,odd} \tag{B.2}$$

In summary, FFT begins by equating the bit-reverse ordered input data array to A^j array. Then, benefiting from *Danielson-Lanczos Lemma* we perform combined DFT on A^j in groups of size $2, 4, ..., N/2, N$ increasing at each step, the final steps being Equation B.2. The number of couple combinations at each step go like $N/2, N/4, ..., 2, 1$. Total number of combinations is $N(1/2 + 1/4 + ...) = N$. And in total there are $log_2 N$ steps. Therefore, FFT requires $O(N log_2 N)$ operations.

APPENDIX C: COPYRIGHT PERMISSIONS

As of December 2020, Boğaziçi University Institute of Graduate Studies in Science and Engineering requires the declaration of copyright permissions for the thesis figures that have been used before in other documents. Below is a list of such figure I used in this thesis and the corresponding declarations of copyright permissions.

- Copyright permissions for Figure 1.1 and Figure 1.4 from the article [1] is expressed on the article's website[2] as follows

  This article is licensed under a Creative Commons Attribution 4.0 International License, which permits use, sharing, adaptation, distribution and reproduction in any medium or format, as long as you give appropriate credit to the original author(s) and the source, provide a link to the Creative Commons license, and indicate if changes were made. The images or other third party material in this article are included in the article's Creative Commons license, unless indicated otherwise in a credit line to the material.

  I hereby declare that Figure 1.1 and Figure 1.4 from the article [1] are licensed under the Creative Commons Attribution 4.0 International License.[3] I use these figures without making a change.
- Figure 1.3 is available online at CERN Document Server (CDS) with report number CERN-AT-2004-001-ECR.[4] Figure 4.4 is available online at CERN Document Server (CDS) with report number DESY-PROC-2015-02.[5] Copyright permission of the materials in CDS are indicated in CDS website:[6]

  The CERN Document Server contains multimedia material under CERN copyright. You can freely download and use the high-resolution version of these files,

[2] https://www.nature.com/articles/nphys4109
[3] http://creativecommons.org/licenses/by/4.0/
[4] https://cds.cern.ch/record/708949
[5] https://cds.cern.ch/record/2110146
[6] http://cds.cern.ch/help/high-res-multimedia

provided you agree and respect the conditions of use.

I used the aforementioned figure in line the terms of use for CERN audiovisual media.[7]

- Copyright permission of Figure 2.1 from article [3] is obtained from AIP Publishing. Below is the license document for the use of Figure [3] in this thesis.

[7] https://copyright.web.cern.ch/

AIP PUBLISHING LICENSE
TERMS AND CONDITIONS

Feb 20, 2021

This Agreement between CERN / Bogazici University -- Kaan Ozbozduman ("You") and AIP Publishing ("AIP Publishing") consists of your license details and the terms and conditions provided by AIP Publishing and Copyright Clearance Center.

License Number	5013291155348
License date	Feb 20, 2021
Licensed Content Publisher	AIP Publishing
Licensed Content Publication	Review of Scientific Instruments
Licensed Content Title	Cavity design for high-frequency axion dark matter detectors
Licensed Content Author	I. Stern, A. A. Chisholm, J. Hoskins, et al
Licensed Content Date	Dec 1, 2015
Licensed Content Volume	86
Licensed Content Issue	12
Type of Use	Thesis/Dissertation
Requestor type	Student

Format	Print and electronic
Portion	Figure/Table
Number of figures/tables	1
Title	IN SEARCH OF THE AXION PARTICLE WITH RF CAVITIES IN CAST EXPERIMENT AT CERN
Institution name	Bogazici University
Expected presentation date	Apr 2021
Portions	Figure 1
Requestor Location	CERN / Bogazici University Bogazici University, Physics Department North Campus, KB Building Floor 3-4 Bebek Istanbul, 34342 Turkey Attn: CERN / Bogazici University
Total	0.00 USD

Terms and Conditions

AIP Publishing -- Terms and Conditions: Permissions Uses

AIP Publishing hereby grants to you the non-exclusive right and license to use and/or distribute the Material according to the use specified in your order, on a one-time basis, for the specified term, with a maximum distribution equal to the number that you have ordered. Any links or other content accompanying the Material are not the subject of this license.

1. You agree to include the following copyright and permission notice with the reproduction of the Material:"Reprinted from [FULL CITATION], with the permission of AIP Publishing." For an article, the credit line and permission notice must be printed on the first page of the article or book chapter. For photographs, covers, or tables, the notice may appear with the Material, in a footnote, or in the reference list.
2. If you have licensed reuse of a figure, photograph, cover, or table, it is your responsibility to ensure that the material is original to AIP Publishing and does not

contain the copyright of another entity, and that the copyright notice of the figure, photograph, cover, or table does not indicate that it was reprinted by AIP Publishing, with permission, from another source. Under no circumstances does AIP Publishing purport or intend to grant permission to reuse material to which it does not hold appropriate rights.
You may not alter or modify the Material in any manner. You may translate the Material into another language only if you have licensed translation rights. You may not use the Material for promotional purposes.

3. The foregoing license shall not take effect unless and until AIP Publishing or its agent, Copyright Clearance Center, receives the Payment in accordance with Copyright Clearance Center Billing and Payment Terms and Conditions, which are incorporated herein by reference.
4. AIP Publishing or Copyright Clearance Center may, within two business days of granting this license, revoke the license for any reason whatsoever, with a full refund payable to you. Should you violate the terms of this license at any time, AIP Publishing, or Copyright Clearance Center may revoke the license with no refund to you. Notice of such revocation will be made using the contact information provided by you. Failure to receive such notice will not nullify the revocation.
5. AIP Publishing makes no representations or warranties with respect to the Material. You agree to indemnify and hold harmless AIP Publishing, and their officers, directors, employees or agents from and against any and all claims arising out of your use of the Material other than as specifically authorized herein.
6. The permission granted herein is personal to you and is not transferable or assignable without the prior written permission of AIP Publishing. This license may not be amended except in a writing signed by the party to be charged.
7. If purchase orders, acknowledgments or check endorsements are issued on any forms containing terms and conditions which are inconsistent with these provisions, such inconsistent terms and conditions shall be of no force and effect. This document, including the CCC Billing and Payment Terms and Conditions, shall be the entire agreement between the parties relating to the subject matter hereof.

This Agreement shall be governed by and construed in accordance with the laws of the State of New York. Both parties hereby submit to the jurisdiction of the courts of New York County for purposes of resolving any disputes that may arise hereunder.

V1.2

Questions? customercare@copyright.com or +1-855-239-3415 (toll free in the US) or +1-978-646-2777.